Computer Simulation of a Novel Technique for Radio-Frequency Ablation of Ventricular Arrhythmias

by

Tamara S. Rosbury

B.S. Physics
Tennessee State University, 1998

S.M. Electrical Engineering and Computer Science
Massachusetts Institute of Technology, 2000

SUBMITTED TO THE DEPARTMENT OF ELECTRICAL ENGINEERING AND COMPUTER SCIENCE IN PARTIAL FULFILLMENT OF THE REQUIREMENTS FOR THE DEGREE OF

DOCTOR OF PHILOSOPHY IN ELECTRICAL ENGINEERING AND COMPUTER SCIENCE
AT THE
MASSACHUSETTS INSTITUTE OF TECHNOLOGY

SEPTEMBER 2006

Signature of Author: _____
Department of Electrical Engineering and Computer Science
September 2006

Certified by: _____
Richard J. Cohen
Whitaker Professor in Biomedical Engineering
Harvard-MIT Division of Health Sciences and Technology
Thesis Supervisor

Accepted by: _____
Arthur C. Smith
Chairman, Department Committee on Graduate Students

Computer Simulation of a Novel Technique for Radio-Frequency Ablation of Ventricular Arrhythmias

by

Tamara S. Rosbury

Submitted to the Department of Electrical Engineering and Computer Science
on August 30, 2006 in Partial Fulfillment of the
Requirements for the Degree of Doctor of Philosophy in
Electrical Engineering and Computer Science

ABSTRACT

Ventricular Tachycardia (VT) is a rapid arrhythmia, most commonly due to reentrant electrical activity in the heart. A common treatment for VT is Radio-Frequency Ablation (RFA), which is minimally invasive, but requires maintenance of VT until the target site for ablation is determined. Most patients with VT cannot tolerate this maintenance phase due to hemodynamic instability and for those who are hemodynamically stable, the RFA procedure is successful in permanently terminating the VT in only approximately half of the cases. Therefore, the need for an RFA procedure that accurately localizes the site for ablation, or exit site of the reentry circuit, and is safe for unstable patients is evident.

We believe utilization of the Single Equivalent Moving Dipole model and inverse problem in cardiology will prove to be efficient in localizing the exit site of the reentry circuit and guiding the ablation catheter to that localized site during the RFA procedure. In principle, our RFA technique only requires a single beat of VT to localize the exit site of the reentry circuit. The objective of this thesis is to determine in a simulation model if one can guide a catheter to the exit site of the reentry circuit using body surface potentials in order to ablate that site with radio-frequency energy. In our new approach to RFA, we sought to design a finite element model to simulate VT due to reentry, develop an algorithm to localize the exit site of the reentry circuit through analysis of body surface potentials, localize the ablation catheter in both slow and fast VT, and advance the ablation catheter to the localized exit site of the reentry circuit. The proposed new RFA procedure promises to provide a new rapid and effective means for treatment of VT.

Thesis Supervisor: Richard J. Cohen
Title: Whitaker Professor in Biomedical Engineering

Acknowledgements

First and foremost, I offer thanks and praise to God for equipping me with the strength and endurance to complete my Ph.D. I thank my husband, Darren Rosbury, who has always been supportive, never doubting my ability to achieve my academic goal. Entering my life at exactly six weeks before my defense date was our healthy, beautiful son, Enzo, who gives me yet another reason to be thankful each and every day. I am grateful to my mother, Brenda Minor, whose independence and hard work ethic inspired me as a child to persevere no matter what obstacles I might encounter in life.

I thank Lucent Technologies for four years fellowship support. I thank my advisor, Dr. Richard Cohen for the many years of financial, technical, and personal support. When I initially joined the Cohen Lab, I invited Dr. Cohen to attend MIT's annual Martin Luther King, Jr. Breakfast, where I was a speaker. His presence let me know from the beginning that he was in my corner and the following years validated my impression. I appreciate Dr. Cohen's assistant, Amy Donovan, for the many years of managing the lab and meeting the needs of students. I also thank Maya Barley and Dr. Grace Xiao, colleagues who have provided technical insight throughout the years. I am thankful to members of the Academy of Courageous Minority Engineers (ACME) for their continual support and encouragement during my navigation through graduate school.

Last but not least, I will be forever thankful to Dr. Yuri Chernyak for taking on the roles as my supervisor and mentor. Yuri exposed me to a thorough approach to research that will remain with me for the rest of my life. During the many years of

working with Yuri, he was always willing to help and continually challenged me in various ways to become a competent research scientist. I truly miss Yuri and his untimely death reminds me to cherish the people you hold dear every time you get a chance because tomorrow is not promised to anyone. I did not know that the last time Yuri and I met would be our last. Yuri, I thank you more than you will ever know for your generous contribution in helping me to complete my Ph.D. I pray that your soul will rest in peace.

Table of Contents

1 Introduction 7
1.1 Thesis Motivation 7
1.2 Thesis Objectives 9
2 Background 13
2.1 Electrical Activity of the Heart 13
2.1.1 Cardiac Action Potential 13
2.1.2 Cellular Transmembrane Currents 15
2.1.3 Refractory Period of the Action Potential 18
2.2 Heart Anatomy 19
2.3 Electrical Conduction System of the Heart 20
2.4 Sudden Cardiac Death 23
2.5 Ventricular Tachyarrhythmias 24
2.5.1 Ventricular Tachycardia 26
2.5.2 Premature Ventricular Contractions 28
2.6 Reentry 29
2.7 Anti-arrhythmic Drugs 32
2.8 Implantable Cardioverter Defibrillators 33
2.9 Radio-Frequency Ablation 36
2.10 Mapping Techniques 39
2.10.1 Surface ECG 40
2.10.2 Activation Sequence Mapping 41
2.10.3 Pace Mapping 44
2.10.4 Entrainment Mapping 46
2.10.5 Entrainment with Concealed Fusion 51
2.10.6 Electro-anatomical Mapping 58
2.10.7 Non-contact Mapping 61
3 Electrophysiologic Simulations 66
3.1 Introduction 66
3.2 Ventricular Model 67
3.3 Model Time Factor 68
3.4 Scar Tissue Description 69
3.5 Excitation and Conduction Rules 72
3.6 Action Potential Simulation 77
3.7 Dynamic Refractory Period 80
3.7.1 Restitution 80
3.7.2 Dynamic Action Potential: *Elharrar and Surawicz Method* 82
3.7.3 Dynamic Action Potential: *Chernyak Method* 83
3.8 Dipole Moment Generation 86
3.8.1 Dipole Magnitude 86

3.8.2 Dipole Direction 88
3.9 Potential Field Generation 89
3.10 Electrophysiologic Simulation Results 90
3.11 Discussion of Electrophysiologic Simulation Results 97
4 Brute Force Inverse Algorithm 99
4.1 Introduction 99
4.2 Forward Problem 100
4.2.1 Unbounded Model 101
4.2.2 Bounded Model 101
4.2.3 Electrode Distribution 103
4.2.4 Noise 104
4.3 Inverse Problem 104
4.4 Single Equivalent Moving Dipole 105
4.5 The 3 plus 3 Parameter Optimization Method 106
4.6 Ablation Site 108
4.7 Exit Site Criteria 109
4.7.1 Dipole Magnitude 110
4.7.2 Distance Between Consecutive Dipoles 110
4.7.3 χ^2 and RNMSE 110
4.8 Brute Force Inverse Algorithm Description 112
4.9 Research Methods 114
4.10 Dipole Trajectories 115
4.11 Slow vs. Fast VT 115
4.12 Brute Force Inverse Algorithm Results 116
4.12.1 Unbounded Model Results: Slow VT 117
4.12.2 Unbounded Model: Fast VT 119
4.12.3 Bounded Model: Slow VT 122
4.12.4 Bounded Model: Fast VT 125
5 Ablation Site Localization in Slow and Fast VT 128
5.1 Introduction 128
5.2 Catheter Dipole Method 131
5.3 Catheter Dipole Method Results 137
5.4 Trajectory Pace-Mapping Method 140
5.4.1 Trajectory Pace-mapping Method for Slow VT 142
5.4.2 Results: Trajectory Pace-mapping Method for Slow VT 149
5.4.3 Trajectory Pace-mapping Method for Fast VT 154
5.4.4 Results: Trajectory Pace-mapping Method for Fast VT 158
6 Summary of Results and Future Goals 164
6.1 Completed Research Objectives 164
6.2 Detailed Summary of Results 164
6.3 Future Direction of Research 167

Chapter 1

Introduction

1.1 Thesis Motivation

A malfunction of the heart's electrical behavior is the principal cause of sudden cardiac death, a major health problem in the U.S.[1] In fact, there were a reported 400,000 to 450,000 sudden cardiac deaths per year from 1989 to 1998, despite major advances in the prevention and medical treatment of cardiac disease.[2] The vast majority of these deaths are due to tachyarrhythmias, or fast heart rates. There are two types of tachyarrhythmias. The first is tachycardia, which consists of a rate greater than 120 beats per minute. The second is fibrillation, which consists of a rate greater than 350 beats per minute.[3] Sudden death is attributed mostly to Ventricular Tachycardia (VT) that rapidly deteriorates to Ventricular Fibrillation (VF).[4,5] Successful eradication of this potentially deadly arrhythmia requires knowledge of the causes of VT and identification of patients who are susceptible to developing VT.

Ventricular tachyarrhythmias are caused by one of three basic mechanisms: abnormal automaticity, triggered activity, or reentry.[6] Automaticity is a property in which the cardiac cells have the ability to spontaneously generate propagated impulses and function as pacemaker cells.[1] Under normal conditions, cardiac cells do not exhibit spontaneous action potentials, or impulses. Triggered activity is premature activation caused by one or more preceding impulses. Reentry is the return of the same impulse

into a zone of heart muscle that it has recently activated. Both automaticity and triggered activity occur in the presence or absence of structural heart disease. However, most symptomatic ventricular arrhythmias occur in patients with structural heart disease and are thought to be mediated by reentry.

Ventricular Tachycardia frequently occurs in the setting of a patient with a prior myocardial infarction and the tachycardia arises from the reentrant electrical conduction circling the subsequent scar tissue, thus leading to formation of a reentry circuit. The reentry circuit entrains the natural pacemaker of the heart, leading to a continuous rapid heartbeat that impairs normal functioning and prevents the ventricles from filling properly, thus causing effective pumping to stop. This drastic decrease in cardiac output and blood pressure can cause collapse and death.[7] Another obstacle faced by VT patients is the existence of multiple reentry circuits. Due to the difficulty in defining these reentry circuits, 30-40% of patients with scar-related VT undergo unsuccessful Radio-Frequency Ablation (RFA) attempts.[8]

Radio-Frequency Ablation involves the localization of a reentry circuit's exit site, or VT site of origin, via induction of the arrhythmia and delivery of radio-frequency energy to that site for termination of the arrhythmia. If the patient is hemodynamically stable during VT, target sites for ablation may be identified in the electrophysiology laboratory with various mapping techniques.[56,57] One of the most popular mapping techniques, pace mapping, consists of pacing from a catheter at multiple ventricular sites during normal sinus rhythm to obtain the ECG morphology identical to that of the VT.

Ventricular Tachycardia may be unstable due to the collapse of blood circulation mechanics (hemodynamic collapse), frequent changes from one form of VT to another, or

inability to reproducibly induce the VT.[9] Unfortunately, 25% of patients who are considered safely treatable are hemodynamically unstable and cannot tolerate the multiple inductions of the arrhythmia necessary in the current catheter ablation technique.[10] For those VT patients who are hemodynamically stable, the RFA procedure is successful in permanently terminating the VT in only approximately half of the cases.

Therefore, the need for an approach to the ablation of VT that accurately localizes the exit site of the reentry circuit and is safe for unstable patients is evident. We believe the Single Equivalent Moving Dipole (SEMD) model and inverse problem in cardiology, both of which will be described later, may be utilized to localize the site for ablation and guide the ablation catheter during the RFA procedure to that localized site for successful ablation of VT.

1.2 Thesis Objectives

The current Radio-Frequency Ablation (RFA) procedure involves mapping of the reentry circuit, which requires the patient to tolerate sustained VT for a prolonged period of time. This requirement limits the availability of RFA to patients with slow, hemodynamically stable VT, which in effect excludes most patients with VT. We developed an approach to RFA that would be more widely applicable than the current technology because localization of the exit site of the reentry circuit, or VT site of origin, would be accomplished through analysis of a single beat of VT. The objective of this thesis is to determine in a simulation model if one can guide a catheter to the VT site of origin using body surface potentials in order to ablate that site with radio-frequency energy. We thus sought to design a finite element model to simulate VT resulting from reentry, develop an algorithm to localize the site of origin of VT through analysis of body

surface potentials, localize the ablation catheter in both slow and fast VT, and advance the ablation catheter to the localized VT site of origin.

Our first objective was to develop a finite element model of ventricular electrical activity in order to simulate various rates of VT resulting from reentry. The model is simple and deterministic, providing a straightforward method for generating body surface potentials corresponding to ventricular electrical activity. Because we are interested in the case of VT resulting from structural heart disease, we superimposed an area of scar tissue on the ventricular model to accommodate the formation of reentry. Through the development and application of excitation and conduction rules using a cellular automata model, we were able to successfully generate electrocardiograms for both slow and fast rates of VT.

Our second objective was to develop an algorithm to localize the VT site of origin from a single beat of VT. This algorithm, the Brute Force Inverse Algorithm (BFIA), estimates the cardiac dipole parameters of a Single Equivalent Moving Dipole (SEMD) representation of cardiac electrical activity from the body surface potentials at each point during the cardiac cycle. The SEMD model represents the heart as a bioelectrical source represented by a single equivalent dipole whose location, magnitude and direction varies throughout the cardiac cycle. For each point in time, the BFIA estimates the location and moment of a single equivalent moving dipole resulting in a trajectory in space of cardiac dipoles. Finally the dipole trajectory is analyzed to determine which point corresponds to the VT site of origin.

Our third objective was to localize the ablation catheter and advance it to the VT site of origin. To guide the catheter to the VT site of origin in slow VT, we developed

the Catheter Dipole Method. In this method we applied sub-threshold current pulses at the catheter tip. The resulting body surface potentials were used as input to the Brute Force Inverse Algorithm, which estimated the parameters of the dipole corresponding to the current pulses, specifically the location of the dipole. By analyzing the SEMD trajectory from the VT simulation (bioelectrical source), the dipole corresponding to the VT site of origin can be identified. A catheter advancement algorithm was used to move the catheter dipole to the VT site of origin dipole. The Catheter Dipole Method was successful in localizing the VT site of origin in slow VT, but was unsuccessful in fast VT. This is because in fast VT, remote ventricular electrical activity altered the body surface potentials generated by the bioelectrical source dipole at the VT site of origin but not the body surface potentials generated by the catheter source.

To guide the catheter to the VT site of origin in fast VT, we developed the Trajectory Pace-mapping Method. In this method we applied supra-threshold current pulses to the catheter tip to stimulate the ventricular myocardium. The resulting body surface potentials at each point in time were used as input to the Brute Force Inverse Algorithm to estimate the parameters of the corresponding SEMD, resulting in a trajectory in space of cardiac dipoles. The resulting catheter dipole trajectory was compared to the VT site of origin dipole trajectory. Finally, a catheter advancement algorithm was used to move the catheter towards the VT site of origin until the trajectories converged. We observed dipole trajectory convergence in both slow and fast VT with this method because both the bioelectrical source and the catheter source generate a wave of ventricular depolarization and thus, both sets of localization estimates should be affected equivalently by the resulting remote ventricular electrical activity.

Through the simulation of VT due to reentry, development of the Brute Force Inverse Algorithm for VT site of origin localization through analysis of the SEMD model, localization of the ablation catheter tip through development of the Catheter Dipole Method and Trajectory Pace-mapping Method, and guidance of the ablation catheter to the VT site of origin, we were able to provide a complete simulation of a new approach to RFA. The proposed new RFA procedure would allow therapy for patients who cannot tolerate the maintenance phase and frequent inductions of VT, by increasing the accuracy and speed by which we determine the site for ablation. In principle, our RFA technique only requires a single beat of VT to localize the VT site of origin. The proposed new RFA procedure promises to provide a new rapid and effective means for the treatment of VT. Future animal and human studies are needed to validate the approach to RFA we have developed.

Chapter 2

Background

2.1 Electrical Activity of the Heart

The heart is a hollow chamber whose walls consist of a mechanical syncytium of cardiac muscle cells called myocytes.[1] Myocytes are relatively small, averaging 10–20 μm in diameter and 50–100 μm in length and form extensive connections with one another as illustrated in **Figure 2.1**.[11] The electrical potential difference between the inside of the cell and its surrounding medium is the transmembrane potential.

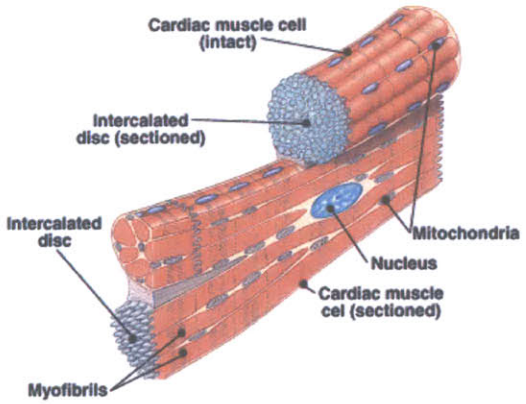

Figure 2.1: Illustration of the cardiac muscle cell.[11]

2.1.1 Cardiac Action Potential

An action potential is the pattern of variation in transmembrane potential when an electrically excitable cell is activated; such activation may be accomplished, for example,

by delivering an electric current of sufficient into the cell.[12] An increase in the value of the transmembrane potential is termed depolarization and a decrease in that value is termed repolarization. The action potential is divided into five distinct phases corresponding to clearly recognizable landmarks in its contour as shown in **Figure 2.2.** The fast depolarization or upstroke refers to phase 0, the fast initial repolarization refers to phase 1, phase 2 is the plateau, the terminal repolarization refers to phase 3, and phase 4 is the resting phase.

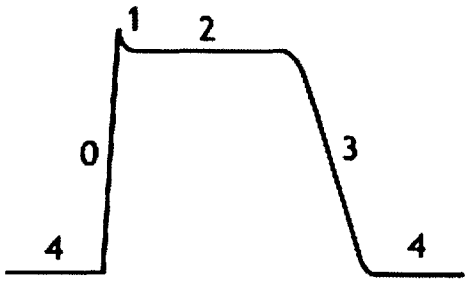

Figure 2.2: Action potential of a ventricular muscle cell denoting the phases of depolarization and repolarization. Phase 0 is the fast depolarization or upstroke. Phase 1 is the fast initial repolarization. Phase 2 is the plateau. Phase 3 is the terminal repolarization. Phase 4 is the resting phase.[13]

Cardiac cells have a semi-permeable cell membrane that allows the passage of some ions while restricting others. The various phases of the cardiac action potential are associated with changes in the permeability of the cell membrane, mainly to sodium, potassium, and calcium ions. Specific ionic currents contribute to each phase of the action potential. These ionic currents are mediated by changes in the specific ionic conductances of individual ionic channels resident in the cell membrane. Flows of positively charged ions (cations) into the cell moves membrane potential in the positive direction, thus causing depolarization. Flows of cations leaving the cell causes

repolarization. Changes in membrane potential resulting from flows of anions (negatively charged ions) are opposite to those just described for cations.[14]

For phase 0, the inward current carried by sodium is the dominant current. During phases 1 and 2, an inward calcium current is opposed by an outward potassium current. An outward potassium current is responsible for repolarization during phase 3. During phase 4, the net current across the membrane is very small leading to a stable transmembrane potential.[14] One should note that the spread of depolarization over myocardial tissue is fundamentally a synchronous process in which activation of one region of tissue spreads to activate neighboring regions. The process of repolarization, on the other hand, is fundamentally an asynchronous process in which local clocks determine the length of time during which a region of tissue remains depolarized and thus refractory to further stimulation.

2.1.2 Cellular Transmembrane Currents

During the plateau of the action potential, as shown in **Figure 2.3**, calcium enters the myocardial cells through calcium channels, which activate and inactivate much more slowly than do the fast sodium channels. When the myocardial cells rest, calcium is taken up by the sarcoplasmic reticulum for subsequent release. However, there is a lag of about 500 to 800 msec before the calcium becomes available for release from the sarcoplasmic reticulum in response to the next depolarization.[15] The resting cell membrane is relatively permeable to potassium but much less to sodium and calcium. The concentration of potassium ions inside a cardiac muscle cell is far greater than the concentration outside the cell. The reverse concentration gradient exists for sodium and calcium ions. These ionic concentration gradients are maintained over a long time scale

(compared to the duration of an action potential) by ionic pumps located in the cell membrane.

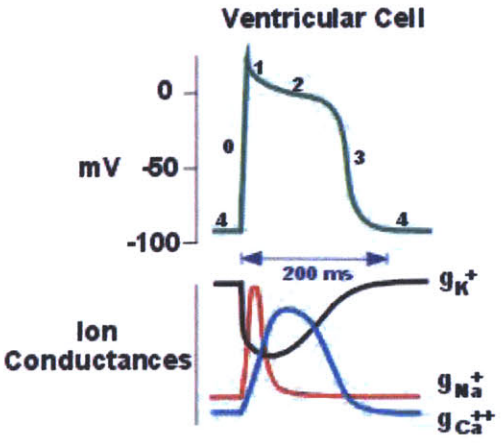

Figure 2.3: Changes in the conductances of sodium (g_{Na}), calcium (g_{Ca}) and potassium (g_K) during the various phases of the action potential.[16]

The flow of the i^{th} ionic species is determined by the conductivity of its channel, g_i and its equilibrium potential, V_i, which is given by the Nernst equilibrium equation:

$$V_i = \frac{RT}{Z_i} \log_{10} \frac{\eta_i^{outside}}{\eta_i^{inside}}. \tag{2.1}$$

In Equation (2.1), R is the ideal gas constant, T is the absolute temperature, Z is the valence of the electron, and η is the molar concentration of the ion.

The relation between the (outward) current carried by a specific ion channel, I_i, and membrane potential, V_m, can be described by the equation,

$$I_i = g_i \cdot (V_m - V_i) \tag{2.2}$$

where V_i is the Nernst potential of the i[th] ion and g_i is the conductance of the i[th] ion.[14] The resting potential can be calculated from the above equation by setting the sum of all ionic currents to zero and is given by:

$$V_m^0 = \frac{g_k}{g_m} V_k + \frac{g_{Na}}{g_m} V_{Na} + \frac{g_{Ca}}{g_m} V_{Ca} + \frac{g_0}{g_m} V_0 \tag{2.3}$$

where

$$g_m = \sum_i g_i \tag{2.4}$$

and V_m^0 is the resting potential and g_m is the total membrane conductance for the potassium (K), sodium (Na), calcium (Ca), and other (O) ions.[1] In the resting state the cell membrane is much more permeable to potassium than to other ions, hence $g_k/g_m \approx 1$. As a result, the resting potential is close to V_k: typically -80 to -90 mV in ventricular myocardial cells. Conversely, at maximum depolarization during the action potential when sodium conductance dominates total conductance, the membrane potential increases towards the Nernst potential for sodium of 40 mV.

In addition to the ionic currents, there is a capacitive transmembrane current:

$$I_c = C_m \frac{dV_m}{dt} \tag{2.5}$$

where C_m = 1 μF/cm^2 is the specific membrane capacitance and V_m is the transmembrane potential.[17] In a space clamped cell, in which we ignore the effects of propagation, the sum of the ionic currents and capacitive current sum to zero as follows:

$$I_m = C_m \frac{dV_m}{dt} + g_i \cdot (V_m - V_i) = 0 \tag{2.6}$$

where I_m is the total membrane current, V_i is the Nernst potential of the i^{th} ion, and g_i is the conductance of the i^{th} ion.

The ionic specific conductances are time-dependent functionals of the past history of the transmembrane potential. This relationship is a consequence of the biophysical effect of the transmembrane potential on the conformational states of the ion specific channels responsible for the specific ionic conductances.[12] The cardiac action potential results from effects of a change in transmembrane potential on ionic conductances which in turn lead to changes in transmembrane currents which in turn lead to changes in the transmembrane potential.

2.1.3 Refractory Period of the Action Potential

For some time after an action potential begins, the membrane will not respond normally to a second stimulus. This time is called the refractory period and can be divided into the absolute refractory period and relative refractory period as illustrated in **Figure 2.4**. The total duration of an action potential is typically 200-300 msec. In the absolute refractory period, the membrane cannot respond at all, because the sodium channels are either already open or closed and inactivated. In a ventricular muscle cell, the absolute refractory period lasts approximately 200 msec, spanning the duration of the plateau and the initial period of rapid repolarization. The absolute refractory period is followed by a shorter (50 msec) relative refractory period. During this period, the voltage-regulated sodium channels are closed but can open. The membrane will respond to a stronger-than-normal stimulus by initiating another action potential. A cardiac action potential, once started in a cell, propagates by local current spread.

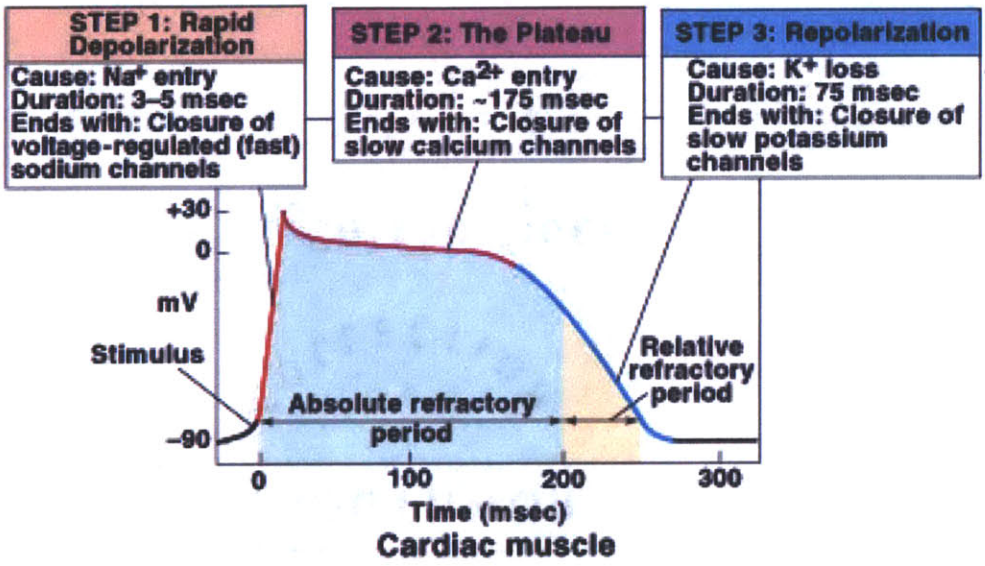

Figure 2.4: Action potential and ion conductance in cardiac muscle.[23]

2.2 Heart Anatomy

The heart muscle has four chambers as illustrated in **Figure 2.5**.[18] The upper chambers are called the left and right atria while the lower chambers are called the left and right ventricles. A wall of muscle called the septum separates the left and right atria and the left and right ventricles. The left ventricle is the largest and strongest chamber in the heart. The left ventricle's chamber walls are only about a half-inch thick, but they have enough force to push blood through the aortic valve and the body's entire vasculature.

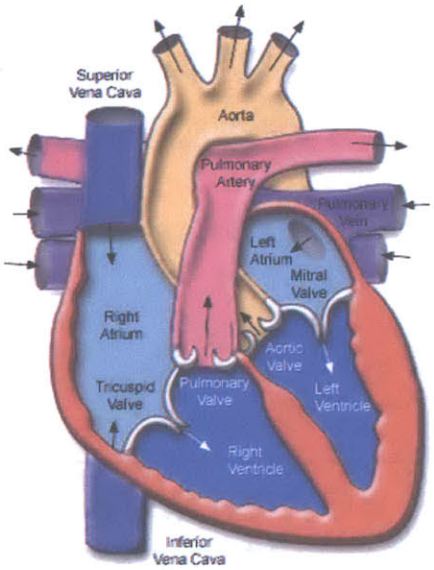

Figure 2.5: Anatomy of the human heart.[18]

2.3 Electrical Conduction System of the Heart

The electro-conduction system of the heart is a complicated system that begins in the right atrium at the sino-atrial (SA) node as illustrated in **Figure 2.6**. The SA node, a small bundle of cells located on the back wall of the right atrium, serves as the natural pacemaker for the heart. The SA node fires an electrical impulse that is spread across the right atrium and to the left atrium by the Bachman's bundle so that both atria contract synchronously.[19] The contraction of the atria forces blood from the atria to the ventricles through their respective valves.

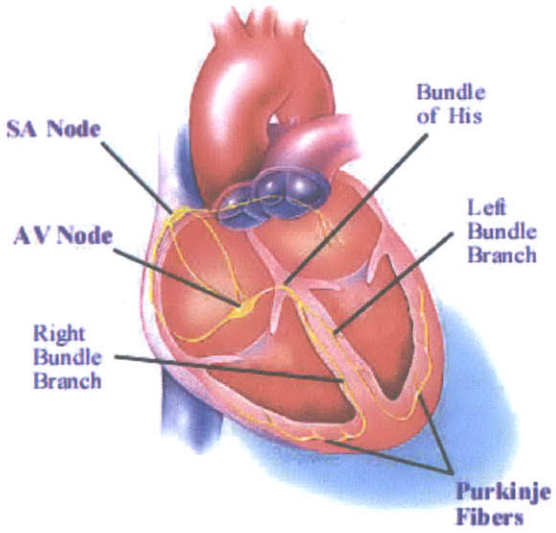

Figure 2.6: Electrical conduction system of the heart.[20]

The impulse that begins at the SA node travels to the atrio-ventricular (AV) node, where the AV node acts as a delay line to slow down the action potential along the internal electro-conduction system. This is done so that all of the blood from the atria can be emptied into the ventricles before the ventricles contract.[19] The action potential then travels from the AV node to the Purkinje fibers. The Purkinje fibers are arranged in two bundles, one bundle branching to the muscle in the right ventricle and the other branching to the muscles in the left ventricle. The action potential moves through these fibers very rapidly and spreads throughout the ventricles at 2 - 4 m/sec. This causes the ventricles to contract in a synchronous manner and forces the blood through their respective valves out to the body at an extremely fast rate. The contraction of the ventricles is termed systole and relaxation of the ventricles is termed diastole.[21]

Because of the electrical activity of the myocardial cells, current flows within the body and potential differences are established on the surface of the skin. The graphical

recording of these body surface potentials as a function of time, is represented by the electrocardiogram (ECG).[1] The signals are detected by means of metal electrodes attached to the extremities and chest wall and are then amplified and recorded.

The electro-conduction of the heart starting at the SA node and traveling through the AV node to the Purkinje fibers creates a mass electrical signal that is detected by the ECG. The letters on the ECG represent different functions that occur in the heart. The P-wave represents atrial contraction, the QRS complex represents ventricular contraction, and the T-wave represents ventricular repolarization, all of which are illustrated in **Figure 2.7**. Examples of normal, fast, slow, and irregular electrocardiograms are also shown. Disturbances of the heart's electrical activity may cause significant abnormalities in its mechanical function and are the basis of much cardiac morbidity and mortality. In fact, a malfunction of the heart's electrical behavior is the principal cause of sudden cardiac death.[1]

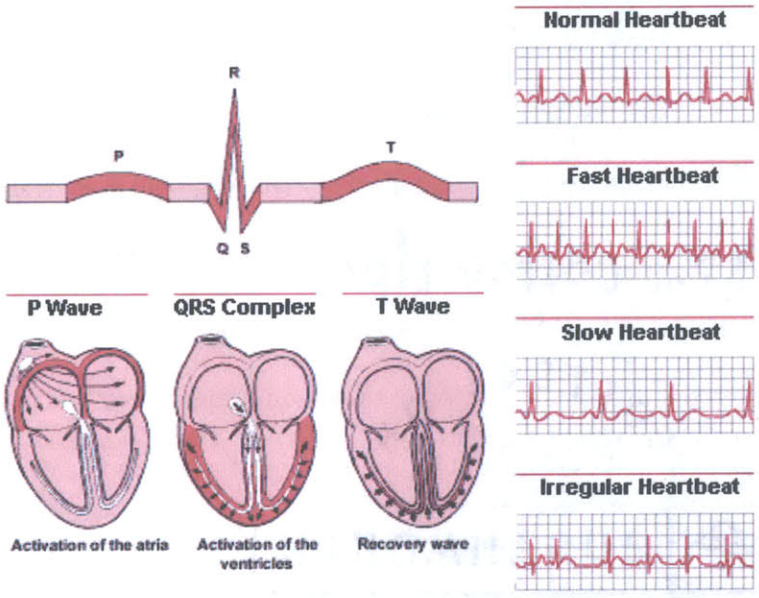

Figure 2.7: Depolarization and repolarization of the heart along with various ECG rates.[22]

The illustration in **Figure 2.8** shows the correlation of the ventricular muscle's action potential and ECG tracing at corresponding times. Ventricular depolarization (phase 0) is represented in the ECG as the beginning of the QRS complex. The initial rapid repolarization (phase 1), due to closing of fast sodium channels, is indicated by the large drop in voltage on the ECG. The plateau (phase 2) during which inflow and outflow currents are balanced is represented when the ECG returns to baseline. Repolarization, (phase 3) when potassium channels open and calcium closes, is shown in the ECG by the T wave. The recovery period (phase 4) is represented in both the muscle tracing and ECG as the return to baseline levels.[23]

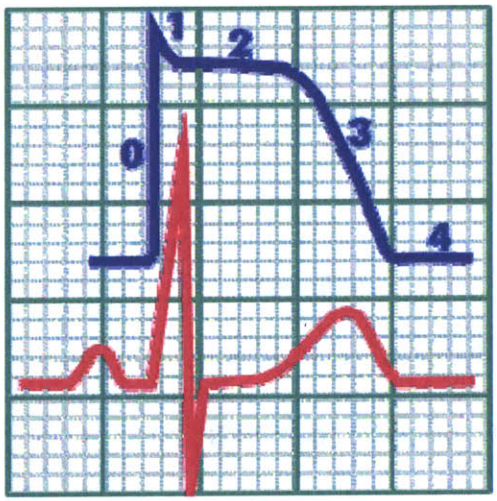

Figure 2.8: Action potential denoting phases of depolarization and repolarization and the corresponding ECG.[23]

2.4 Sudden Cardiac Death

Sudden cardiac death (SCD) is death resulting from an abrupt loss of heart function (cardiac arrest). The time and mode of death are unexpected and it occurs within minutes after symptoms appear.[24] SCD is the most common lethal manifestation of heart disease,

and in many cases it is the first and only symptom.[25,26,27] The high incidence and sudden, unexpected nature, combined with the low successful rate of resuscitation, make SCD a major unsolved problem in clinical cardiology, emergency medicine, and public health.[28,29,30,31] From 1989 to 1998, SCD as the proportion of all cardiac deaths, increased 12.4% (56.3% to 63.9%), and age-adjusted SCD rates declined 11.7% in men and 5.8% in women.[32]

Clinical and pathologic findings suggest that patients with conditions such as coronary artery disease (plaque build-up in arteries that deliver blood to the heart), cardiomyopathy (disease of the heart muscle that causes it to lose pumping strength), hypertensive heart disease (high blood pressure), or arrhythmias (cardiac rhythm disturbances) are at high risk of SCD.[33] In most cases, the mechanism for onset of SCD is a ventricular tachycardia that rapidly progresses to ventricular fibrillation and circulatory collapse.[31,34] Ventricular fibrillation is a lethal, disorganized tachycardia that leads to cessation of effective pumping, cardiac output, and can result in death.

2.5 Ventricular Tachyarrhythmias

Ventricular arrhythmias are a result of abnormalities in impulse initiation or conduction, or both. Tachycardias refer to arrhythmias with three or more complexes at rates exceeding 100 beats per minute; they occur more often in structurally diseased hearts than in normal hearts.[47] Ventricular Tachycardia (VT) originates from a ventricular ectopic focus (prematurely discharging in the ventricle), characterized by a rate typically greater than 120 beats per minute and wide QRS complexes. No absolute ECG criteria exist for establishing the presence of VT. However, several factors suggest VT, including the following: (i) a rate greater than 100 beats per minute (usually 150-200

bpm); (ii) wide QRS complexes (>120 ms); (iii) presence of atrio-ventricular dissociation; and (iv) fusion beats, which have a P wave, broad QRS complex and inverted T wave.[35]

There are two main types of tachycardias, supraventricular and ventricular tachycardia. Supraventricular tachycardias originate from above the ventricles – either from the atria or from the AV node. Generally, supraventricular tachycardias come and go, so they are also known as paroxysmal supraventricular tachycardias. If they last for a sustained period, then they are termed sustained paroxysmal supraventricular tachycardias. In general, ventricular tachycardias carry greater risk to the patient than supraventricular tachycardias.[36]

VT may develop without hemodynamic deterioration (relating to mechanics of blood circulation), yet it often causes severe hemodynamic compromise and may deteriorate rapidly into ventricular fibrillation as shown in **Figure 2.9**. Ventricular fibrillation must be immediately terminated by electric shock to avoid sudden death.

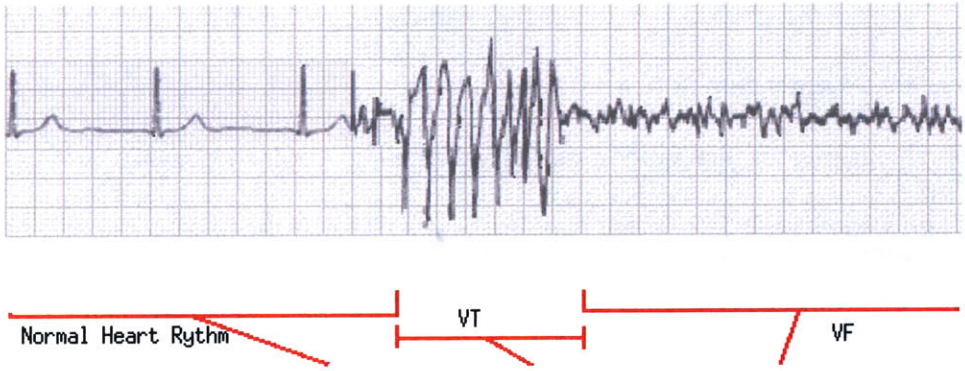

Figure 2.9: A schematic representation of the transition from normal heartbeat to ventricular tachycardia and finally to ventricular fibrillation on an ECG recording.[37]

2.5.1 Ventricular Tachycardia

Ventricular Tachycardias may be classified based on morphology, duration, or underlying mechanisms (substrates).[38] Regarding morphology, the two different morphologies of VT are monomorphic and polymorphic. Monomorphic refers to a regular rhythm originating from a single focus with identical QRS complexes. Monomorphic VT, which is illustrated in **Figure 2.10**, may occur in patients with structural heart disease such as coronary artery disease or may occur in patients without obvious heart disease, also known as idiopathic VT. Polymorphic VT refers to an irregular rhythm and varying QRS complexes and/or axis and is an unstable, malignant form of VT that often degenerates to VF.[39]

Figure 2.10: Monomorphic VT.[39]

Torsade de pointes is a distinctive variant of polymorphic VT, characterized by spontaneous termination (often mistakenly called self-terminating VF) and a distinct cyclic fluctuation of the QRS complex morphology and amplitude. It has unusual shifting-axis QRS complexes that appear on the ECG as if the heart is rotating on an axis as shown in **Figure 2.11**. It typically results from anti-arrhythmic drug toxicity or congenital causes that prolong the QT interval.[35] This arrhythmia may occur with or without either myocardial ischemia (decreased flow of oxygenated blood to heart) or infarction (tissue death caused by obstruction of blood circulation) and episodes are often self-terminating, but can be rapidly fatal if they persist.

Figure 2.11: Torsade de pointes.[39]

The duration classification of VT comes in the form of either sustained or non-sustained VT. Sustained VT is defined as VT that either lasts at least 30 seconds or results in hemodynamic collapse. It is most often caused by reentry within the ventricular heart muscle and usually associated with some form of structural heart disease. Sustained VT can be caused by an accelerated focus in the absence of heart disease. However, the most common cause is chronic ischemic heart disease associated with a prior myocardial infarction. Myocardial Infarction (MI) is usually caused by coronary artery disease (plaque build-up in the arteries that deliver blood to the heart).[35] Sustained, monomorphic VT in patients with coronary artery disease is usually generated by a reentry circuit that incorporates diseased myocardium adjacent to an area of infarction in the left ventricle. Patients with VT after infarction often have multiple reentry circuits with an average of 3 to 4 different inducible VTs.[40]

Non-sustained VT is a run of tachycardia less than 30 seconds duration and does not lead to hemodynamic collapse.[41] Often it is an episode of VT that is short and spontaneously terminating (hence, the term non-sustained) and irregular. This is because the arrhythmia is unstable and cannot establish a stable organized reentrant circuit. Non-sustained VT can cause palpitations, lightheadedness, and even fainting. Non-sustained VT is also associated with cardiac disease but occurs in its absence more often than sustained VT.

Some VTs are caused by underlying mechanisms, which may be due to such substrates as coronary artery disease or dilated hypertrophy (increase in size of the heart). VT usually is a consequence of structural heart disease, with a breakdown of normal conduction patterns, increased automaticity (which tends to favor ectopic foci), and activation of reentrant pathways in the ventricular conduction system.

2.5.2 Premature Ventricular Contractions

A focus within the ventricles that prematurely begins myocardial depolarization results in a Premature Ventricular Contraction (PVC). PVCs are among the most common arrhythmias and occur in patients with and without heart disease. In patients without heart disease, PVCs have not been shown to be associated with any increased incidence in mortality or morbidity. PVCs may occur in up to 80% of patients with previous myocardial infarction, and in this setting, if frequent (>10 per hour) and/or complex (occurring in couplets), they have been associated with increased mortality. However, cardiac mortality in such patients usually occurs in association with significantly impaired ventricular function.[47]

During the PVC, conduction moves more slowly than through the specialized conduction pathways, resulting in a widened QRS complex (greater than 0.12 seconds). The wide QRS complex will either have initially a high amplitude negative or positive deflection as shown in **Figure 2.12**. The direction of this deflection is dependent upon the exact location of the focus.[39] The two ventricles depolarize sequentially instead of simultaneously. PVCs may occur as isolated complexes or may occur in pairs, triplets, or in a repeating sequence with normal QRS complexes. Three or more PVCs in a row is

considered a run of VT. If it lasts for more than 30 seconds or causes hemodynamic collapse, it is termed sustained VT.[22]

Figure 2.12: Premature ventricular contractions.[39]

VT due to hypoxia (oxygen deficiency) can also cause abnormal conduction and lead to regional depolarization. The regional depolarization causes both reduced amplitude action potentials and a decrease in the rate of depolarization, which will slow down the velocity of impulses or completely stop impulse conduction (conduction block).[42] Conduction block can lead to tachyarrhythmias whose most common mechanism involves reentry.[22]

2.6 Reentry

Ventricular Tachycardia is most often caused by reentry within the ventricular heart muscle and is usually associated with underlying heart disease. Reentry is the return of the same impulse into a zone of heart muscle that it has recently activated; sufficiently delayed such that the zone is no longer refractory.[43] Reentrant activity is thought to underlie a great variety of common clinical rhythm disturbances, ranging from the more benign, including SA and AV node reentrant tachycardias, to the more malignant, such as ventricular tachycardia and ventricular fibrillation.[44]

Reentry can take place within a small local region (as shown in **Figure 2.13**) or it can occur globally between the atria and ventricles. This mechanism involves the presence of a unidirectional block within a conducting pathway (usually caused by partial

depolarization) and necessitates critical timing between action potentials. The effective refractory period of the action potentials plays a major role in determining whether or not a reentry circuit will become established.

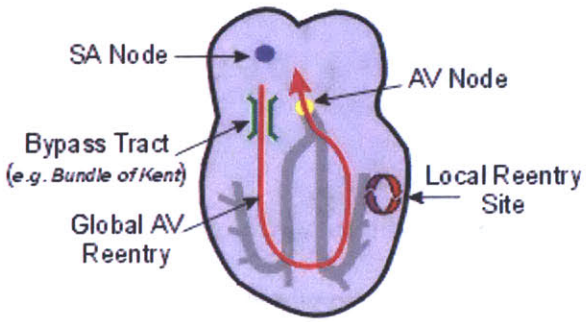

Figure 2.13: Local reentrant circuit.[42]

In the model of reentry shown in **Figure 2.14**, if a single Purkinje fiber forms two branches (1 & 2), the action potential will divide and travel down each branch (top panel). If these branches then come together into a common branch (3), the action potentials will block each other's conduction. An electrode (*) in branch 3 would record single, normal action potentials as they are conducted down the branch. If branch 2 (bottom panel), for example, has a unidirectional block (impulses will travel retrograde but not orthograde), then the action potential traveling down the right branch 1, and into the common distal path (branch 3), will then travel in retrograde fashion through the unidirectional block in branch 2 (blue line). When the block wears off, the impulse may conduct in a retrograde direction back to the origin and then descend again through branch 1, establishing a circular movement, or reentry.[45]

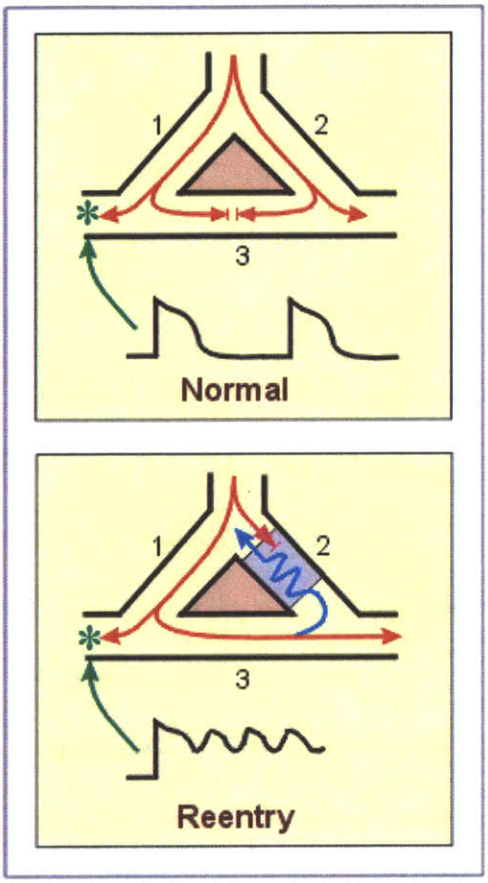

Figure 2.14: Theoretical reentry: 1 is the left bundle branch, 2 is the right bundle brunch and 3 is the common distal path; * represents the electrode placement.[42]

If the action potential exits the block and finds the tissue refractory, then the action potential will dissipate. Therefore, timing is critical in that the action potential exiting the block must find the tissue excitable in order to continue to propagate. If the tissue is not refractory, the action potential can establish a circular pathway of high frequency impulses leading to tachyarrhythmia that can spread throughout the ventricles.

Because both timing and refractory state of the tissue are important for reentry to occur, alterations in timing (related to conduction velocity) and refractoriness can either precipitate reentry or abolish reentry. For this reason, changes in autonomic nerve

function can significantly affect reentry mechanisms, either precipitating or terminating reentry circuits. Many anti-arrhythmic drugs alter the effective refractory period or conduction velocity and thereby affect reentry mechanisms, but some of the drugs have proven to be ineffective and sometimes fatal.

2.7 Anti-arrhythmic Drugs

A number of limitations exist for anti-arrhythmic drug treatment for patients with VT due to infarction. Although the first six months after infarction is thought to be the period of greatest risk for VT and sudden death, some patients develop VT much later. Because the arrhythmia substrate for late VT is relatively fixed, this type of VT tends to be recurrent and difficult to suppress with medications.[46] Anti-arrhythmic drugs were frequently prescribed because they altered the electrophysiological properties of the reentrant circuit and suppressed potential triggers for the development of VT. However, within 2 years, more than 40% of patients treated for sustained VT experienced recurrences.[47]

Suppression of ambient ventricular ectopy by an anti-arrhythmic agent does not prevent future life threatening arrhythmias. For instance, a remarkable study showed that patients effectively treated with class 1C agents in the Cardiac Arrhythmia Suppression Trial (CAST) had a greater risk of sudden cardiac death than those who received placebo, a finding that underlines the pro-arrhythmic potential of these agents.[48] The CAST study findings presented a new awareness, prompting medical professionals to seek alternative methods to anti-arrhythmic drug prescriptions. The Implantable Cardioverter Defibrillator has proven to be a suitable alternative to anti-arrhythmic therapy.

2.8 Implantable Cardioverter Defibrillators

The superiority of the Implantable Cardioverter Defibrillator (ICD) over anti-arrhythmic drug therapy in prolonging survival and preventing sudden death in survivors of sustained ventricular arrhythmias has been supported in three trials.[49,50,51] Thus, the ICD has become first-line therapy for patients with sustained VT. While pacemakers speed up a slow heart rate, ICDs slow down a fast heart rate. Yet, many ICDs also contain a built-in full-featured pacemaker. The ICD automatically detects Ventricular Tachycardia or fibrillation and terminates the arrhythmia by overdrive pacing, high-energy shocks, or both.

The ICD consists of a mini-computer powered by a battery, all sealed in a titanium case.[52] A typical ICD unit is small in size, often four to five ounces in weight, less than two inches wide and a half-inch thick. An example of an ICD implanted in the heart is illustrated in **Figure 2.15**. The battery is connected to a capacitor, which helps the ICD to charge and store enough energy to deliver therapy when required. The ICD lead, which connects the ICD to the heart, is a flexible insulated wire that has an electrode at the tip.

Most ICDs use transvenous leads, which are passed through the vein and carries electrical impulses from the ICD to the heart and information from the heart back to the ICD for assessment by a physician. All ICDs require at least one defibrillator lead, which is placed in the right ventricle. A defibrillator lead has a shocking coil near its tip that delivers defibrillation therapy to the heart. A single chamber ICD uses one pacing lead, placed inside or on the surface of the ventricle. The single and dual chamber ICD refers to the functionality of the built-in pacemaker. A single chamber ICD defibrillates and

paces the ventricle. A dual chamber ICD defibrillates the ventricle and paces the atrium and ventricle.

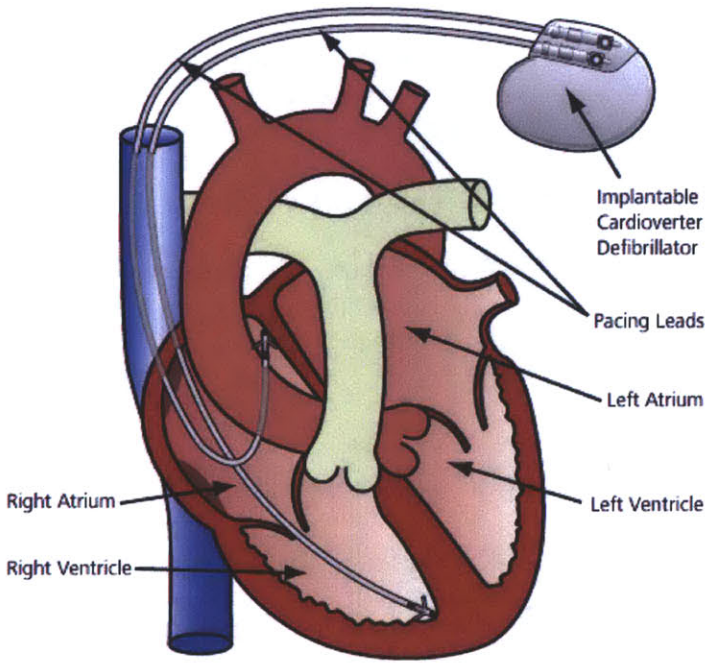

Figure 2.15: Implantable Cardioverter Defibrillator.[52]

To know if, when, and what type of therapy might be needed, the ICD monitors the heart through its computer. The ability to sort out arrhythmias is called discrimination, which is done with algorithms that are designed to ensure patients receive needed therapy, while avoiding unnecessary shocks. The physician can evaluate the ICD's performance and change settings non-invasively. A telemetry wand is placed on the chest over the implanted device, enabling the ICD to communicate with the computer and vice versa. To facilitate programming, the computer software provides high-speed processing and easy operation. At the touch of a button, the unique "Automated Follow-

Up" feature delivers customized information on the ICD function and cardiac activity to help provide therapy specifically tailored to the patient.

The anti-tachycardia pacing therapy actually paces the heart faster than the VT. This application of overdrive pacing allows the ICD to take control of the heart's electrical function, returning it to normal. The patient may feel symptoms of VT, such as dizziness and light-headedness. However, for many patients anti-tachycardia pacing can be so rapid and painless that they may not be aware that they experienced an episode of VT. If pacing does not stop VT, the ICD will deliver stronger impulses. Cardioversion is a low or high-energy shock that is timed to the patient's heart rhythm to stop VT. Cardioversion is usually used when the VT is too fast for anti-tachycardia pacing to be used. Patients often describe cardioversion therapy as an uncomfortable feeling (like a kick in the chest).[53]

Although the ICD is effective in the prevention of death caused by arrhythmias, the device treats the tachyarrhythmia only after it has occurred and does not alter the disorder's natural history. In addition, excessive device activation for patients with incessant VT (frequent episodes) greatly reduces one's quality of life. Thus, utilization of the ICD as an adjunct to catheter ablation might present the best treatment for VT. Ablation can be particularly useful for controlling incessant VT terminated by an ICD. In one series, catheter ablation reduced spontaneous episodes of VT to less than one per month in a selected group of 21 patients who had an average of 134 episodes per month prior to ablation.[54]

2.9 Radio-Frequency Ablation

The treatment of individuals who suffer from arrhythmic episodes has undergone dramatic change. Anti-arrhythmic drugs and implantable devices (pacemakers and defibrillators) have been part of this process, but among the more dramatic developments has been the use of Radio-Frequency Ablation (RFA).[55] Radio-Frequency Ablation, commonly referred to as simply catheter ablation, is applicable to a wide variety of tachycardias, has an extremely high success rate for most supraventricular tachycardias, but has a high rate of recurrence in VT. The presence of multiple morphologies, hemodynamic intolerance, and non-inducible VT has limited the widespread applicability of radio-frequency ablative therapy.[56,57,58] The efficacy of RFA depends on the accurate identification of the site of origin of the arrhythmia, which coincides with the reentry circuit's exit site. Once this site has been identified, an electrode catheter is positioned in direct contact with the exit and radio-frequency energy is delivered through the catheter to ablate the arrhythmia.

Radio-frequency ablation is performed in an electrophysiology laboratory where usually both the diagnosis and ablation can be accomplished in a single session.[59] The procedure can be performed without general anesthesia, but the patient can expect to experience some discomfort. During the procedure, three or four electrode catheters are inserted percutaneously into a femoral, internal jugular, or subclavian vein and positioned within the heart to allow pacing and recording at key sites.[60]

The electrode catheter is connected to a radio-frequency (RF) current generator that delivers an unmodulated sinusoidal RF current between an electrode on an endocardial catheter and a large skin electrode. The current passing through the high

resistance tissue adjacent to the endocardial electrode heats the tissue producing a focal burn.[61] RF ablation produces heating without causing propagated depolarizations or ectopic beats. Radio-frequency lesions are created with the ablation catheter's large distal electrode positioned on the endocardium (inside surface of heart). Up to 50 watts of 500 kHz of RF energy is applied, directly heating a small rim of tissue (resistive heating) as illustrated in **Figure 2.16**. Heat transfer from this region (conductive heating) creates the larger portion of the lesion. Because the catheter tip and heated tissue are cooled by surrounding and intra-myocardial blood flow, respectively, lesions are small, approximately 5mm in diameter.[62]

Radio-frequency ablation is used to treat the most common regular supraventricular tachycardia encountered in clinical practice, AV nodal reentrant tachycardia (AVNRT). Treatment of AVNRT involves a combination of radio-frequency ablation and diagnostic electrophysiological study in a single session. The diagnostic electrophysiological study replicates the clinical tachycardia, to define its mechanism, and to exclude the presence of other arrhythmia mechanisms. Indeed, multiple arrhythmia mechanisms such as the presence of an accessory AV pathway, atrial tachycardia, ventricular tachycardia, or atrial flutter may be present in an individual and the accurate definition and treatment of each tachycardia is important. The results of AV nodal ablation are excellent, with most experienced laboratories reporting well over 95% success rates with minimal risk of serious complications. The risk of recurrent AVNRT is less than 1% for patients with typical slow-fast AVNRT after ablation. The risk of recurrence is higher in patients with atypical forms of AVNRT.[63]

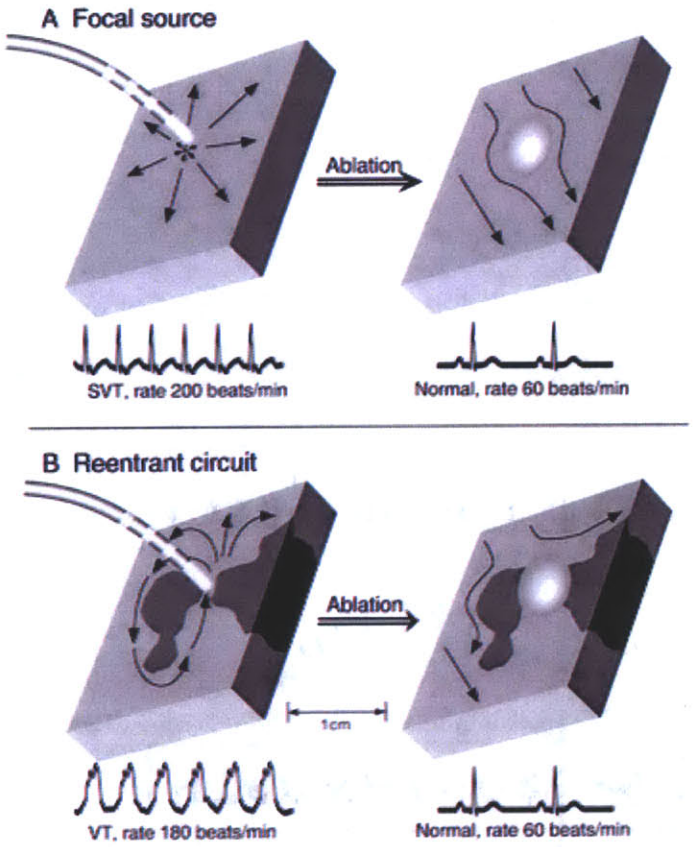

Figure 2.16: How catheter ablation works in different types of tachycardias. Sections of heart muscle where tachycardia originates are depicted. A, A focus (*) is repeatedly firing to cause tachycardia by spreading outward to other cells; the ECG below shows SVT at 200 beats/min. A catheter with a large electrode at its tip is in contact with the focus; after ablation (right), the area of the focus has been damaged and is no longer firing. Arrows show normal electrical propagation and the ECG below is normal. B, A reentrant circuit is shown with electrical propagation around a non-conducting barrier to produce VT at a rate of 180 beats/min, as shown in the ECG below. The impulse must pass through a narrow "bottleneck" to continue. This is an area at which a small amount of damage can eliminate reentry; after ablation, the bottleneck is sealed off, preventing reentry. The ECG rhythm below is normal.[46]

Some ventricular tachycardias contain reentrant circuits that are ill defined, thus radio-frequency ablation therapy is not trivial. In this case, radio-frequency ablation is performed in conjunction with mapping techniques that localize the site of origin of the

arrhythmia. Mapping usually involves multiple inductions of the arrhythmia, which requires the patient to be hemodynamically stable during VT. This requirement limits the availability of RFA to patients with slow, hemodynamically stable VT, which in effect excludes most patients with VT.

Unfortunately, 25% of patients are hemodynamically unstable and cannot tolerate multiple inductions of the arrhythmia.[10] Furthermore, most VT patients never make it to the operating room or electrophysiology lab and for those who are admitted, the current RFA procedure is successful in permanently terminating the VT in only approximately half of the cases. Therefore, increasing the accuracy and speed by which we determine the exit site will result in a more widely applicable RFA procedure. In fact the RFA technique we have developed in principle only requires one beat of VT to localize the site of origin.

2.10 Mapping Techniques

Mapping to identify the origin of ventricular tachycardia is crucial for successful ablation. The approach to mapping is influenced by the size and configuration of the arrhythmia substrate and the arrhythmia mechanism. For small, discrete VT foci, such as those causing idiopathic VT in a structurally normal heart, pace mapping or activation sequence mapping usually provides adequate localization. VT associated with ventricular scars, such as myocardial infarction, are often the result of reentry circuits that can be difficult to define. In this case entrainment mapping is useful along with other additional mapping techniques.[64,76] Detailed mapping of the arrhythmia and sequential positioning of the catheter is required for identification of the arrhythmia's site of origin.

Mapping is attempted and accomplished only when the VT is slow enough not to pose a threat to the safety of the patient.

The consistent beat-to-beat QRS morphology of monomorphic VT indicates a relatively stable reentry circuit or focus that can be targeted for ablation. Polymorphic VT, in which the QRS morphology is continually changing, suggests a wandering arrhythmia source that would not be susceptible to focal ablation.[61] In the case of polymorphic VT, continuous induction of fast VT is not feasible, resulting in the exclusion of many patients for the RFA procedure. The procedure requires that the VT is tolerable to allow localization of the source by mapping during the arrhythmia. We will describe some of the various mapping techniques currently utilized in RFA.

2.10.1 Surface ECG

The surface ECG is probably the most important initial mapping technique in determining the site of origin of VT.[65] On the ECG, the QRS complex represents the spread of the heart's electrical impulse across the right and left ventricles, which contain the left and right bundle branches, respectively. Bundle branch block is a common indicator of abnormal conduction. Because with bundle branch block, the ventricles receive the electrical impulse through the bundle branches sequentially instead of simultaneously, it takes longer for the QRS complex to form. Since the pattern of the spreading of the electrical impulse is abnormal in bundle branch block, the pattern of the QRS complex is also abnormal[66] and is noted by the increase in width from a normal QRS complex.[76]

The QRS morphology during VT is a useful initial guide in identifying the chamber of origin in idiopathic VT, which is typically monomorphic in nature. For focal

VTs, the sequence of ventricular activation is determined largely by the arrhythmia focus. In addition, the ECG can be used to identify the site of origin and diagnosis of VT in scar-based VT. For VT circuits associated with scars, the QRS morphology tends to indicate the location of the reentry circuit exit, but is not always reliable.[67]

The limitations involved with solely utilizing the ECG in determining the site of ablation are obvious. The ECG does not indicate the precise location of the target site for ablation. If solely utilized for catheter guidance, the ECG localization of the ablation site would be too general and lead to permanent destruction of healthy myocardium. Another limitation regarding patients both with and without structural heart disease is the orientation of the heart in the precordium (vertical versus horizontal) can alter the VT ECG morphology. Also, the ECG can be influenced by the presence of large scar, thus it is only useful as an initial step in determining the general location of the VT origin.

2.10.2 Activation Sequence Mapping

Activation sequence mapping is recording activation times from electrograms in an attempt to spatially reconstruct the sequence of myocardial depolarization. The activation times are referenced to a common point, usually the QRS onset during catheter mapping.[64] Activation sequence mapping involves simultaneous sampling from a large number of electrode sites to spatially reconstruct the reentry pathways from activation times and has been used extensively to investigate reentry circuit configuration in humans.[68,69,70,71] The procedure of activation mapping comprises two principal steps: (1) identification of the local activation time at each electrode, and (2) generation of the isochronal map by means of an interpolation algorithm.[72] The principles of activation

mapping are illustrated in **Figure 2.17** for a theoretical reentry circuit in a structurally normal ventricle.

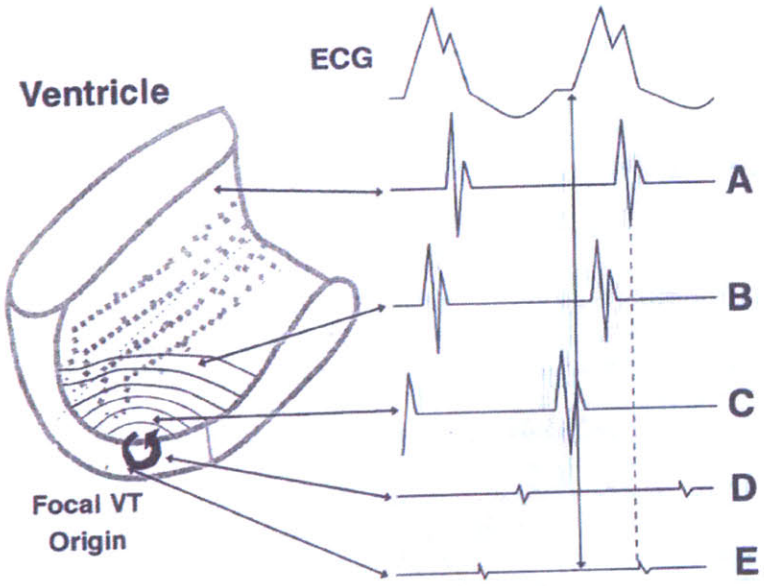

Figure 2.17: The left panel contains a schematic of the left ventricle contains a small reentry circuit. The top right half of the panel contains an ECG while the lower half shows bipolar electrograms at various distances from the reentry circuit (A through E). The recording sites are indicated by arrows extending from the intra-cardiac tracing to the site. The QRS onset is indicated by the vertical arrow. Electrograms recorded near the VT origin (site C) precede the QRS onset. At sites more proximal in circuit (site E), activation time may be similar to that observed at sites distant from the circuit (site A)—represented by dashed line.[64]

The small focal reentrant circuit or automatic focus may occur in the rare instance of idiopathic VT.[73] The concentric lines that spread out from the focal VT origin represent isochrones, which indicate the spread of excitation from the focus. Because the reentry circuit is small, the focal region does not generate enough electrical activity to be detected in the ECG. Thus, the onset of the QRS complex is not observed until a critical

mass of myocardium has been depolarized, which corresponds to the propagation of the reentry wave out of the circuit into myocardium progressively farther from the VT origin. Wavefronts that are propagating perpendicular to the recording dipole of an ECG lead as they leave the focus will not generate a deflection until sufficient vector forces are generated in other directions. This will cause the QRS onset in that lead to occur later than the onset in other leads.[64]

As the recording site is moved further from the arrhythmia focus, electrograms are recorded progressively later during the inscription of the QRS complex, producing a notable phase shift. Identical electrograms can be produced when activation times are similar at the following two locations: (i) sites proximal to the reentry circuit exit site where activation may occur during QRS onset and (ii) sites distant from the circuit as indicated by the dashed line in **Figure 2.17**. Therefore, the timing of a single site relative to the QRS complex may not reliably indicate that the site is in the circuit.

Reentry circuits in abnormal hearts are much more common than the idiopathic VT that may arise in a normal heart. The reentry circuits that give rise to sustained VT late after myocardial infarction can be large and are contained within an abnormal ventricle. A variety of reentry circuit configurations and sizes are possible. Conduction velocity through regions of scar is often slowed and depolarization generates low amplitude electrical signals that are not detectable by the ECG.[68,69,71,74] In addition, the entire reentry path is often undefined, despite electrode recordings from multiple sites throughout the heart. A region of slow conduction through the infarct scar is a common feature of many reentry circuits that have been mapped intra-operatively.

Limitations of activation mapping for use in patients with idiopathic VT include the VT must be sustained, but the majority of idiopathic VTs are non-sustained. The far-field signals sometimes appear early and are not always in the vicinity of the site of origin. In addition, the small, focal reentry circuit does not generate enough electrical activity to be detected in the ECG. Activation mapping alone is not predictive of optimal ablation targets, especially with scar based reentrant circuits that may incorporate a large zone (isthmus) of slow conduction. Difficulty in the identification of slow conduction zones in the reentry circuit may exist due to the small isthmus not manifesting recordable electrical activity.

Additional limitations of activation mapping for use in patients with scar-based reentrant VT include the requirement that VT be hemodynamically tolerated, but about 25% of all scar-based reentrant VTs are too fast to be tolerated to allow sampling at different intra-cardiac sites.[68] In addition, precise timing of local activation is often problematic due to the presence of multiple rapid components, creating a fractionated appearance in the electrogram.[68,69,74] In addition, abnormal electrograms are generated from some areas adjacent to, but not actually within, the reentry circuit at bystander areas.[75]

2.10.3 Pace Mapping

Pace mapping is pacing from an ablation catheter at multiple ventricular sites during sinus rhythm to obtain the ECG morphology identical to that of the clinical arrhythmia.[59] Because many tachyarrhythmias appear to be due to a reentrant mechanism with the impulse traveling in a circuit, a properly timed paced impulse can penetrate and prematurely depolarize part of the circuit, rendering it refractory to the next circulating

wavefront and thereby interrupting the circus movement.[47] It is useful first to compare a 12-lead ECG during the tachycardia with a 12-lead ECG recorded during sinus rhythm for focal VTs. For focal, non-reentrant tachycardias, pace mapping at the VT focus produces a QRS complex identical to that of the VT.[68]

For scar-related reentry circuits, pace mapping can help to focus more precise mapping on areas of interest, but it provides only a limited indication of the circuit exit location and areas of abnormal conduction. At many sites in the reentry circuit, pacing produces a QRS different from that of the VT, particularly if the site is not near the exit. Abnormal conduction during pace mapping in both focal and scar-based reentrant VT, is indicated by a delay > 40 msec between the stimulus and QRS onset (S-QRS) in all 12 leads of the ECG as shown in **Figure 2.18**. However, in scar-based reentrant VT, the specificity is low for reentry circuits.[76]

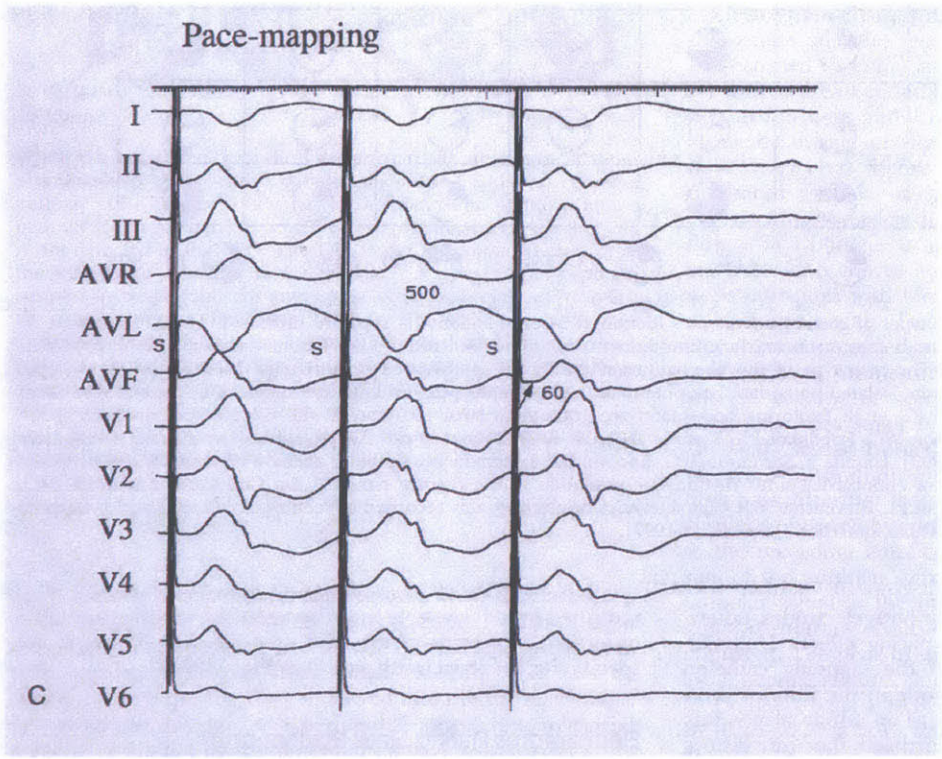

Figure 2.18: Indication of abnormal conduction resulting from pace-mapping where S represents the stimulus.[76]

Pace mapping is extremely limited in indicating the precise VT site of origin for any scar-based VT. Thus, pace mapping for scar-based reentrant VT is usually used in conjunction with entrainment with concealed fusion (ECF), in which specific sites within the reentry circuit can be targeted based on a set of pre-defined criteria.

2.10.4 Entrainment Mapping

Entrainment mapping is a technique to identify ablation sites in a reentry circuit. Reentry circuits associated with scars vary in size, configuration, and location as illustrated in **Figure 2.19**, along with the identification of key areas.

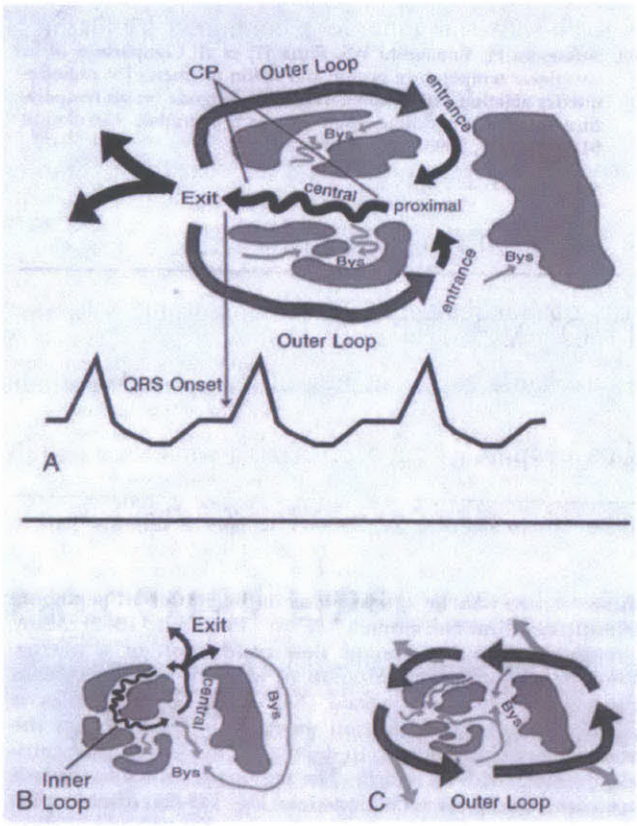

Figure 2.19: Three theoretical reentry circuits are shown. The dark grey areas represent scar tissue resulting from myocardial infarction and the arrow represent the direction of wavefront propagation. (A) shows a double loop (figure-eight) circuit consisting of a central common pathway (CP) and two outer loops. (B) shows a single loop circuit with exit, central, proximal, and inner loop regions. (C) shows a circuit consisting of a single outer loop. Note the exit, entrance, central, proximal and bystander (bys) regions [77]

Depolarization of the *common pathway*, (from *proximal* to *central* to *exit*) occurs during diastole and is not detected in the surface ECG as with many circuits containing a region of slow conduction or a narrow isthmus, or both. It is assumed that diastolic activity also is found on other protected myocardial sites such as the *inner loop* or *bystander*. [78] The regions proximal to the exit are central and proximal regions. After leaving the exit, the reentry wavefront returns to the proximal region by propagating through a loop as shown

in **Figure 2.19B**, which shows an inner loop contained within the scar. An outer loop is a broad sheet of myocardium along the border of the scar as shown in **Figure 2.19A and C**. Outer loop wavefront propagation enters the scar through an entrance. Circuits may be comprised of a single loop or multiple loops.

The majority of scar-related, stable monomorphic VTs are due to reentry with an excitable gap. An excitable gap is an area of repolarized, excitable tissue that can exist between the head of an approaching depolarizing wavefront and the tail of the preceding wavefront as illustrated in **Figure 2.20**.[77] The excitable gap allows appropriately timed pacing stimuli to reset the reentry circuit. The revolution time exceeds the refractory period at all sites, creating at excitable gap between recovery from depolarization and arrival of the next circulating wavefront.

The post pacing interval, PPI, is the time from the stimulus to the return of the stimulated orthodromic wavefront to the pacing site. We can measure the PPI when we pace the ventricle from a site in the region of the reentrant circuit. The VT cycle length (VTCL) is the time it takes VT to travel through the circuit. When pacing at a site in the reentry circuit, the PPI approximates the VT cycle length (VTCL) as shown in **Figure 2.20B and C**. The PPI from the stimulus to the return of the stimulated orthodromic wavefront to the pacing site is equal to the VTCL. In contrast, at bystander sites the PPI exceeds the VT cycle length (**Figure 2.20D and E**). The PPI is the conduction time from the pacing site, to the circuit, through the circuit, and back to the pacing site, and exceeds the VTCL. Analysis of the PPI assumes that the electrogram indicates depolarization of the pacing site by the returning orthodromic wavefront.[76]

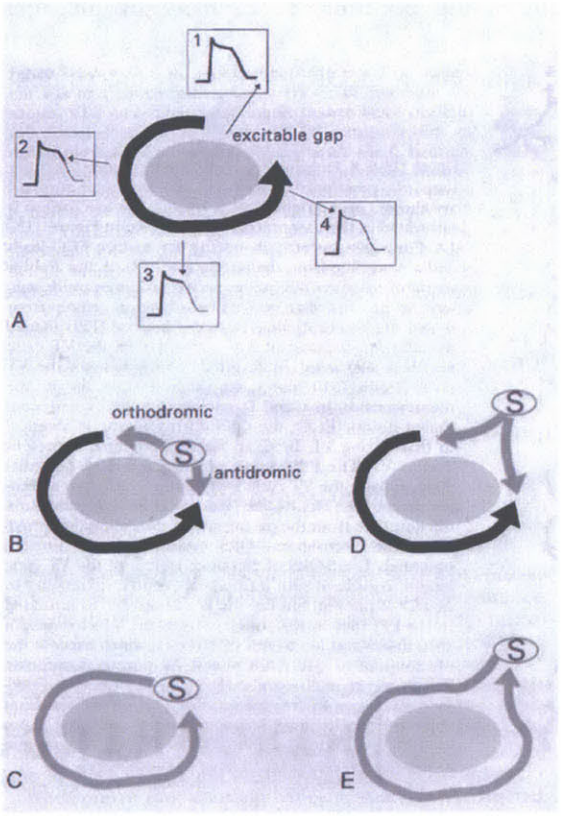

Figure 2.20: Reentry with an excitable gap, resetting, and the post-pacing interval (PPI) are illustrated. The circulating wavefront (solid arrow) propagates around an unexcitable region (gray). Following depolarization, each site is refractory for a finite time. Boxes in A show action potentials at various stages of repolarization from different sites [1, 2, 3, 4] around the circuit. In B, resetting by a stimulus that captures a site in the reentry circuit is shown. The stimulus (S) produces orthodromic and antidromic wavefronts (gray arrows). The antidromic wavefront collides with the returning orthodromic wavefront. In C, the stimulated orthodromic wavefront propagates through the circuit, resetting it. D and E show resetting of the circuit by pacing at a bystander site. A capturing stimulus produces wavefronts that propagate to the circuit and begin traveling in antidromic and orthodromic directions. The antidromic wavefront collides with an orthodromic wavefront and is extinguished. The stimulated orthodromic wavefront travels through the circuit and then returns to the pacing site (E).[77]

Entrainment is the continuous resetting of the reentry circuit by a series of stimuli.[79] In entrainment with QRS fusion, or entrainment for brevity, fusion of two wavefronts, one from reentrant activity in the circuit and one from the stimulus, is observed in the ECG. This fusion results from stimulated wavefronts that alter ventricular activation remote from the pacing site. Note in **Figure 2.21** that the stimulated orthodromic wavefronts (gray arrows) generated from the stimulus (S) do not exit the circuit at the same time as the reentrant activity in the circuit (black arrows).

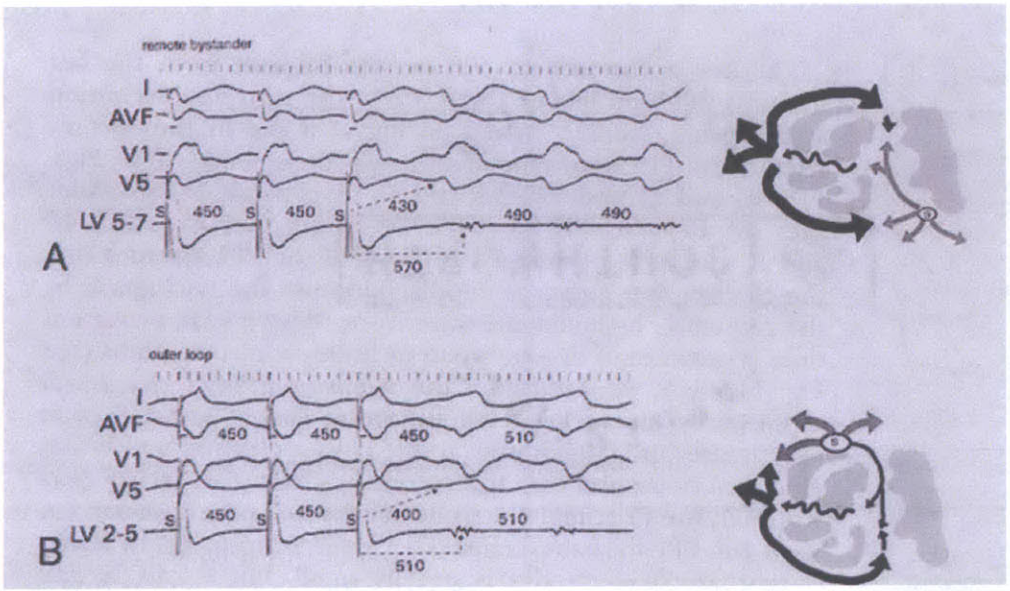

Figure 2.21: Entrainment at remote bystander (A), and outer loop (B) are shown. To the right of each tracing, the mechanism is illustrated in the theoretical reentry circuit. From the top of each tracing are surface ECG leads and a recording from the pacing site (LV). A and B show entrainment with QRS fusion; pacing produces antidromic wavefronts that alter ventricular activation remote from the pacing site. A: Pacing from stimulus (S) at a remote bystander site. B: Pacing within the outer loop of the reentry circuit. All pacing is unipolar and time is in msec.[77]

In addition, the stimulated antidromic wavefronts are not contained in or near the scar, but propagate through other areas of the heart. Thus, it is expected that the ECG would

represent a fusion of the orthodromic wavefront at the exit site fused with the reentrant activity in the circuit at the same exit site.

2.10.5 Entrainment with Concealed Fusion

Entrainment with concealed fusion (ECF) is entrainment by stimuli that do not alter the QRS morphology. The lack of QRS fusion is due to failure of the stimulated wavefronts to alter ventricular activation. As the illustration of ECF shows in **Figure 2.22C and D**, the stimulated orthodromic wavefront leaves the exit at the same time as VT, utilizing the same exit.

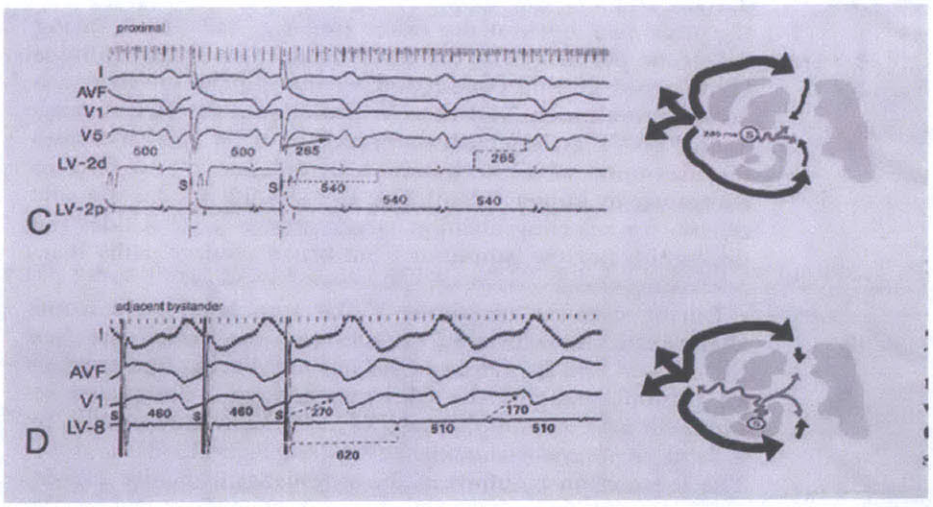

Figure 2.22: Entrainment at proximal (C) and adjacent bystander sites (D) are shown. To the right of each tracing, the mechanism is illustrated in the theoretical reentry circuit. From the top of each tracing are surface ECG leads and a recording from the pacing site (LV). In C and D, pacing entrains VT with concealed fusion (ECF); the QRS during pacing is identical to that during VT. In C, an isolated potential is present and the PPI measured to the isolated potential approximates the VTCL, consistent with a reentry circuit site. All pacing is unipolar and time is in msec.[77]

The stimulated antidromic wavefronts are contained in or near the scar by collision with a returning orthodromic wavefront and by regions of conduction block.[57] The term entrainment with concealed fusion stems from the fact that fusion occurs between orthodromic and antidromic wavefronts at the electrogram level within the scar. However, this fusion is concealed, or not apparent on the surface ECG.

During sinus rhythm, potentials that occur after the end of the QRS complex, designated late potentials, are associated with abnormal conduction and with isolated potentials during VT. Abnormal sinus rhythm electrograms are usually present at exit, central, and proximal sites, but they also occur at bystanders.[76] Isolated diastolic potentials are low-amplitude electrograms that occur during electrical diastole, between QRS complexes as shown in **Figure 2.22C**. They often arise from a reentry circuit isthmus, but can also occur in bystander areas; as indicated by dissociation of the potential from the VT during entrainment, or initiation of the VT.[80]

Because entrainment with concealed fusion can occur during pacing at bystander sites adjacent to the reentry circuit, additional criteria are needed to distinguish reentry circuit sites from bystanders. From evaluating the PPI, Stevenson and coworkers found that at 53 ECF sites, 25% were in bystander areas and 75% were in the reentry circuit.[64] ECF use of the PPI to distinguish reentry circuit sites from bystander sites is based on the assumption that the conduction time through the reentry circuit remains the same during entrainment as during VT.[57,81] When conduction velocity slows during pacing, prolonging the revolution time through the circuit, the PPI lengthens, exceeding the VTCL. Therefore, if the PPI significantly exceeds VTCL, we know that pacing is occurring at a bystander site.

At inner loop and common pathway sites, pacing entrains tachycardia with concealed fusion and a PPI *approximating* the VTCL. Pacing in an outer loop entrains or resets the tachycardia with QRS fusion, but with PPI *matching* the VTCL. As confirmation of our earlier discussion of PPI, note that when pacing within the circuit, the PPI = VTCL (**Figure 2.21B** and **Figure 2.22C**), but when pacing outside the circuit, at a bystander site, PPI > VTCL (**Figure 2.21A** and **Figure 2.22D**).

Several measurements for identifying reentry circuit components during entrainment are critical. The first measurement is to consider the difference between PPI and VTCL. A minimum PPI-VTCL difference $\leq$ 30 msec increases the likelihood of VT termination by five-fold, as compared to longer PPIs.[57] However, the PPI should not be the sole criteria for selecting ablation target sites because it does not distinguish narrow isthmuses from broad reentry paths (e.g. outer loop sites).[76] As can be seen in **Figure 2.23**, the PPI-VTCL difference of $\leq$ 30 msec can inform you if you are pacing at an outer loop, remote bystander or adjacent bystander sites. However, additional criteria are need for isthmus and inner loop site information.

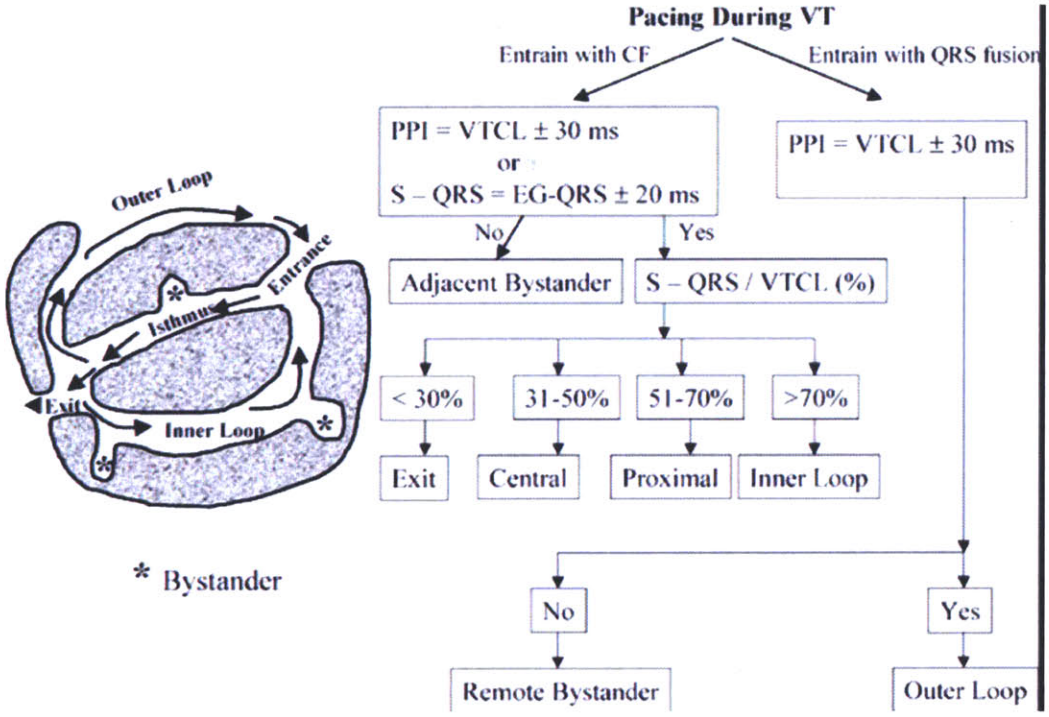

Figure 2.23: The cartoon and adjacent panel represent the criteria for determining different components in a scar based reentrant VT circuit by entrainment mapping. Highest success for ablation lesions is in the isthmus followed by exit site. CF represents concealed fusion and EG represents electrogram.[82]

A second measurement to observe is the difference between the S-QRS interval and the interval between the onset of the electrogram deflection and onset of the corresponding QRS complex, EG-QRS. The S-QRS interval is the time from the stimulus to the QRS onset and the EG-QRS interval is the time from the electrogram deflection to the QRS onset. The S-QRS is short at exit, and longer at central, proximal, and inner loop sites as shown in **Figure 2.23**. The S-QRS interval also aids in the identification of bystander sites. At reentry circuit sites, but not bystander sites, the S-QRS during ECF equals the EG-QRS interval during VT, provided that pacing does not alter conduction. Stevenson and coworkers found that an S-QRS and EG-QRS difference

of $\leq$ 20 msec may indicate a reentry circuit site.[64] They determined that a short S-QRS and EG-QRS difference may indicate a reentry circuit site, but a long difference may not reliably indicate that the site is remote from the circuit. The reasons for this are not clear but may possibly result from the stimulated wavefront taking a slightly different path than the tachycardia when exiting the reentry circuit. In addition, entrainment with subtle QRS fusion may not have been detected on the ECG lead used to access the QRS morphology during pacing.

A third measurement to consider is the ratio, S-QRS/VTCL, which provides information regarding whether or not the pacing occurs at exit, central, proximal or inner loop sites. ECF with either an S-QRS interval less than 70% of the VTCL, or with an isolated diastolic potential, increases the likelihood of VT termination by more than eight-fold, to as high as 70%.[57,86]

In order to clarify the measurements discussed, we have depicted an example with all of the measurements labeled in **Figure 2.24**. Note that the stimulus is at the proximal region of the common pathway, or isthmus, inside the reentry circuit. First, we would expect the PPI and VTCL difference to be less than 30 msec. Secondly, we would also expect the S-QRS and EG-QRS difference to be less than 20 msec. Finally, we would expect the S-QRS/VTCL to lie between 51-70%.

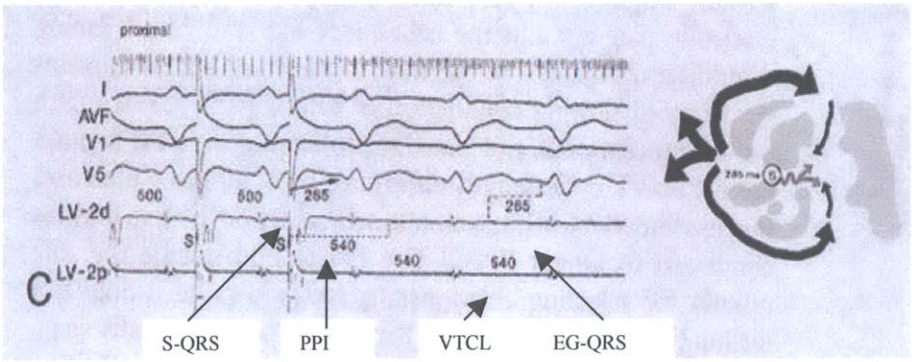

Figure 2.24: Example of electrogram and ECG with measurement indicators.[77]

The criteria to fulfill are as follows: Is the PPI and VTCL difference ≤ 30msec? Yes, the PPI = 540 msec and VTCL = 540 msec. Is the S-QRS and EG-QRS difference ≤ 20 msec? Yes, the S-QRS = 285 msec and EG-QRS = 285 msec. Is the S-QRS/VTCL ratio between 51-70%? Yes, the S-QRS/VTCL = 285/540 = 52.8%. These criteria indicate that the stimulus is in the common pathway, thus a lesion will be formed at that site followed by movement of the stimulus toward the exit site to form a lesion where the S-QRS/VTCL ratio is < 30%.

Multiple morphologies of inducible monomorphic VT are common in patients with scar-related VTs as shown in **Figure 2.25**. Typically three to four VTs per patient are present, increasing the difficulty of mapping and ablation. [57,86] Multiple VTs may originate from different regions, or from a single region of slow conduction, such that ablation in one region abolishes more than one VT.[76] Patients referred for ablation often have recurrent episodes of VT. [40,56] Reentry circuits related to inferior wall infarctions are most commonly located along the basal region of the infarct, near the mitral annulus.[84] In some cases, a surviving rim of tissue beneath the mitral annulus is a critical isthmus where ablation can abolish multiple VTs. Rarely, the successful ablation site is

in the right ventricle.[83] In 20% to 30% of patients, target sites for one or more VTs are not identified from the endocardium.

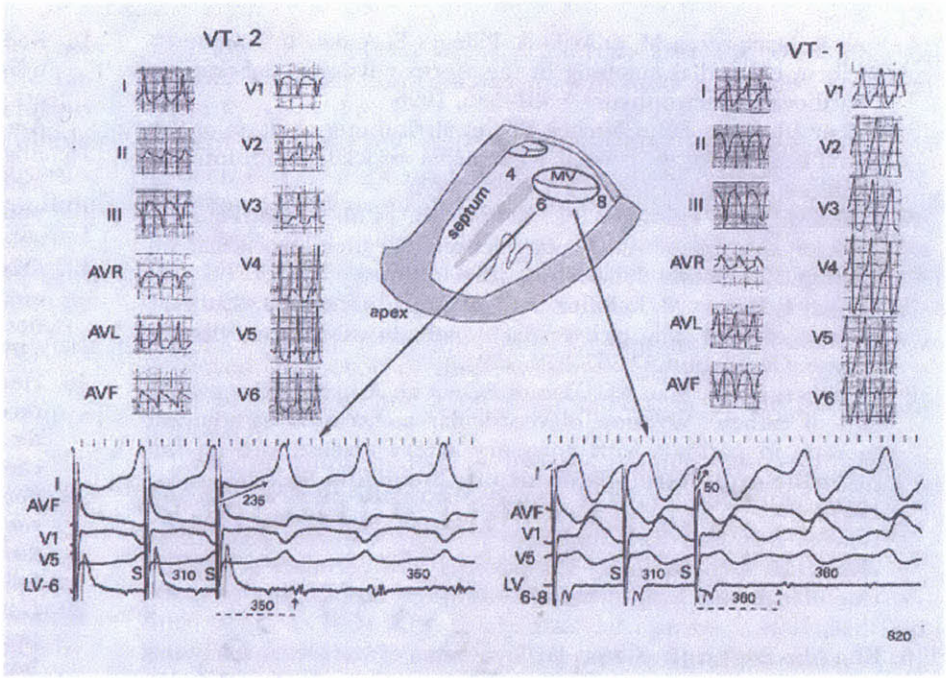

Figure 2.25: ECG tracings and entrainment of two different VTs in a patient with prior inferior wall infarction are shown. VT-2 (*at left*) has a LBBB configuration and dominant R waves in V3-V6 consistent with an exit at the base of the septum. Pacing at LV site 6, beneath the mitral annulus on the inferior wall, produces ECF, a PPI indicating that the site is in the circuit (dashed line), and a relatively long S-QRS (235 msec) consistent with a proximal; site in the circuit. VT-1 (*at right*) has a RBBB configuration and pacing at site 6 to 8, produces ECF, the PPI approximates the VTCL, and the relatively short S-QRS of 60 msec is consistent with an exit site. Ablation in this region abolished both VTs.[84]

When all the criteria of an ideal site are met: (i) a perfect ECG match of paced beats to the VT—ECF, (ii) PPI ≤ 30 msec of VTCL and (iii) pacing S-QRS/VTCL ≤ 50% of VT cycle length—within the isthmus, then 70% of the VTs can be terminated by a limited number of lesions.[85,40,86] Termination of VT by a stimulus that does not produce

a QRS complex is uncommon, but probably indicates the pacing site is in the reentry circuit.[76]

Entrainment with QRS or concealed fusion is not well suited for the study of rapid tachycardias because the techniques require the patient to repeatedly tolerate episodes of sustained tachycardia. The ability of the stimulus to entrain tachycardia depends on the existence of a long enough excitable gap in the reentry circuit.[57] Entrainment can be demonstrated for the vast majority of slow monomorphic VT arising from infarct scars. However, these methods are not suited for polymorphic ventricular arrhythmias. It is likely that abnormal electrograms serve as a useful guide for selecting regions to interrogate further during tachycardia, but they have a low specificity for identifying reentry circuit sites.

2.10.6 Electro-anatomical Mapping

In the past, localization of the mapping catheter electrodes was based on two-dimensional fluoroscopic images. These images clearly define the location coordinates of the electrodes, but because they do not reveal endocardial information, they are insufficient to record the electrode coordinates within the patient's heart. Thus the electro-anatomical mapping system was introduced, which simultaneously reports the recording electrode coordinates together with its electrogram. This mapping system makes use of an intra-body, real-time, high resolution, non-fluoroscopic location and navigation system.[87]

Electro-anatomical mapping is a new, widely used, commercially available mapping technique. The CARTO System (Biosense, Tirat Hacarmel, Israel) is a non-fluoroscopic three-dimensional, catheter based mapping system that creates a replica of

the anatomy of the cardiac chamber at the site of the tachycardia focus or circuit. Historically, significant research efforts were directed to accurately determine the local activation time from unipolar and bipolar electrograms, but little effort was given to achieve a better understanding of the importance of the accurate determination of location. As catheter ablation procedures became more widespread, the need for location-accurate maps was needed.[88]

During the mapping procedure, a locatable mapping catheter is introduced under fluoroscopic guidance and is positioned inside the area of the heart to be mapped. The mapping system determines the location and orientation of the mapping catheter, which is gated to a fiducial point (cross location marker) in the cardiac cycle. The catheter tip is sequentially dragged over the endocardium, acquiring multiple tip locations together with their respective electrograms. The set of gated catheter tip locations is used to reconstruct the 3-D endocardial surface using x-irradiation. The system may be used to identify tag areas where the radio-frequency energy has to be applied, enabling the operator to move the catheter to contiguous sites around the focal origin of the tachycardia for more radio-frequency energy applications, in order to ablate the tachycardia focus.

The system can produce an activation map and a voltage map as demonstrated in **Figure 2.26**. The local activation time at each site is color-coded and incorporated into the endocardial surface reconstruction as a color, in which red represents earliest activation times and purple represents latest activation times. The activation map (**Figure 2.26A**) depicts an entrance to the slow conduction zone (located at the border of the scar, SCZ) and an exit (EXIT). RF energy was delivered to create a line of block

transecting the SCZ (brown tags). In the voltage map (**Figure 2.26B**), red represents scar (< 0.5 mV) and purple represents healthy tissue (> 2 mV). Blue, green, yellow, and red indicate progressively lower-amplitude abnormal regions. The pink tags indicate sites with diastolic electrical activity from the reentrant pathway.

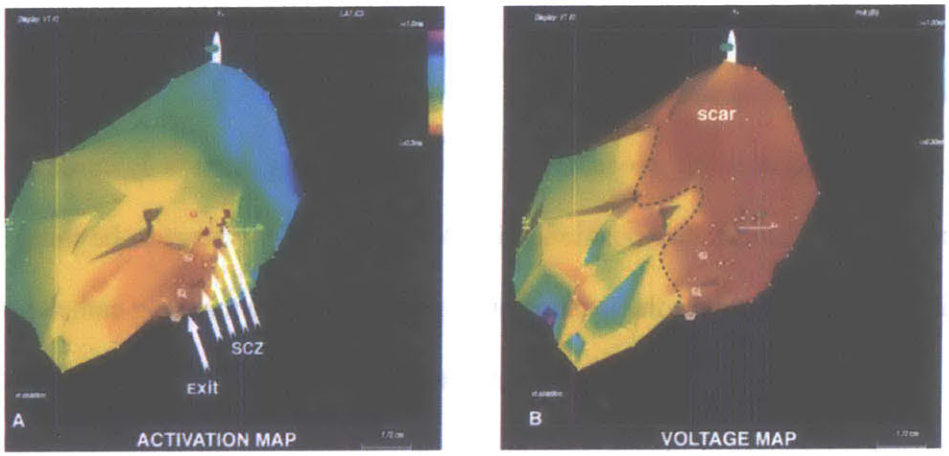

Figure 2.26: Activation(A) and substrate (B) maps (AP view) of a patient with ischemic VT. The substrate (B) map shows, in red, areas of a large low voltage area (corresponding with scar, SCAR). The activation map (A) depicts an entrance to the slow conduction zone (located at the border of the scar, SCZ) and an exit (EXIT) 3 cm more posterior into the normal tissue. The pink tags indicate sites with diastolic electrical activity. This map guided the ablation procedure in which RF energy was delivered to create a line of block transecting the SCZ (brown tags). (Map courtesy of Dr. Karl Heinz Kuck, St. George's Clinic, Hamburg, Germany).

Patient movement is corrected by placing a second locatable catheter on the patient's back. The mapping system subtracts the location of the mapping catheter from the simultaneous location of the reference probe, thus compensating for any patient motion. A correction can also be made for heart movement by placing an internal reference probe in a secure place in the heart chambers, such as in the coronary sinus. Once sufficient anatomical data has been acquired, the operator can navigate without

using fluoroscopy.[88] Before new data is added to the map, the stability of the catheter-endocardial contact is tested for location stability and local activation time stability. Data may also be presented as propagation maps, in which active sites are colored red and quiescent sites are blue. [46]

The CARTO system provides a better understanding of subtleties of pace mapping, leading to accurate targeting of ablation lesions in idiopathic VT. For scar-based reentrant VT, CARTO characterizes the true endocardial extent of scar and border zones. Studies found that repeated electro-anatomical activation and propagation maps during sinus rhythm and pacing were similar and enabled accurate identification of the pacing site in all animal studies.[89] Accuracy was also tested by repeatedly applying radio-frequency energy to a site on the endocardium that was tagged on the electro-anatomical map.[90] These studies indicate that the localization is accurate enough to guide radio-frequency energy to create single, multiple, and long continuous lesions.

Some limitations of the procedure include the fact that only exit sites of the electrical wavefront can be registered, but not the underlying electrophysiological and anatomical structure. Furthermore, electro-anatomical mapping is limited by the fact that it requires a hemodynamically stable tachycardia in order to allow activation sequence mapping.[91] Because the localization methodology is based on recording low-level magnetic fields, large ferromagnetic objects can affect the magnetic field sensed by the catheter sensor (usually when large objects are within 1 cm from the catheter tip).

2.10.7 Non-contact Mapping

Conventional mapping prospects are poor for patients who have rapid hemodynamic deterioration due to rapid rate and depressed ventricular function because

it is not possible to keep these patients in tachycardia during mapping. The concept of rapid endocardial activation mapping using a catheter based system that acquires data simultaneously is attractive and now possible through non-contact mapping. The non-contact mapping system produces endocardial activation maps based on the electrical field detected in the blood pool by a catheter-mounted probe deployed free in the cardiac chamber.[92]

The endocardial electrograms are constructed from the low-frequency, low-amplitude potentials detected in the blood pool[93] by utilizing principles previously applied to the reconstruction of epicardial maps from skin surface electrograms.[94] The technique to enhance and resolve the far-field potentials is based on an inverse solution to Laplace's equation that considers how a signal detected at a remote point (non-contact electrode) would have appeared at the source. An alternative in such unstable patients—now feasible with non-contact mapping—is to transect areas of slow conduction and visualize lines of ablation as they are created and perform the ablation during sinus rhythm.[95]

The Non-contact mapping system (EnSite), as shown in **Figure 2.27**, utilizes a 9 French multi-electrode array (MEA) catheter with 64 electrodes mounted on a 7.5 ml balloon (filled with a contrast/saline mixture to deploy the MEA) to record intra-cavitary far-field potentials. A *French* is the circumference of the tube in mm. The outer diameter (also in mm) is computed by dividing by π.

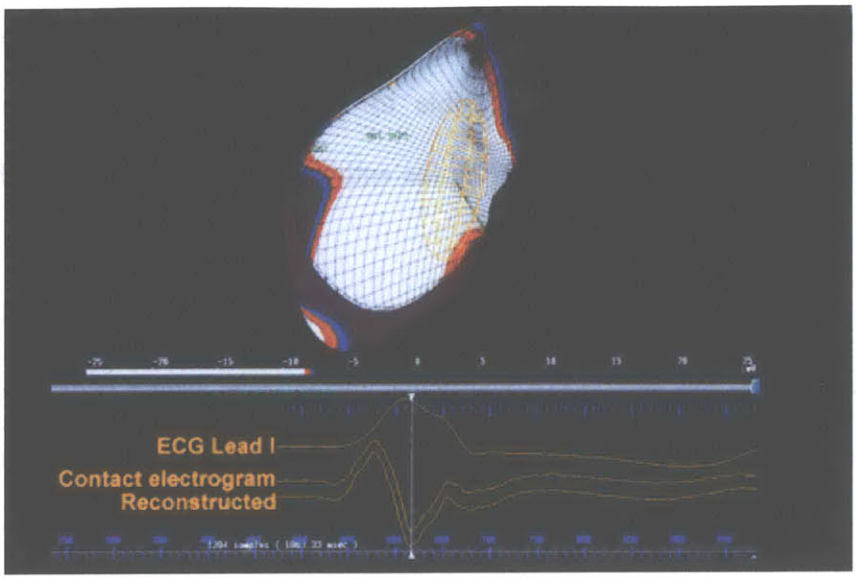

Figure 2.27: Detail from screen of non-contact system workstation. Within the geometric contour of the computer-generated virtual LV endocardium (top), position of MEA is represented as a yellow frame. Lateral wall of virtual endocardium has been removed to reveal endocardial surface. Some anatomic locations, as identified on fluoroscopy, are labeled in green, having been marked on the map by use of the catheter-location system. Inf indicates inferior; Infsept, inferoseptal; Ant, anterior; and Ant Sept, anteroseptal. A reconstructed isopotential map is superimposed onto the virtual LV endocardium. Color scale for the isopotential map, shown as a horizontal line below the virtual endocardium, has been set so that white represents endocardial regions where the potential is <-9 mV and purple represents endocardial regions where the potential is >-8 mV (thus producing an activation map). Green locator signal line emerging from MEA marks the position of the mapping catheter tip on the endocardium. Below the virtual endocardium are waveforms showing surface ECG lead I, contact electrogram from the mapping catheter tip, and reconstructed electrogram at the same location.[96]

The system permits simultaneous multi-site intra-cardiac mapping and has the capability to localize any conventional roving electrode catheter. Using inverse solution mathematics, distortion of the detected electrograms due to noise, measurement errors, or inaccuracies in determining the endocardial geometry, may result in large errors in reconstruction of the electrogram. To compensate for potential distortions in detected

electrograms, stability is provided by using a mathematical technique known as regularization, which make it possible to reconstruct and interpolate up to 3300 electrograms simultaneously, covering the entire virtual endocardium of the chamber in which deployed.[97]

Schilling and coworkers conducted a study of non-contact mapping in the left ventricle during the ablation of ventricular tachycardia, which demonstrated excellent results of the non-contact mapping technology.[98] Of 24 patients with VT undergoing non-contact mapping of VT, 21 patients had ischemic heart disease. Of a total of 81 morphologies of left ventricular tachycardia mapped, the exit site from the diastolic reentrant pathway was demonstrated in 80 (99%). The complete circuit was visualized in 17 (21%) and the exit alone could be identified in 26 (34%). The non-contact mapping system was safely used to map and guide ablation with no complications arising directly from the system.

Limitations include overall decrease in accuracy in reconstructed electrograms as the distance of mapped area from the MEA increases, thus creating problems in mapping large cardiac chambers and complications due to aggressive anticoagulation measures because of MEA deployment in the cardiac chamber expose patients to potential bleeding complications.[99] The MEA catheter has demonstrated limited clinical utility by providing poor spatial resolution. However, with further development of the accuracy, rapidity, and possibly, automation of data analysis, this technology has the potential to not only make the large majority of previously inaccessibly, poorly tolerated VT amenable to mapping and ablation, but also to reduce procedure and fluoroscopy times,

and increase the efficacy of ablation through a better appreciation of the arrhythmia mechanism.[92]

Chapter 3

Electrophysiologic Simulations

3.1 Introduction

The simulation of reentrant arrhythmias was necessary in analyzing the effectiveness of the Brute Force Inverse Algorithm (BFIA) in eradicating Ventricular Tachycardia (VT). We present a simulation model to study the abnormal electrical conduction that arises from ventricular scar tissue, specifically VT that is caused by an underlying reentry circuit. Thus, it is our objective to develop a model whose elements have the characteristics of VT due to a reentry circuit substrate. The model is simple and deterministic, providing a straightforward approach to electrocardiogram (ECG) simulations.

Prior ECG simulations by Smith[100] provided evidence that the spatial dispersion of refractoriness was a sufficient condition to initiate reentrant arrhythmias. The refractoriness of tissue refers to the length of time the tissue has been activated and thus the level of susceptibility for future activation. The "dispersion of refractoriness" hypothesis is rooted in the concept that the spread of depolarization over myocardial tissue is fundamentally a synchronous process in which activation of one region of tissue spreads to activate neighboring regions. The process of repolarization, on the other hand, is fundamentally an asynchronous process in which local clocks determine the length of

time during which a region of tissue remains depolarized and thus refractory to further stimulation.

An alternative approach to testing the dispersion of refractoriness hypothesis in animals and one that allows for gaining additional insight into basic mechanisms is to construct a simple computer model of ventricular conduction processes that explicitly incorporates spatial dispersion of refractoriness. The goal of this approach is not to develop a model that closely represents the detailed electrophysiology of ventricular conduction, but rather to develop the simplest model that retains key features of the problem. The pioneering work of Moe et al.[101] represented an initial effort in this direction. We have developed realistic ECG simulation results with our simple ventricular model whose elements retained only dynamical parameters such as action potential duration, autochron and state values, which will be described in the following sections.

3.2 Ventricular Model

We present a simple finite-element model of ventricular conduction in which a cylindrical shell model represents a first order approximation to ventricular geometry as depicted in **Figure 3.1.** The cylindrical ventricle with a diameter of 4.5 cm and length of 9 cm was placed inside a spherical torso centered at the origin, [0,0,0], with radius 12.5 cm. In our analysis, 45 square elements were generated along the length of the cylinder and 71 square elements were generated along the circumference of the cylinder, thus totaling 3,195 elements. The linear dimension of the square elements in our model is 2 mm.

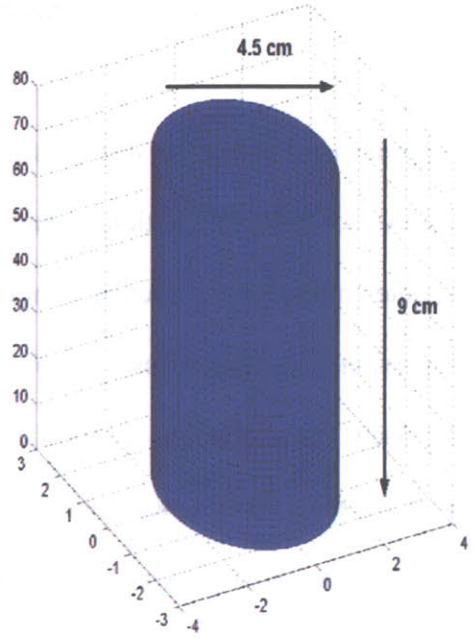

Figure 3.1: Cylindrical finite element model for ventricular conduction with a radius of 4.5 cm and length of 9 cm. The linear dimension of the square elements in our model is 2 mm.

3.3 Model Time Factor

Due to the fact that our model is discrete, it was important to keep track of most parameters in terms of machine time units (MTU). To later interpret our ECG's in terms of physical time units, we computed the following time scale value, $t = T_{QRS}/(m+n/2)$, where m is the number of rows and n is the number of columns in the ventricular model and T_{QRS} is the duration of a normal sinus rhythm QRS complex in the absence of the fast Purkinje system, which is the case in our model. The $m+n/2$ factor represents the total number of elements that will depolarize the ventricle during one cardiac cycle. The resultant time scale value with T_{QRS} = 140 msec, m = *45*,

and $n = 71$ is 1.7391 msec for each element. Therefore, each element will contain an underlying physical time scale value of $t = 1.7391$ msec.

3.4 Scar Tissue Description

To simulate Ventricular Tachycardia (VT) due to a localized reentrant loop, we superimposed on a small region of the ventricular surface a three-layer scar tissue area. The inner and outer layer consisted of permanently refractory elements. Note that one element in the outer loop remained excitable and constituted our exit site. The middle layer consisted of excitable elements, which when appropriately activated, allowed the depolarization wave to propagate such that reentry developed. In order to simulate this reentry circuit, the initial state of one element was depolarizing while its neighbor was initially refractory, thus allowing a unidirectional movement of the depolarization wavefront. These three levels of elements representing the scar area are shown in **Figure 3.2**.

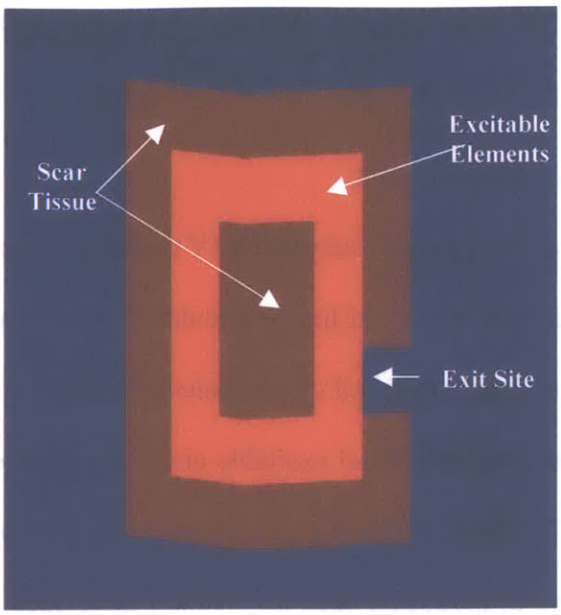

Figure 3.2: Scar tissue in the ventricular model consisting of an inner and outer layer of permanently refractory elements and a middle layer of excitable elements. An element in the outer layer of permanently refractory elements remains excitable and is considered the exit site.

One potential problem with a fixed geometry inner loop of excitable elements is that it limits the number of evenly spaced elements for varying the speed of the depolarizing wave. To address this problem, we evaluated the excitable loop in 1-D as shown in **Figure 3.3**. With this feature, although the perimeter of excitable elements remains constant, the number of excitable elements inside the scar tissue could vary, thus altering the conduction velocity and allowing for the generation of various rates of VT.

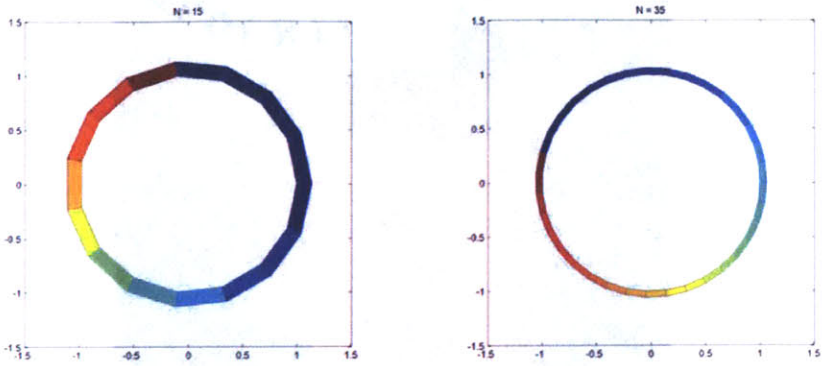

Figure 3.3: Examples of 1-D loops of excitable elements within the scar tissue with 15 elements (left) and 35 elements (right).

Our model topology consisted of 2-D ventricular elements and 1-D excitable loop elements. In order to link the two dimensions, in addition to considering the elements adjacent to the exit site in the 2-D ventricular elements as neighbors, we will consider all the elements in the 1-D loop that are in contact with the exit site as additional nearest neighbors. Note that although the elements in the 1-D excitable loop are smaller in size in the model, they do retain the same time scale value as the larger 2-D elements. This feature allows us to slow down conduction in the 1-D loop relative to the conduction velocity in the 2-D ventricular elements. **Figure 3.4** illustrates 3 elements in the 1-D excitable loop in contact with the exit site. Therefore, when the exit site is excited, we will have to consider the state of the 1-D loop elements and thus create the dynamical transition from 2-D to 1-D excitation rules.

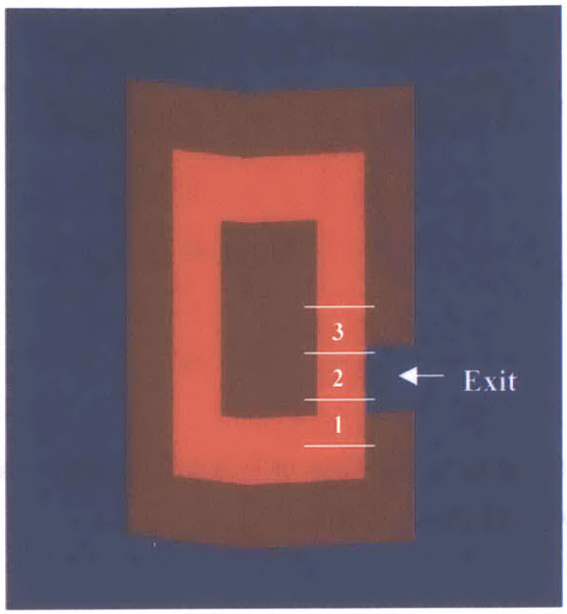

Figure 3.4: Scar tissue indicating the three nearest neighbors of the exit site element inside the 1-D excitable loop.

3.5 Excitation and Conduction Rules

A finite state cellular automata model was used to develop a set of excitation rules for the spread of depolarization. A cellular automata is an element, usually part of a collection of many similar elements, which is always in one of a specified number of internal states and whose internal state evolves in time according to a specified set of state transition rules.[102] The two most commonly used lattices for two-dimensional finite element simulations contain square or hexagonal elements as shown in **Figure 3.5**. The square lattice is probably most often used because the locations of the centers of each lattice element form an orthogonal coordinate system and is how we define the eight nearest neighbors to an element.

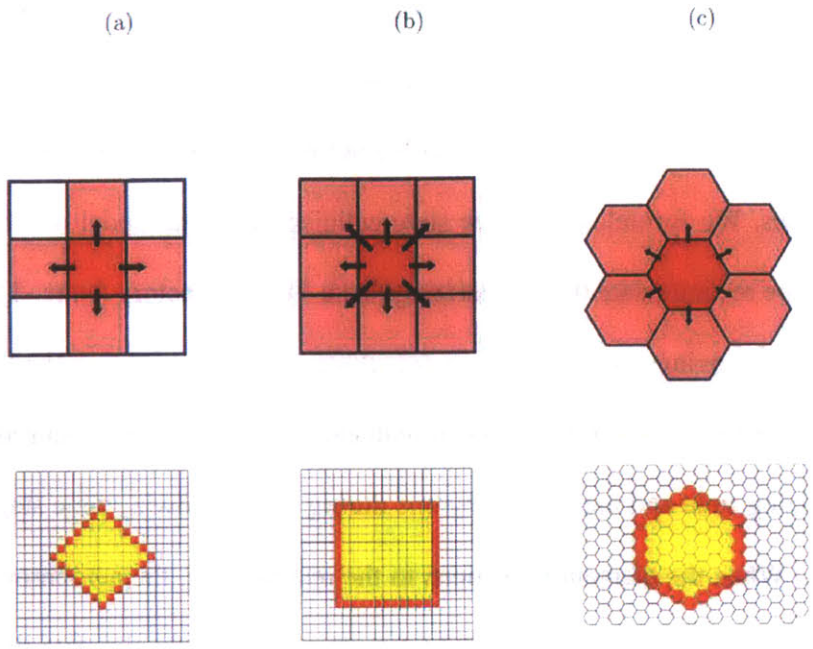

Figure 3.5: Two simple Bravais lattices (top) and the waves resulting from nearest neighbor interactions on those lattices (bottom). Figures (a) and (b) show square lattices (each lattice point is at the center of an individual square). In Figure (a), the "nearest neighbors" are taken to be those lattice elements that share an edge with the central element. In Figure (b), "nearest neighbors" are taken to be any element in contact with the central element. Each system produces square waves from a single element, though the waves are oriented at 45° to each other. Figure (c) shows a hexagonal lattice. Although this eliminates the problem of choosing between two different types of neighbors, the resulting wave still has the (discrete) symmetry of the lattice.[103]

We used our knowledge of the cardiac cell's action potential and refractory period to model the spread of depolarization in our ventricular model. The action potential corresponds to the time evolution of the trans-membrane potential of a cardiac cell following excitation. The refractory period, roughly corresponding to the width of the action potential as shown in **Figure 3.6**, indicates the period following excitation of a myocardial cell during which time the cell cannot be re-excited.

A finite state cellular automata model was used to simulate ventricular electrical activity. A cellular automata model is composed of elements that are always in one of a specified number of internal states, and evolve in time according to a specified set of state transition rules. We formulated a three state cellular automata model in which the heart tissue could be resting (state 0), depolarizing (state 1), or refractory (state -1). In addition to each element having a state value, an autochron value representing the time since the cell was last activated was also associated with each element. The autochron is set to 1 in the depolarizing state and increments by one during each following time step as shown in **Figure 3.6**. When the element transitions to the resting state, the autochron continues to increase until the element is re-activated (state 1). To properly simulate the physiology, the refractory period of each element was dynamically adjusted based on the value of the preceding diastolic interval.

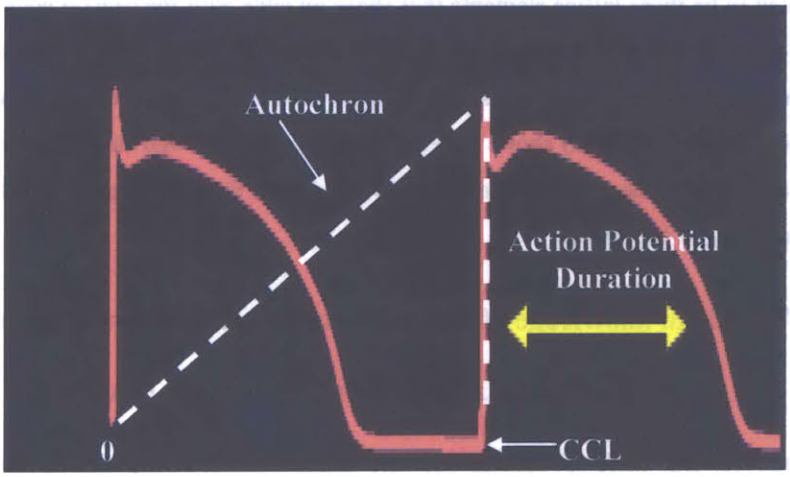

Figure 3.6: Illustration of the cardiac cell's action potential indicating the behavior of the autochron and depiction of the action potential duration for one cardiac cycle length (CCL).[104]

Now I will provide an example of our excitation and state transition rules for our ventricular model in **Figure 3.7**. If an element at time n is resting and at least one of its neighbors is depolarizing (state 1), at time $n+1$ that element will go into the depolarizing state and the neighbor becomes refractory, as shown in the top figure. In our model, an element stays in the depolarizing state (state 1) for only one time step. If an element is resting at time n and none of the neighbors is depolarizing, it remains at rest at time $n+1$. If an element is in the refractory state at time n and the autochron is less than the value of the refractory period, the state remains refractory while if the autochron is greater than or equal to the refractory period, the state becomes resting at time $n+1$ as shown in the lower figures. A refractory element is not affected by the state of its neighbors.

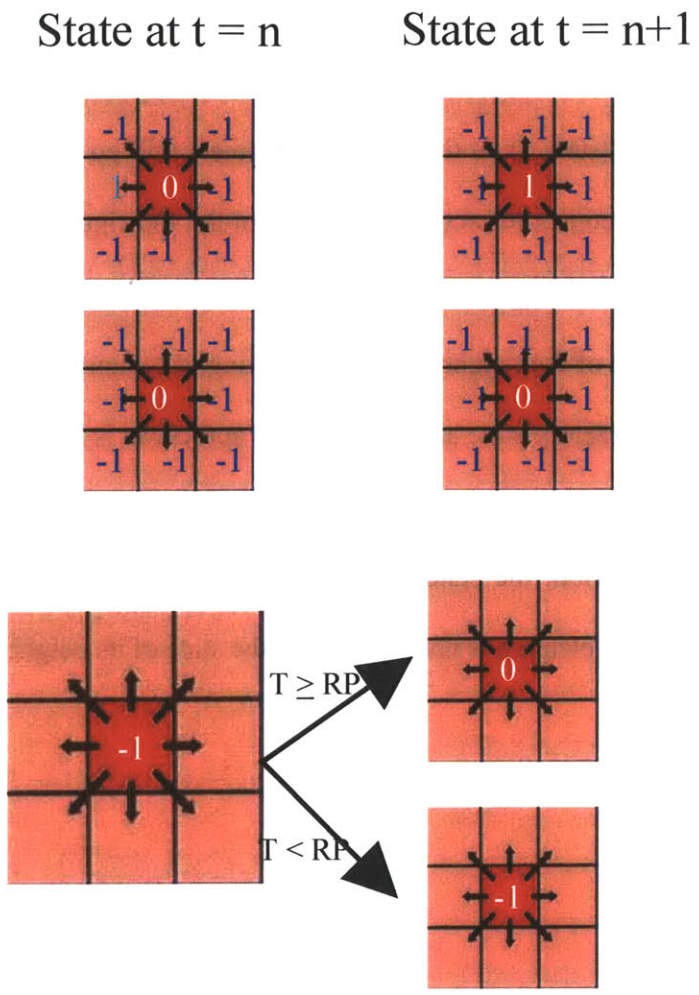

Figure 3.7: Example of Excitation and State Transition Rules. If an element at time *n* is resting and at least one of its neighbors is depolarizing (state 1), at time *n+1* that element will go into the depolarizing state and the neighbor becomes refractory, as shown in the top figure with the depolarizing state indicated by a green 1. If an element is resting at time *n* and none of the neighbors is depolarizing, it remains at rest at time *n+1*. If an element is in the refractory state at time *n* and the autochron is less than the value of the refractory period, the state remains refractory while if the autochron is greater than or equal to the refractory period, the state becomes resting at time *n+1* as shown in the lower figure.

The spread of depolarization was controlled by a simple conduction scheme in which an element depolarized if two conditions were met: (i) the time since the last depolarization exceeded the elements refractory period and (ii) one or more of its eight

nearest neighbors depolarized during the previous time iteration. We excited one element at the edge of the cylinder at regular intervals to activate the model and represent AV-node, or atrio-ventricular, pacing. We then allowed an appropriately timed pacing stimulus to initialize the reentry in the 1-D loop, located at the center of the cylinder, which eventually overrides the AV-node pacing as shown in **Figure 3.8**. Views of the cylinder in 2-D and 3-D are shown in the simulation result.

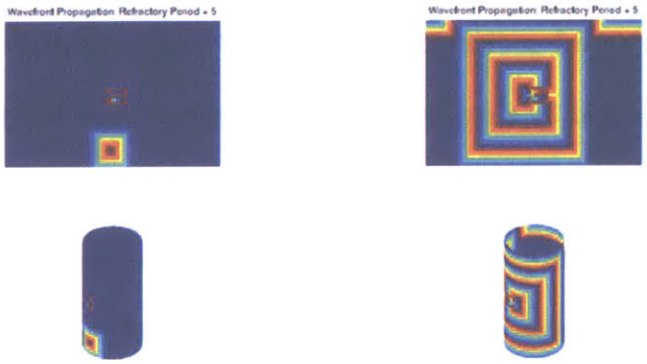

Figure 3.8: 2-D and corresponding 3-D views of the cylindrical finite element model activated at a single element at regular intervals along with activation of the scar tissue area. We used a refractory period of 5 for each of the elements and a pacing period of 35 in this simulation. Note after some time, as shown in the second figure, the pacing at the scar tissue site overrides the AV-node pacing.

3.6 Action Potential Simulation

We used our knowledge of the cardiac cell's action potential and refractory period to model the spread of depolarization in our ventricular model. The action potential corresponds to the time evolution of the trans-membrane potential of a cardiac cell

following excitation. The refractory period, roughly corresponding to the width of the action potential, indicates the period following excitation of a myocardial cell during which time the cell cannot be re-excited. In order to generate a realistic action potential for each element, we turned to the Beeler-Reuter Model.[105] Beeler and Reuter described a mathematical model of membrane action potentials of mammalian ventricular myocardial fibers. Four individual components of ionic current were formulated mathematically in terms of Hodgkin-Huxley type equations.

The model incorporated two voltage- and time-dependent inward currents, the excitatory inward sodium current, i_{Na}, and a secondary or slow inward current, i_s, primarily carried by calcium ions. A time-independent outward potassium current, i_{K1}, exhibiting inward-going rectification, and a voltage- and time-dependent outward current, i_{x1}, primarily carried by potassium ions, are further elements of the model. The i_{Na} is primarily responsible for the rapid upstroke of the action potential, while the other current components determine the configuration of the plateau of the action potential and the repolarization phase. The relative importance of inactivation of i_s and of activation of i_{x1} for termination of the plateau was evaluated by the model.

The primary model is a single space-clamped patch of membrane, which consists of a membrane capacity with four parallel current paths. Eight parameters must be integrated to produce a solution to this model. These are the membrane potential across the capacity, the intracellular calcium ion concentration as it is affected by i_s, and six activation or inactivation parameters for the various conductances. At each step in time, the Runge-Kutta-Merson integration algorithm establishes a set of values for the variables being integrated (initial conditions for the step) and provides these values:

membrane potential, $[Ca]_i$, and six conductance parameters; to a subprogram which computes the derivative for each integrated variable. During this process, the individual ionic currents are determined and summed along with any 'externally applied' current to arrive at the charging current for the membrane capacity, which then determines the derivative of the membrane potential. The complete set of equations and constants that define the model are given in Beeler and Reuter's paper.[105]

Upon solving the system of eight first-order simultaneous nonlinear differential equations, we retrieved the voltage values for the action potential duration. Because the cardiac cycle length (*CCL*) exceeds the value of the action potential duration (*APD*), we used the cubic spline to append the action potential with zeros for all values of the autochron (T) where $T > APD$ and $T < CCL$. The simulation result of an *APD* of 300 msec and cardiac *CCL* of 560 msec is shown in **Figure 3.9**.

We later scaled the ordinate axis containing the potential values to the range [0,1], which will be useful later when generating dipole moments between depolarizing and repolarizing elements for use in the body surface potential field generation. We assign a refractory period to each element and compute the individual elements' potentials by scaling the duration of the simulated action potential with the current refractory period of the element. This dynamic adjustment of the refractory period will be discussed in the following section.

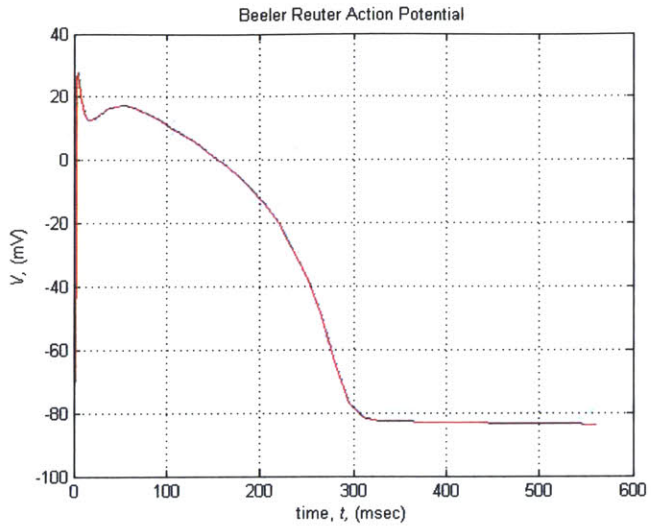

Figure 3.9: Simulated action potential using the Beeler Reuter model.

3.7 Dynamic Refractory Period

Cohen and Smith[100] showed that the spatial dispersion of refractoriness was a sufficient condition to initiate reentrant arrhythmias. Spatial variation in refractory times leads to the appearance of islands of refractory tissues during the repolarization process. A new wave of depolarization impinging on these islands of refractory tissue will fractionate. Such fractionation of the depolarization wavefront can lead to eddies and reentry. While Smith and Cohen's model involved an evolution of islands of refractory tissue, our model's dynamic refractory periods were generated in real-time based on the restitution property of cardiac tissue.

3.7.1 Restitution

The heart rhythm originates from the sino-atrial node, which generates a sequence of electrical stimuli that can trigger excitation waves propagating through the heart.

These excitation or Action Potential (AP) waves in turn generate electric potentials on the body surface that can be recorded as a local electrocardiogram (ECG). The shape of the *AP* wave in cardiac tissue, characterized primarily by the Action Potential Duration (or *APD*, denoted T_{AP}), depends on the time the tissue has rested since the end of the previous excitation (Diastolic Interval, or DI, denoted by T_{DI}).[106] The dependence $T_{AP} = f(T_{DI})$ is usually referred to as a restitution function or curve.[107] In reality, we always deal with sequences of stimuli, so one must write $T_{AP}^{n+1} = f(T_{DI}^{n})$, where the superscript indicates the cardiac cycle number. Within the nth cardiac cycle, the APD and DI are related by the relation $T_n = T_{AP}^{n} + T_{DI}^{n}$, where T_n is the nth cardiac cycle length (CCL). The above two relations combined can be expressed as $T_{DI}^{n+1} = T_{n+1} - f(T_{DI}^{n})$.

In reality, due to heart rate variability the sino-atrial node generates a stimulus sequence that is not strictly periodic, so the aforementioned conditions are not strictly applicable. The input stimulus sequence can be viewed as a signal from a "noisy metronome" with a random spacing T_n between the n^{th} and $(n-1)^{th}$ stimuli. In the corresponding iterative map, $T_{DI}^{n+1} = T_{n+1} - f(T_{DI}^{n})$, the first term on the right hand side represents a random component while the second term is deterministic.

For an illustration of restitution and how the preceding diastolic interval affects the next action potential duration, observe **Figure 3.10** in which a series of stimuli has been applied to the cardiac tissue.

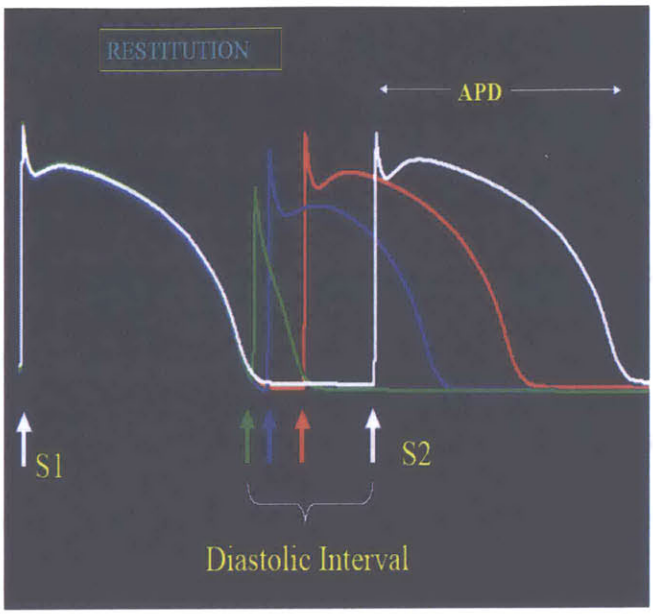

Figure 3.10: Restitution illustration where a stimulus, *S1*, has been applied to the cardiac tissue. A series of stimuli, *S2*, follow to illustrate how the length of the preceding diastolic interval affects the length of the next action potential duration, *APD*. The first *S2* (green) is applied to the heart tissue just before the resting phase, thus resulting in a short *APD*. In the next case, *S2* (blue) is applied when the heart tissue has been resting for a very short time resulting in an APD that is not quite as long as the *APD* resulting from *S1*. Eventually when the stimulus is applied after a sufficient length of time during the *DI*, *S2* (white), the *APD* has the same duration as the *APD* resulting from *S1*.[104]

3.7.2 Dynamic Action Potential: *Elharrar and Surawicz Method*

Elharrar and Surawicz studied the steady state behavior of the *APD* by applying a sequence of long, periodic conditioning pulses to the cardiac tissue.[107] Upon creation of this artificial electrical history, a random test pulse was applied and considered the current *APD*. The steady-state *CCL-APD* relationship is described by the equation

$$\overline{APD} = \frac{\overline{CCL}}{a\overline{CCL} + b}, a = 3.03s^{-1}, b = 1.08 \tag{3.1}$$

where *CCL* is the cycle length in msec. The constants *a* and *b* were determined by linear regression analysis between *1/z* and *1/APD*. A general equation describing restitution curves is given by,

$$APD_t = APD_{\max} \cdot g(z) \cdot \left\{ 1 - A_1 e^{-\frac{DI_t}{T_1}} - A_2 e^{-\frac{DI_t}{T_2}} \right\} \tag{3.2}$$

where *t* is the test *DI* (DI_t); *T* and *A* are the time constant and the intercept, respectively, of the fast (T_1, A_1) and slow (T_2, A_2) exponential components; APD_{max} is the limit value of *APD* at infinitely long cycle length, which is given by *1/a*; *g(z)* is a function of the *CCL* having a value of 1 for infinitely long *CCL* and <1 for shorter *CCL*.

Although this method proved useful in a controlled experimental setting, the need for a dynamic model that would suffice when individual elements contain a different history was apparent. The Elharrar and Surawicz study did not explain the property that different heart tissue regions will naturally have a different history. Therefore, Yuri Chernyak of the Cohen Lab extended their equations to include the dynamic evolution of refractory periods by generating an arbitrary pacing sequence for each element in the model.

3.7.3 Dynamic Action Potential: *Chernyak Method*

Yuri Chernyak of the Cohen Lab introduced a simpler notation for the dynamic evolution of refractory periods. In our analysis *T* will represent *CCL*, *t* will represent *DI*, and τ will represent *APD* so,

$$T = t + \tau . \tag{3.3}$$

The steady state quantities will be marked by 'bar' as follows,

$$\bar{T} = \bar{t} + \bar{\tau}. \tag{3.4}$$

As aforementioned, according to Elharrar and Surawicz, the steady state quantities are simply related by the relation

$$\bar{\tau} = \phi(\bar{T}) \equiv \frac{\bar{T}}{a\bar{T} + b}, \quad a = 3.03 s^{-1}, \; b = 1.08. \tag{3.5}$$

According to Equation (3.4) and Equation (3.5), any two of the quantities $\bar{t}, \bar{\tau}, \bar{T}$ can be readily expressed via the third. For example,

$$\bar{T} = \frac{b\bar{\tau}}{1 - a\bar{\tau}}, \tag{3.6}$$

and

$$\bar{t} = \bar{\tau} - \frac{\left(b - 1 + a\bar{\tau}\right)}{1 - a\bar{\tau}}. \tag{3.7}$$

The dependence on the preceding *DI*, *t*, is presented as a separate factor,

$$\rho(t) = 1 - Ae^{-\alpha t} - Be^{-\beta t} \tag{3.8}$$

where the amplitudes are $A = 0.375$ and $B = 0.125$, and the time constants $T_\alpha \equiv 1/\alpha =$ 0.093s and $T_\beta \equiv 1/\beta =$ 1.455s so that the first exponent describes much faster kinetics than the second one. The Elharrar and Surawicz description of the test *APD*, τ, following a test *DI*, *t*, which was preceded by a long periodic conditioning pacing sequence with the period $\bar{T}$, can be written as follows,

$$\tau = \phi(\bar{T}) \frac{\rho(t)}{\rho(\bar{t})} \equiv \frac{\bar{T}}{a\bar{T} + b} \cdot \frac{1 - Ae^{-\alpha t} - Be^{-\beta t}}{1 - Ae^{-\alpha \bar{t}} - Be^{-\beta \bar{t}}} \tag{3.9}$$

In this equation, $\bar{t}$ is the steady state *DI*. Interestingly, Elharrar & Surawicz used only the numerical value of $\bar{t}$ and specified neither the variable nor the expression through which $\bar{t}$ was actually computed. The dependent variable can be either $\bar{T}, \bar{\tau}$ or $\bar{t}$ since they all can be expressed via Equation (3.4) and Equation (3.5).

The problem now was to extend Equation (3.9) to the arbitrary pacing sequence. With this goal in the forefront, we observed that the first factor in Equation (3.9) is simply the steady-state, or conditioning *APD* so Equation (3.9) becomes

$$\tau = \bar{\tau}\frac{\rho(t)}{\rho(\bar{t})}. \tag{3.10}$$

Guided by the idea that most of the information is contained in the preceding *APD*, $\bar{\tau}$, we shall express $\bar{t}$ through $\bar{\tau}$ via Equation (3.7) and obtain

$$\tau = \bar{\tau}\frac{\rho(t)}{\rho\left(\bar{\tau}\frac{\left(b-1+a\bar{\tau}\right)}{1-a\bar{\tau}}\right)}. \tag{3.11}$$

Equation (3.11) is equivalent to Equation (3.9), but makes use of two variables $\bar{\tau}$ and t instead of three variables, $\bar{T}$, $\bar{t}$, and t. Now it can be readily rewritten to incorporate an arbitrary pacing sequence because the quantities marked by the 'bar' also correspond to the CCL that immediately precedes the test stimulus, so we can write

$$\tau_{n+1} = \tau_n\frac{\rho(t_{n+1})}{\rho\left(\tau_n\frac{b-1+a\tau_n}{1-a\tau_n}\right)}. \tag{3.12}$$

This equation represents the final form of the recurrent relation, thus describing the current *APD* as if the preceding *APD* was the last in the steady sequence, $\tau_n = \bar{\tau}$. It was essential that the steady-state information was incorporated in the denominator of Equation (3.12), which will be equal to the numerator only if steady-state is reached. Equation (3.12) indeed possesses the correct asymptotic properties, that is, τ_{n+1} tends to the correct new steady-state value determined by the new steady *CCL* (pacing rate). Notice if one used the equation,

$$\tau_{n+1} = \tau_n \frac{\rho(t_{n+1})}{\rho(t_n)}, \tag{3.13}$$

which includes the actual value of t_n, the sequence would not have correct asymptotic properties. Similar to Equation (3.12), all such extensions must have the steady-state parameters, a and b, incorporated in the denominator in such a way that the algebraic fraction tends to unity when the equilibrium is reached.

3.8 Dipole Moment Generation

In the following sections, we will develop an analysis for computing the dipole moment and direction between the individual model elements. The dipole moment will be proportional to the potential differences between neighboring elements and the dipole direction will be based on simple unit vector analysis.

3.8.1 Dipole Magnitude

In order to compute the body surface potentials, we first assigned dipole moments to each of the interfaces between the elements in our finite element model as illustrated in **Figure 3.11**. From electrophysiologic theory, we know that each dipole moment is proportional to the difference in the transmembrane potential values between

corresponding adjacent elements. We can determine the dipole moment by utilizing the equation,

$$\vec{p}_{ij} \propto \left(V_i - V_j\right) \cdot \vec{u}_{ij} \tag{3.14}$$

where $\left(V_i - V_j\right)$ is the potential difference between the element and its neighbor and $\vec{u}_{ij}$ is the unit vector for an arbitrarily shaped ventricle. For simplification purposes, we will generate dipoles between four nearest neighbors, eliminating the diagonal elements; these are *left (L)*, *right (R)*, *up (U)*, and *down (D)* elements. To prevent double counting, we only need to consider all of the *up* and *right* elements of an element because one element's *right*, is another's *left* and one element's *up* is another's *down*.

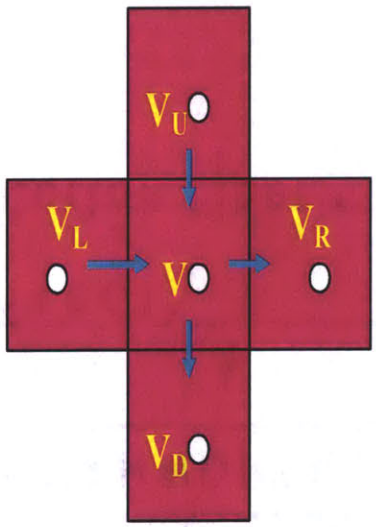

Figure 3.11: Potential values of element V and its four nearest neighbors with the corresponding dipoles of varying magnitudes between adjacent elements (blue arrows).

3.8.2 Dipole Direction

The use of a general unit vector simplifies computation of the projection of the 1-D loop elements onto the spherical torso surface. With the use of this unit vector, any general ventricle shape would produce a correct projection onto the spherical torso surface, where the ECG is computed from the surface leads. An illustration of the unit vectors is shown in **Figure 3.12**. The vector, $\vec{r}_B$, is the boundary vector which is an average of the two neighboring position vectors and is shown in Equation (3.15). The difference between the boundary and the dipole location vectors, $\vec{r}_1 - \vec{r}_B$ and $\vec{r}_2 - \vec{r}_B$, followed by one vector shift to the left and another vector shift to the right and normalization by the magnitude, produces the unit vectors, u_L and u_R as shown in Equations (3.16) and (3.17) .

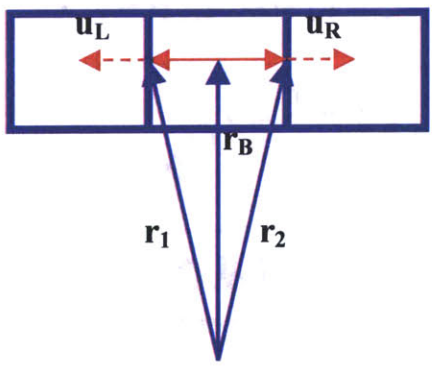

Figure 3.12: Generalized unit vectors (u) associated with the dipole moment between adjacent left (L) and right (R) elements. The vector, $\vec{r}_B$, is the boundary vector which is an average of the two neighboring position vectors, $\vec{r}_1$ and $\vec{r}_2$.

$$\vec{r}_B = \frac{(\vec{r}_1 + \vec{r}_2)}{2} \tag{3.15}$$

$$\vec{u}_L = \frac{\vec{r}_1 - \vec{r}_B - \frac{scy}{2}}{|\vec{r}_1 - \vec{r}_B|} \tag{3.16}$$

$$\vec{u}_R = \frac{\vec{r}_2 - \vec{r}_B - \frac{scy}{2}}{|r_2 - \vec{r}_B|} \tag{3.17}$$

3.9 Potential Field Generation

Upon calculating the dipole moments, we then calculated the body surface potentials on the surface of a sphere of radius 12.5 cm enclosing the ventricular model that would be generated by this distributed collection of dipoles. We computed the potentials for each of the N elements, resulting in elements of dimension [4 x # electrodes x N] as shown in Equation (3.18). We then summed over the four potentials at each element resulting in a matrix of dimension [1 x # electrodes x N]. Finally, we summed over the number of elements in the model, N, to generate the potentials for the number of electrode leads in the model.

$$\phi_i = \left[\phi_{up}, \phi_{down}, \phi_{left}, \phi_{right}\right] \tag{3.18}$$

$$\phi_{2i} = \sum_{i=1}^{4} \phi_i \tag{3.19}$$

$$\phi_{3i} = \sum_{i=1}^{N} \phi_{2i} \tag{3.20}$$

3.10 Electrophysiologic Simulation Results

We placed 60 electrodes on our torso model ran the simulation for 3000 machine time units (MTU) to produce the lead results shown in **Figure 3.13A-D**. We then took the difference between two leads that were far from one another to generate the normal sinus rhythm. We did not activate the reentry circuit to produce normal sinus rhythm. The cardiac cycle length was taken to be 750 msec and the pacing stimulus was applied every 433rd time step (corresponding to CCL / t). A simulation of a normal ECG with a rate of 80 bpm (60,000 msec/minute * 1/1750 msec) is shown in **Figure 3.14**.

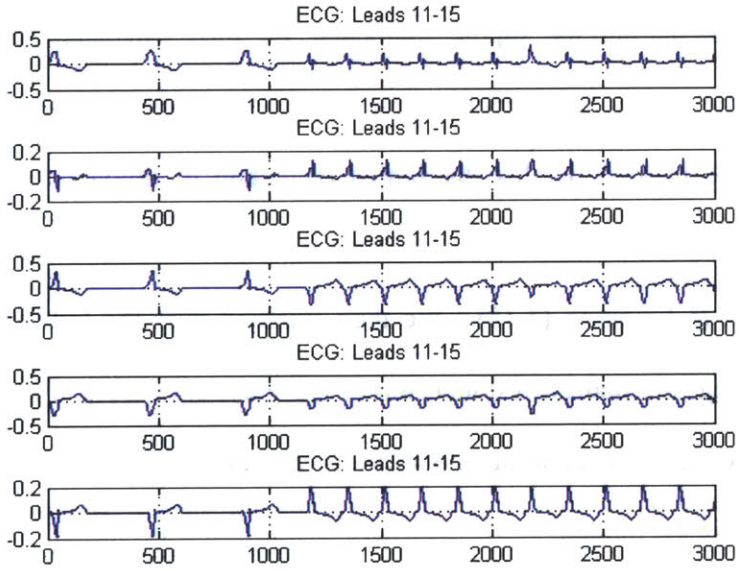

A

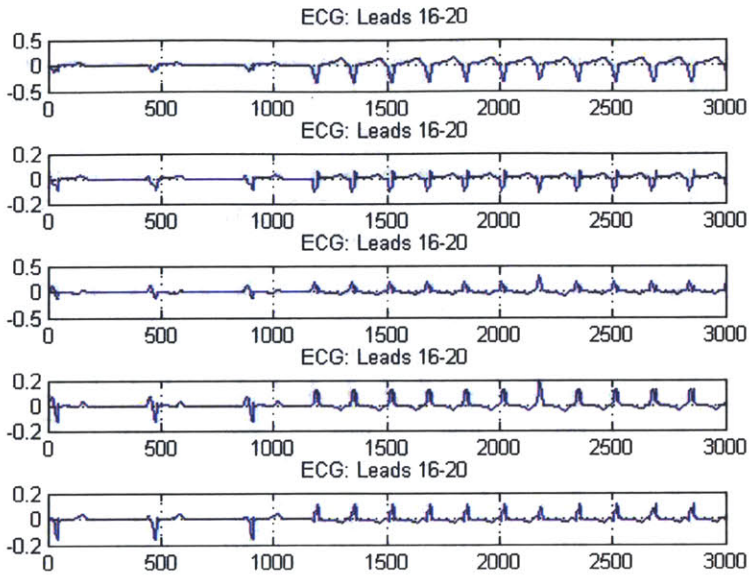
ECG: Leads 16-20
ECG: Leads 16-20
ECG: Leads 16-20
ECG: Leads 16-20
ECG: Leads 16-20
0.5
0
-0.5
0.2
0
-0.2
0
500
1000
1500
2000
2500
3000

B

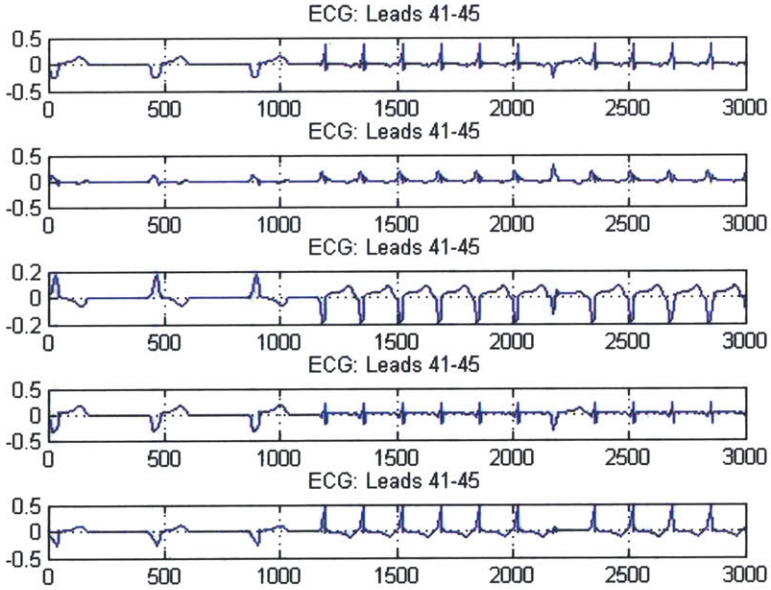
ECG: Leads 41-45
ECG: Leads 41-45
ECG: Leads 41-45
ECG: Leads 41-45
ECG: Leads 41-45
0.5
0
-0.5
0.2
0
-0.2
0
500
1000
1500
2000
2500
3000

C

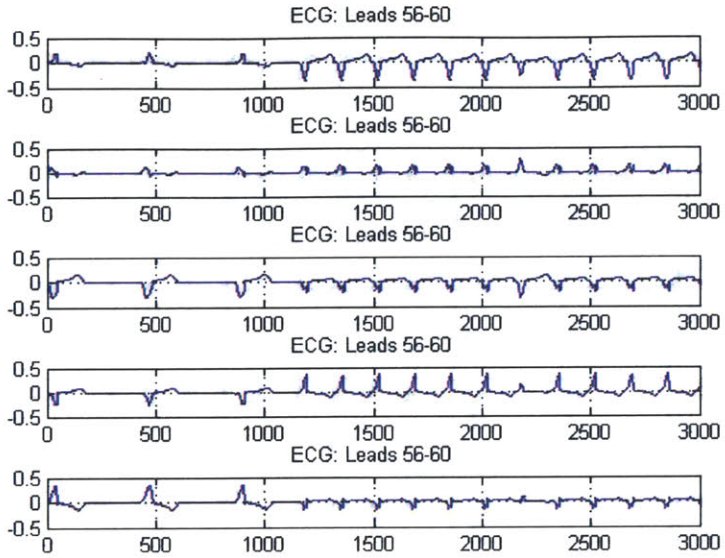

D

Figure 3.13A-D: ECG lead results for leads number 11-15 (A), 16-20 (B), 41-45 (C), and 56-60 (D) extracted from the total 60 electrodes electrocardiograms.

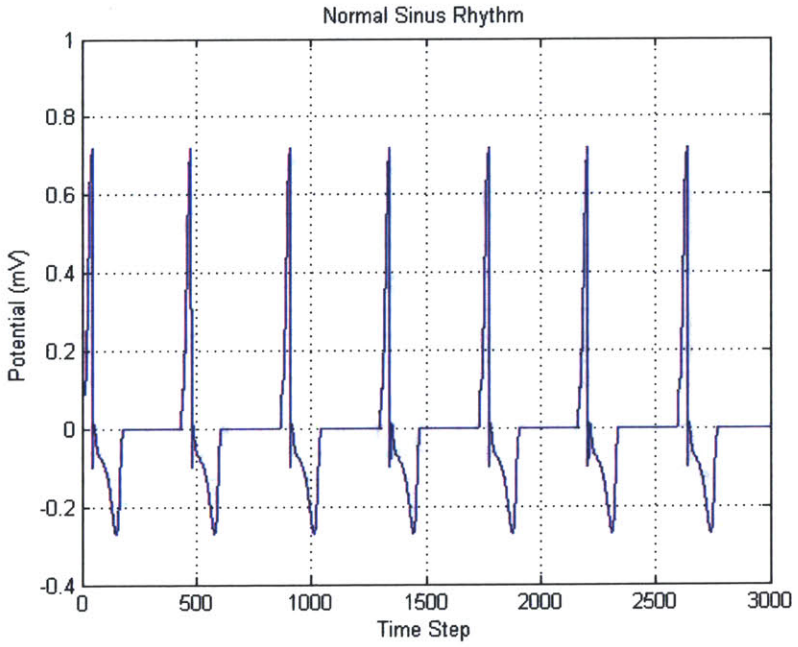

Figure 3.14: Simulation of normal heart rhythm with a rate 80 bpm.

In order to produce Ventricular Tachycardia, we activated the reentry circuit, which contained one activated element in direct proximity to a refractory element at the 1001^{st} MTU, meaning the atrio-ventricular node had been initially activated 1000 MTUs ago. Activating one element while making the preceding element refractory forces the propagation to proceed in one direction instead of two directions, which would lead to the waves canceling one another.

To illustrate the wave propagation, we present the following hypothetical example representing the 3-D and 2-D views of the cylinder in which the refractory period is 5 MTUs. The corresponding voltage values in the range [0:1] were plotted, which corresponded to autochron matrix values in the range [0:5]. A color gradient showing the minimum voltage value of 0 (dark blue) to a maximum value of 1 (dark red) was displayed as shown in **Figure 3.15**. Note that both the reentry circuit and the atrio-ventricular node have been excited and after some time, the VT overrides the atrio-ventricular pacing as shown in **Figure 3.16**.

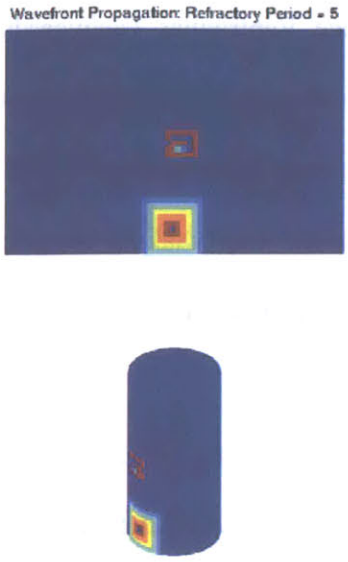

Figure 3.15: Cylindrical model activated at the atrio-ventricular node and the pacing site in the scar tissue loop. We used a τ value of 5 and T value of 35 in our simulations.

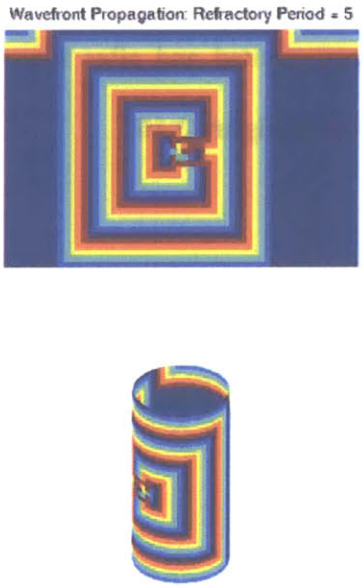

Figure 3.16: Wavefront propagation as pacing within scar tissue overrides the atrio-ventricular pacing rate.

We considered two rates of VT, both slow and fast. Slow VT refers to VT in which a period of cardiac electrical inactivity exists before the next beat of VT, ensuring that the dipole exiting the reentry circuit is highly localized. However, in fast VT this period of inactivity is nonexistent and thus the cardiac electrical activity from preceding beats may interfere causing less localization of the dipole as it exits the reentry circuit. Examples of slow (CCL = 500 msec) and fast VT (CCL = 300 msec) are shown in **Figure 3.17A-B**. Upon converting machine time units to physical time units, we were able to compute a slow VT rate of 120 beats per minute and a fast VT rate of 200 beats per minute.

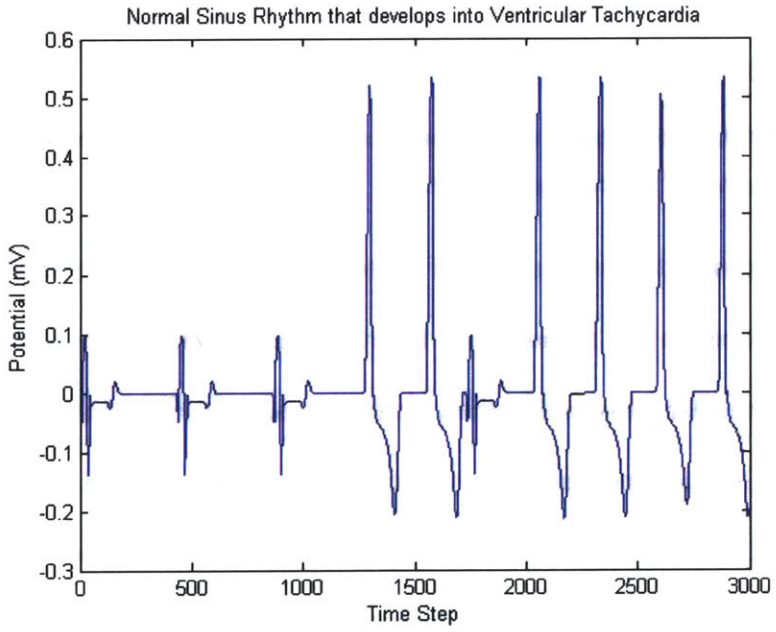

A

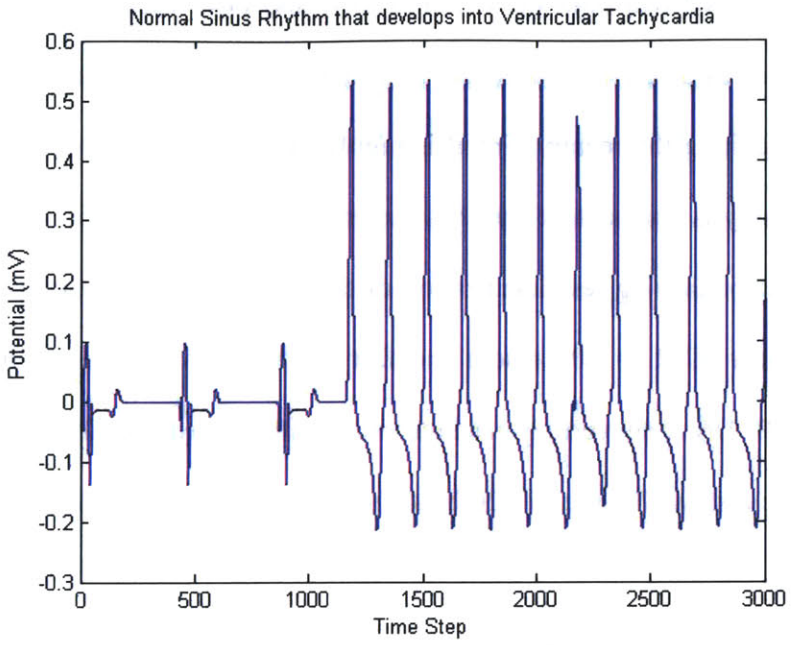

B

Figure 3.17A-B: Simulation of (A) slow VT with a rate of 120 beats per minute and (B) fast VT with a rate of 200 beats per minute.

We can conclude that a number of ventricular arrhythmias can be generated from the model developed in this section. The following parameters can be altered to produce a variety of ventricular arrhythmias: the ventricular pacing rate, P, the ventricular cardiac cycle length, CCL, the time instant for scar tissue pacing, k_{inr}, and the scar tissue cardiac cycle length, CCL_r. One must be careful to time the [P and CCL] and [k_{inr} and CCL_r] such that the wavefront from the atrio-ventricular pacing does not extinguish the wavefront exiting the scar tissue. In addition, the size and location of the scar with respect to the size of the ventricle should be taken into account. The key to successful ventricular arrhythmia simulation is that scar tissue pacing overrides the atrio-ventricular pacing.

3.11 Discussion of Electrophysiologic Simulation Results

We were successful in our task to develop a simple and deterministic model for a straightforward approach to electrocardiogram (ECG) simulations. In our approach we utilized well-established research findings on cardiac tissue behavior. The normal cardiac depolarization of the ventricle was observed through use of excitation rules we developed based on knowledge regarding refractoriness of tissue and the spread of the depolarization wavefront in the ventricle. In addition, superposition of permanently refractory elements on the ventricular surface to represent scar tissue was sufficient for providing the proper interruption of normal electrical conduction so that VT could develop.

The restitution property of cardiac tissue was used to support the development of dynamic refractory periods for each element as the electrical activity propagated through the model. The dipole moment magnitude was computed by taking the difference between neighboring elements' intrinsic potential values, which was derived from an action potential model assigned to each element, and proved to be simple and accurate. The incorporation of a loop of 1-D elements on a 2-D cylindrical surface was ingenious for a simple approach to producing varying rates of VT. We proved that such an approach provides unlimited access to any particular rate of VT without the restrictions encountered with a fixed geometry model.

The leads from the 60 electrodes, which were randomly placed on the torso, displayed a variety of ECG morphologies as would be expected in a clinical setting. In addition, computing the difference between surface electrodes that were far apart, closely resembled the normal ECG as seen in a clinical setting when electrodes are placed at a

distance in which the polarities will differ. This model provides a concise and efficient methodology for ECG generation, which can simply be utilized in a number of applications.

Chapter 4

Brute Force Inverse Algorithm

4.1 Introduction

This chapter focuses on the development of an algorithm that improves the safety, efficiency, and cost-effectiveness of the medical procedure of radio-frequency ablation (RFA) for Ventricular Tachycardia (VT) patients. Currently, physicians use an approach to RFA, which is just short of a trial-and-error technique in localizing the exit site of a VT reentry circuit. Upon applying a stimulus to the ventricle in hopes of inducing VT, radio-frequency energy is applied when the physician observes VT on the ECG monitor, thus indicating the exit site has been localized with the ablation catheter. Drawbacks of this trial-and-error approach to RFA include that the method is time-consuming due to difficulty in determining the exit site, which leads to high costs for hospitals and patients. Most importantly, patients who cannot tolerate multiple inductions of the arrhythmia due to hemodynamic instability are not candidates for this minimally invasive RFA procedure due to their low tolerance for induction and maintenance of VT.

Therefore, the need was evident for an accurate and efficient RFA technology that would address both the difficulty in defining reentry circuits that cause VT and intolerance to maintenance, or multiple inductions, of VT.[108,109] We addressed the limitations of the current RFA procedure by developing a Brute Force Inverse Algorithm (BFIA) that utilized the forward and inverse problems of cardiology. For each point in

time, the BFIA estimates the location and moment of a single equivalent moving dipole resulting in a trajectory in space of cardiac dipoles. A brute force algorithm in the true sense of the meaning implies the search space consists of a very large number of possible fine resolution solutions. Our algorithm is actually *intelligent* because the solution space resolution is reduced in iterative steps versus performing a one step search. The BFIA should increase the accuracy and speed in targeting the ablation site during the RFA procedure.

Previously, Armoundas developed a simplex inverse algorithm applicable to RFA, which accurately localized the VT exit site when applied to simulated data. However, problems of entrapment in local minima and poor dipole trajectory visualization were apparent when the algorithm was applied to clinical data.[110,111] Thus, the simplex method is not optimal for RFA due to these limitations. Alternatively, the BFIA's exhaustive analysis of the solution space prevents entrapment in local minima and has proven to produce the anticipated clear dipole trajectories when applied to clinical data.[111]

4.2 Forward Problem

The forward problem is one in which the body surface potentials are determined given knowledge of the heart generator. The electrical activity of the myocardial cells causes current to flow within the body and establish potential differences on the surface of the skin. The graphical recording of these body surface potentials as a function of time produces the electrocardiogram (ECG).[112] For the forward problem formulation, we considered two models in our analysis: the unbounded infinite homogeneous conductor (unbounded model) and the bounded spherical model (bounded model).

4.2.1 Unbounded Model

In the unbounded model, which is the field of the free dipole containing no boundary effects, the electrode locations, dipole locations, dipole moments and tissue conductivity are used to determine the theoretical potential values, ϕ, as shown in Equation (4.1). As **Figure 4.1** illustrates, the electrode locations are $\vec{r} = (x, y, z)$, the dipole locations are represented by $\vec{r}' = (x', y', z')$, the dipole moments are $\vec{p} = (p_x, p_y, p_z)$, and the conductivity of the human torso, g, is 1.2 x 10^{-3} Siemens/cm. The BFIA dipole solutions are computed using the unbounded model equation.

$$\phi = \frac{\vec{p} \cdot (\vec{r} - \vec{r}')}{4\pi g |\vec{r} - \vec{r}'|^3} \tag{4.1}$$

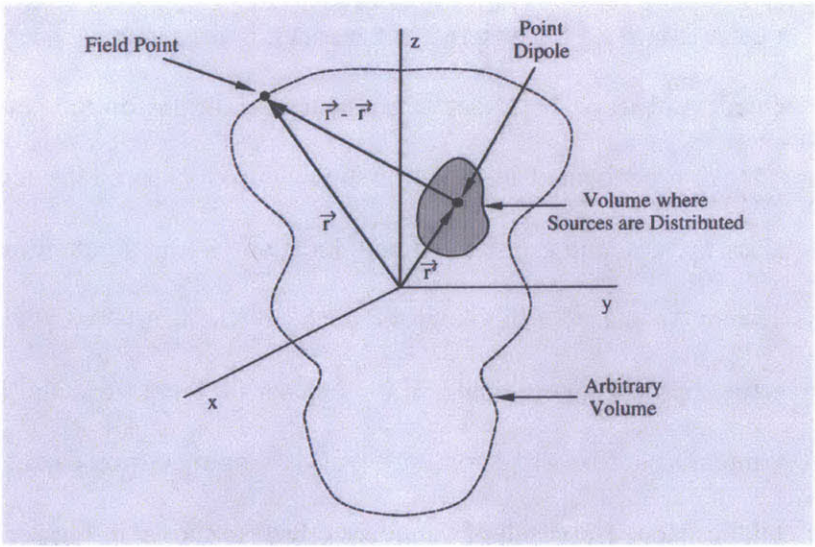

Figure 4.1: The potential field in an infinite homogeneous medium; r is the vector from the origin to the field point and r' is the vector from origin to the point dipole.[110]

4.2.2 Bounded Model

Unlike the unbounded model, the bounded model equation for the potential field considers boundary effects of the torso. Experiments have shown that boundary effects,

inhomogeneities in tissue conductivity, imprecise knowledge of the electrode locations, and non-detailed torso geometry may lead to systematic error. Systematic error exists in our inverse algorithm analysis when utilizing the bounded model in the forward problem because the BFIA utilizes the unbounded model. The potentials in the bounded model's forward problem were computed using the following equation,[113]

$$\phi = \frac{p_z}{4\pi g f R^2}\left[\frac{1-f^2}{\left(1+f^2-2f\mu\right)^{3/2}}-1\right] + \frac{p_x\cos\psi + p_y\sin\psi}{4\pi g f R^2\sin\theta}\left[\frac{3f-3f^2\mu+f^3-\mu}{\left(1+f^2-2f\mu\right)^{3/2}}+\mu\right] \tag{4.2}$$

where $\mu = \cos\theta$ and θ and ψ are the azimuth and latitude angles, respectively. A dipole is placed along the z-axis at z = fR, where f is a constant in the range between 0 and 1.

We decided to observe the affect of boundary conditions on the performance of our algorithm. We thus conducted a simulation in which we observed the accuracy in the difference between the true and estimated dipole locations as the dipole moved closer to the torso boundary. We placed a dipole at the center of the heart (0,0,5) cm. We then chose to move the dipole's x-coordinate in increments of 1 cm, thus the (D_x, D_y, D_z) coordinates became (D_x, 0, 5) cm and consisted of D_x changing during each trial while D_y and D_z remained the same. The result of boundary effects is shown in **Figure 4.2**.

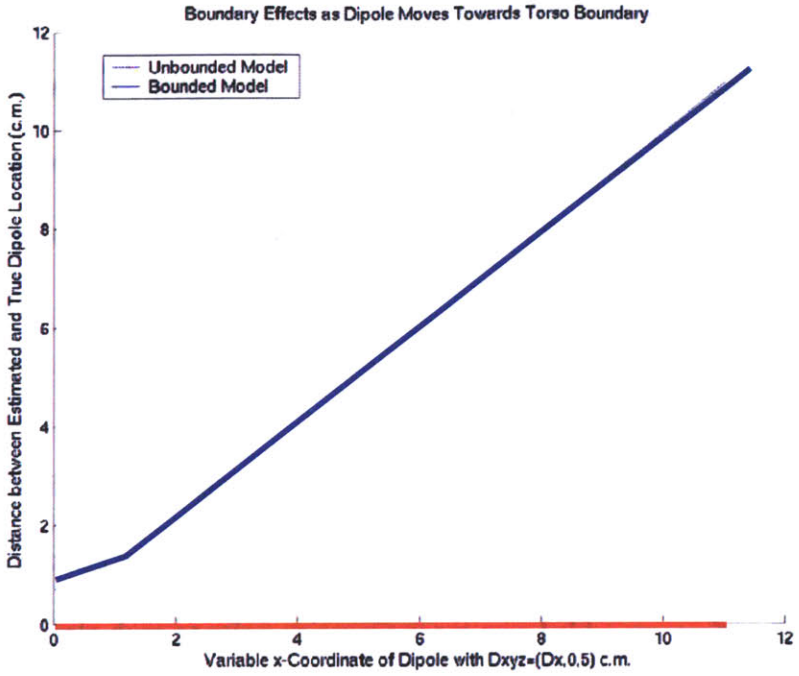

Figure 4.2: Effect of boundary conditions as the cardiac dipole moves from the center of the torso towards the surface. The Unbounded Model results are shown in red and the Bounded Model results are shown in blue.

We did not expect boundary effects to be an issue when using the unbounded model in the simulation and is validated by our results. However, when the bounded model was used in the forward problem, we saw a decrease in accuracy of the algorithm results as the dipole moved closer to the torso boundary. Our belief that boundary effects decrease the accuracy of the Brute Force Inverse Algorithm is confirmed in **Figure 4.2**.

4.2.3 Electrode Distribution

Prior work by Armoundas suggested that a uniform distribution of the electrodes in the forward problem is the best option in reducing the spatial error for localization of the dipole source.[110] A grid on a spherical surface is generated with a uniform distribution of randomly spaced nodes, which corresponds to an electrode site $\mathbf{r}^i$ and is

represented by its spherical coordinates, (r^i, θ^i, ϕ^i). Since the differential solid angle is given by solid angle geometry, $d\Omega = sin(\theta)d\theta d\phi = d(cos(\theta))d\phi$, we randomize $cos\theta$ in the interval [-1,1] to obtain the θ angle and randomized ϕ in the interval $[0,2\pi]$. The radius of the spherical torso is R = 12.5 cm and the potentials are computed using either the unbounded or bounded models.

4.2.4 Noise

We utilized the facts that clinical electrocardiograms have a signal on the order of a few mV and are usually corrupted by μV level noise to model the effect of noise on the electrodes. Therefore, we added zero mean Gaussian noise to each electrode signal with a standard deviation, σ, ranging from low, moderate, high to very high levels (1μV, 10μV, 100μV, and 1 mV, respectively). The resulting measured potential, ϕ_m^i, represented the potential at a specific site *i*. We observed a total of 60 electrode sites.

4.3 Inverse Problem

The inverse problem consists of determining the dipole parameters, $\vec{p}$ and $\vec{r}'$, from the potential field on the body surface. In general, it is not possible to uniquely specify the characteristics of a current generator from the potentials alone. In other words, the 3-D distribution of the cardiac electrical sources cannot be constructed from the 2-D distribution of ECG signals on the body surface. However, if we can assume the cardiac electrical dipole sources are localized, the relationship between the cardiac generator and body surface potentials may be studied and solved. Such an assumption can be made through use of the Single Equivalent Moving Dipole (SEMD) model.

4.4 Single Equivalent Moving Dipole

The Single Equivalent Moving Dipole (SEMD) model is the simplest mathematical model for relating the cardiac generator to the body surface potentials and represents the torso as a linear, isotropic, homogeneous, spherical conductor. The SEMD model represents the heart as a single bioelectrical dipole source that moves in space during the cardiac cycle and changes in magnitude and direction. When applying the SEMD model, the assumption is that the heart is suspended in a homogeneous isotropic conducting medium and observed from a distance large compared to its size. We can thus assume that all of the individual current dipoles of the cardiac generator originate at the same point in space.

The total cardiac electrical activity is represented by a single equivalent dipole source whose magnitude and direction is the vector summation of all the individual dipole sources.[1] As cardiac depolarization spreads, the cardiac dipole changes in magnitude and direction as a function of time. In our analysis, we apply the SEMD model, but ignore tissue inhomogeneities in electrical conductivity and boundary effects.

The SEMD model does have some limitations. The first limitation is that the SEMD represents the heart as a single bioelectrical source while the heart really consists of distributed dipole sources. The SEMD is strictly valid when the electrical activity is highly localized, such as when it initially emerges from the VT site of origin. This happens to be the only point in time of interest to us. The second limitation is that we ignore tissue inhomogeneities and boundary effects that are present in the heart. The effect of these inhomogeneities and boundary effects is that they distort the image

location of the SEMD. But when the SEMDs of the VT exit site and catheter tip are brought together, their distortions should be equivalent and thus cancel.

4.5 The 3 plus 3 Parameter Optimization Method

In the 3 plus 3 parameter optimization method, originally developed by Antonis Armoundas,[110] we determine the 3 dipole moment components analytically and the 3 dipole location components numerically. One can conclude from observing the unbounded and bounded model equations, Equation (4.1) and Equation (4.2), that the potential field, ϕ, is linear in dipole moment components, p, and the minimization in terms of the moments can be performed analytically so they become known, explicit functions of the dipole location and measured body surface potentials.

Now that the moment is expressed through dipole location, it only remains to minimize the objective function, χ^2, in terms of the three location components, which is achieved numerically using the Brute Force Inverse Algorithm (BFIA). The equation for the objective function is as follows,

$$\chi^2 = \sum_{i=1}^{I} \left(\frac{\phi_m^i - \phi_e^i}{\sigma_i} \right)^2, \tag{4.3}$$

where ϕ_e^i is the theoretical potential field computed by the BFIA and ϕ_m^i are the measured body surface potentials computed by the forward problem. It is apparent that in the presence of noise in the electrodes, χ^2 will never be zero. However, when ϕ_e^i and ϕ_m^i are of the same order as the noise, σ_i, we would expect the signal-to-noise ratio of the χ^2 estimate to approach 1. The system of equations for computing the dipole moment components, p_α for the unbounded model is as follows:

$$\frac{\partial \chi^2}{\partial p_\alpha} = 0 \tag{4.4}$$

and

$$\sum_{i=1}^{I} \frac{\left(\phi^i - \phi_m^i\right)}{\sigma_i^2} \frac{\partial \phi^i}{\partial p_\alpha} = 0 \tag{4.5}$$

which yields,

$$\sum_{i=1}^{I} \frac{1}{\sigma_i^2} \left[\frac{\vec{p} \cdot \left(\vec{r}^{\,i} - \vec{r}\right)}{\left|\vec{r}^{\,i} - \vec{r}\right|^3} - \phi_m^i \right] \frac{r_\alpha^i - r_\alpha}{\left|\vec{r}^{\,i} - \vec{r}\right|^3} = 0, \tag{4.6}$$

where I is the number of electrode positions. Using the following components,

$$\vec{p} \cdot \left(\vec{r}^{\,i} - \vec{r}\right) = \sum_\beta p_\beta \left(r_\beta^i - r_\beta\right), \tag{4.7}$$

we write

$$\sum_\beta p_\beta \left[\sum_{i=1}^{I} \frac{\left(r_\beta^i - r_\beta\right)\left(r_\alpha^i - r_\alpha\right)}{\sigma_i^2 \left|\vec{r}^{\,i} - \vec{r}\right|^6} \right] = \sum_{i=1}^{I} \frac{1}{\sigma_i^2} \phi_m^i \frac{r_\alpha^i - r_\alpha}{\left|\vec{r}^{\,i} - \vec{r}\right|^3}. \tag{4.8}$$

For simplification, let

$$M_{\alpha\beta} = \sum_{i=1}^{I} \frac{1}{\sigma_i^2} \frac{\left(r_\beta^i - r_\beta\right)\left(r_\alpha^i - r_\alpha\right)}{\left|\vec{r}^{\,i} - \vec{r}\right|^6} \tag{4.9}$$

and

$$B_\alpha = \sum_{i=1}^{I} \frac{1}{\sigma_i^2} \phi_m^i \frac{r_\alpha^i - r_\alpha}{\left|\vec{r}^{\,i} - \vec{r}\right|^3}. \tag{4.10}$$

Therefore,

$$\sum_{\beta} M_{\alpha\beta} p_{\beta} = B_{\alpha} , \tag{4.11}$$

$$\vec{p} \cdot M = B , \tag{4.12}$$

and

$$\vec{p} = BM^{-1} . \tag{4.13}$$

4.6 Ablation Site

The SEMD is strictly valid when the electrical activity is highly localized, such as when it initially emerges from the VT site of origin, or the reentry circuit's exit site. This happens to be the only point in time of interest to us. Reentry is the return of the same impulse into a zone of heart muscle that it has recently activated. The substrate for reentry is typically scar tissue left behind from a previous heart attack. The QRS complex is inscribed when the excitation wavefront emerges from the reentry circuit's exit site as shown in **Figure 4.3**.[8] Therefore, if we deliver an impulse to the ablation catheter when it is located at the exit site, the resultant ECG will display VT and thus indicate the ablation site.

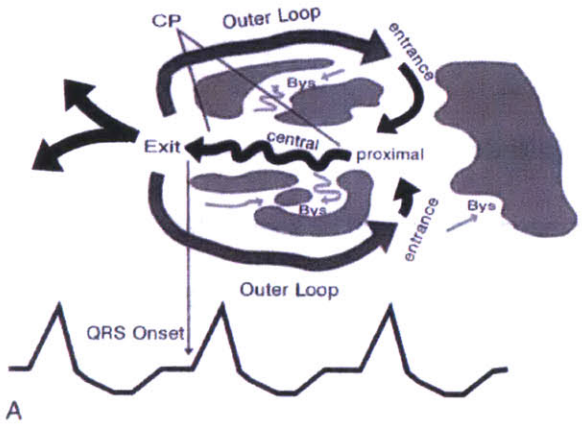

Figure 4.3: A double loop (figure-eight) reentry circuit consisting of a central common pathway (CP) and two outer loops. The grey regions represent scar tissue.[77]

4.7 Exit Site Criteria

The ectopic pacing site in the reentry circuit depolarizes the exit site and propagates to further depolarize the rest of the ventricle. This resulting wave of depolarization produces body surface potentials represented by the electrocardiogram. These potentials are used as input to the Brute Force Inverse Algorithm (BFIA) and for each point in time of the cardiac cycle, a single equivalent dipole is estimated thus producing a trajectory of cardiac dipoles. We can then apply a set of exit site criteria developed by Maya Barley[111] of the Cohen Lab to determine which dipole location in the cardiac dipole trajectory corresponds to the exit site.

We understand that the target site for ablation occurs when the excitation wavefront leaves the reentry circuit from the exit site. The dipole at this exit site is highly localized before spreading to surrounding tissue or continuing in the circuit where the dipole vectors are less localized. Barley[111] analyzed previously acquired clinical data

and developed a preliminary set of criteria to determine the ablation site. These criteria are described below.

4.7.1 Dipole Magnitude

The dipole magnitude should be small when exiting the reentry circuit due to high localization of the depolarization wavefront as it exits the reentry circuit. Therefore, we will focus on dipoles that are small in magnitude to represent possible sites for ablation.

4.7.2 Distance Between Consecutive Dipoles

Barley[111] found that the dipole locations were highly uncorrelated before and during the pacing spike. However, after the initial decline of the ECG signal, the dipoles followed a clear trajectory. At the initial decline point, the dipoles were closely grouped together since the area of activation was minimal and the speed of depolarization slow. This is the region in which the exit site dipole should be found. Therefore, we will compute the distance between consecutive dipoles to locate this dipole cluster of interest. The dipole chosen as the site of ablation should occur soon after the distance between consecutive dipoles reaches a minimum.

4.7.3 χ^2 and RNMSE

The BFIA computed an error value, χ^2, for each dipole solution. The χ^2 is essentially a comparison between the dipole and noise whose values are in the range [0,1], where 1 represents the best localization. If the dipole is highly localized, the measured potentials should be very close to the estimated potentials on the body surface. As the wave becomes more diffuse, the χ^2 exceeds one and becomes futile. Therefore, we can use the fact that the χ^2 does provide useful feedback for a highly localized region,

such as the exit site of the reentry circuit. Barley showed that the maximum χ^2 lies near the peak of the QRS, where the voltages are largest and the wavefront is becoming highly diffuse.[111] She concluded the ablation site dipole should be characterized by a low χ^2 value to ensure that the dipole estimation is good.

The Root Normalized Mean Square Error (RNMSE), shown in Equation (4.14), represents the difference between the estimated and measured electrode potentials due to the Single Equivalent Moving Dipole (SEMD) model parameters. The RNMSE indicates how much potential in the measured signal cannot be attributed to the SEMD.

$$RNMSE = \sqrt{\frac{\sum_{i=1}^{I}\left(V_e^i - V_m^i\right)^2}{\sum_{i=1}^{I}\left(V_m^i\right)^2}} \tag{4.14}$$

In the equation V_e^i is the voltage at the electrode estimated by the forward algorithm, V_m^i is the measured voltage at the same electrode, and I represents the total number of electrodes under observation.

Because the RNMSE is a normalized measure of error, its value should be highest, close to one, if the measured potentials and noise are of the same order. If the RNMSE is close to zero, meaning the signal-to-noise ratio (SNR) is high, it is likely the dipole solution will be found. Barley[111] found high RNMSE values in the low-voltage period before the start of the QRS complex and concluded that a dipole estimate from samples in this region would likely be inaccurate. As the SNR increased with increasing cardiac activity, the dipole estimate initially became more accurate and the RNMSE decreased. However, because the RNMSE is a ratio of error in the absolute value of the estimated and measured voltages, it may decrease even though the SEMD approximation

is less accurate near the peak of the QRS complex where the SNR is highest. Consequently, the dipole chosen as the ablation site should occur soon after the initial peaks in the RNMSE (corresponding to the end of the repolarization phase) although not at an absolute minimum (corresponding to the peak of the QRS complex).

4.8 Brute Force Inverse Algorithm Description

We will begin with a conceptual description of the Brute Force Inverse Algorithm (BFIA). We discretize the spherical torso into a set of cubic elements as shown in **Figure 4.4**. We sequentially place a dipole in the center of each cubic element and assign to it the dipole moments determined analytically by the 3 plus 3 parameter optimization algorithm. We then compute the body surface potentials generated by that dipole and calculate the error, χ^2, when comparing the estimated potentials to the measured body surface potentials. We then select the element that results in the minimum χ^2 and this determines the location and dipole moments of the best dipole solution.

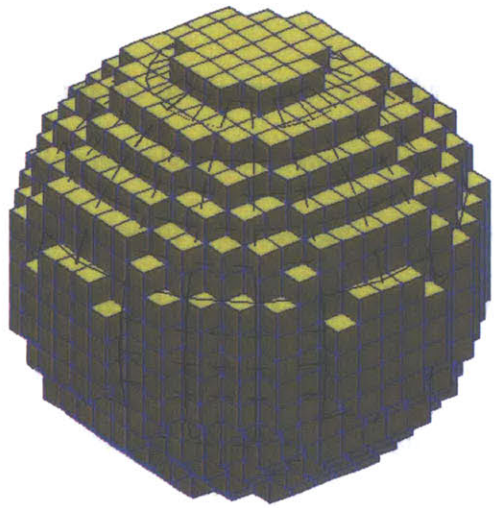

Figure 4.4: Spherical torso of radius 12.5 cm filled with 1.5 cm^3 cubes.

Although we place a dipole in the center of the cubic element, the best dipole location after reducing the cube size might exist in the volume of one of the neighbors. To address this potential discrepancy, upon selecting the cube containing the best dipole solution, we create a cube triple in dimension around the best dipole solution and fill that cube with smaller cubes that are a third of the dimension. Then, we sequentially place a dipole in the center of each cube and begin the process again of computing the dipole moment and location for each cube and selecting the best dipole parameters after evaluating the entire cubic volume.

A flowchart illustrating the explicit steps of the BFIA is provided in **Figure 4.5**. The spherical torso has a radius of 12.5 cm and is filled with cubes on the order of L cm, where L = 1.5 cm.. We sequentially placed a dipole source at the center of each of the cubes. We iteratively reduce the dimensions of the elements until sub-millimeter resolution is attained as follows. We center a (3L x 3L x 3L) cm cube about the best dipole solution and fill that cube with cubes on the order of (L/3 x L/3 x L/3) cm. We repeat the reduction in grid space size until we acquire sub-millimeter resolution, which is the desired accuracy level for clinical purposes.

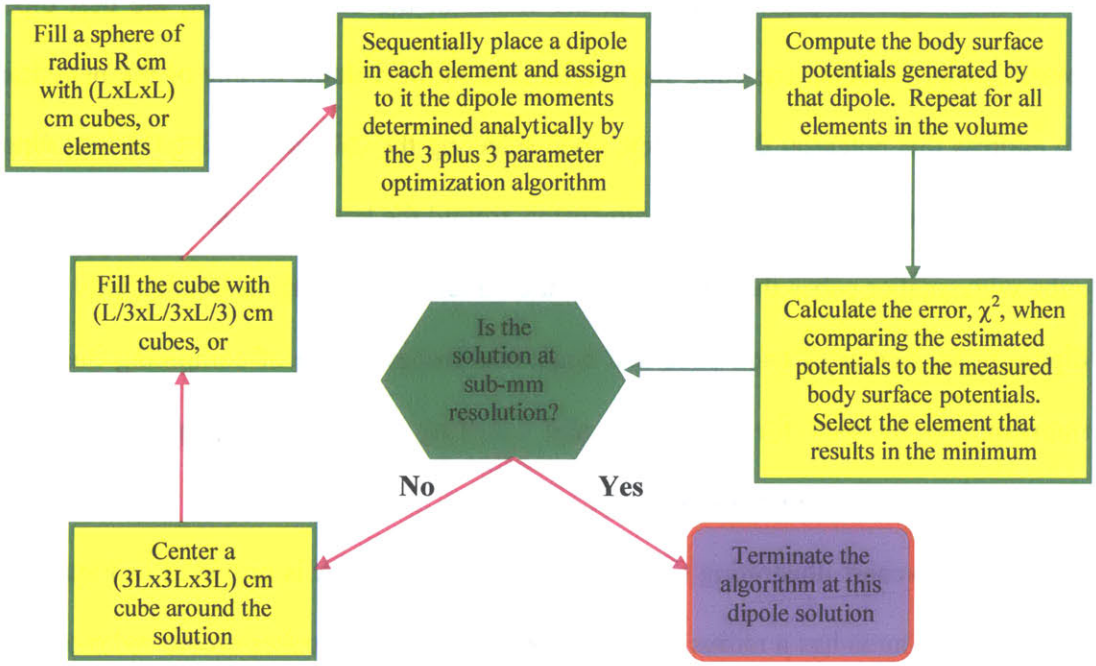

Figure 4.5: Brute Force Inverse Algorithm (BFIA) flow chart outlining the steps by which we use the Brute Force Inverse Algorithm to localize the site for ablation. The spherical torso has a radius of 12.5 cm and is filled with cubes on the order of *L* cm, where *L* = 1.5 cm.. We sequentially placed a dipole source at the center of each of the cubes. We iteratively reduce the dimensions of the elements until sub-millimeter resolution is attained as follows. We center a (3L x 3L x 3L) cm cube about the best dipole solution and fill that cube with cubes on the order of (L/3 x L/3 x L/3) cm. We repeat the reduction in grid space size until we acquire sub-millimeter resolution, which is the desired accuracy level for clinical purposes.

4.9 Research Methods

Upon simulating Ventricular Tachycardia, we will apply the BFIA to a single beat of VT. We will then apply a set of exit site criteria to determine the VT exit site, or VT site of origin. The localized dipole solution from the simulated VT will be called the bioelectrical source solution. Upon randomly placing the catheter in the ventricle, we will deliver an impulse to its tip and apply the BFIA to localize the catheter tip.

Theoretically, when the VT exit site and catheter tip are both localized using the BFIA, any distortions present due to the assumption of tissue homogeneities and lack of boundary conditions will become equivalent and thus cancel. Random error in the localization of the dipole is the only limitation involved in the superposition of the catheter tip and VT exit site.[110]

4.10 Dipole Trajectories

The ability to perform 3-D mapping and view the arrhythmia in real-time would be an improvement to the standard fluoroscopic 2-D imaging. In order to do this, we represented the dipole characteristics by visualizing its trajectory to keep track of dipole movement throughout the heart. In addition, we developed some characteristics for representing the dipole in 3-D. First, we utilized the Brute Force Inverse Algorithm to compute the location and moment parameters of the dipole solution throughout the time of observation. The resulting dipole location was represented by a color filled circle and we represented the dipole orientation by a scaled unit vector with an arrow on the tip. The colors of the dipole parameters were directly related to the time during the dipole movement. Therefore, a dark blue circle in the trajectory corresponded to the first dipole location determined by the brute force inverse algorithm, a dark red circle corresponded to the final solution, and all solutions in between were represented by a color gradient between dark blue and dark red as shown in **Figure 4.8.**

4.11 Slow vs. Fast VT

We considered two rates of VT, both slow and fast. Slow VT refers to VT in which a period of cardiac electrical inactivity exists before the next beat of VT, ensuring that the dipole exiting the reentry circuit is highly localized. However, in fast VT this

period of inactivity is nonexistent and thus the cardiac electrical activity from preceding beats may interfere causing less localization of the dipole as it exits the reentry circuit. Slow VT is less susceptible to error in the SEMD solution because the electrical activity from one beat completely dissipates before the onset of the next beat.

4.12 Brute Force Inverse Algorithm Results

We generated results for both slow VT and fast VT in order to evaluate performance of the Brute Force Inverse Algorithm (BFIA). In slow VT, there is an absence of remote electrical activity in the ventricle at the time that the new wave of depolarization emerges from the exit site. This absence of remote electrical activity at the time the electrical activity emerges from the exit site allows the BFIA to localize the exit site without additional distortion. However, in fast VT, remote electrical activity in the ventricle, resulting from previous beats of VT, is present at the time a new wave of depolarization emerges from the exit site. This presence of remote ventricular electrical activity at the time that the new wave of depolarization emerges from the exit site will contribute to the body surface potentials and thus distort the location of the exit site as calculated by the BFIA.

We tested the BFIA's performance using both the unbounded model, which considers the torso as an infinite homogeneous volume conductor. In the bounded model, we assume the torso is a spherical homogeneous conductor immersed in a volume insulator. Note that we only obtained an undistorted solution for the localized exit site in the case of slow VT using the Unbounded Model.

4.12.1 Unbounded Model Results: Slow VT

The measured potentials from a single cardiac cycle length of slow VT were provided as input to the BFIA as shown in **Figure 4.6**. We then applied the exit site criteria for dipole localization to indicate the time instance during the VT cycle length when the exit site is expected to occur as shown in **Figure 4.7**. Due to the existence of the isoelectric period before the onset of the QRS complex in slow VT, localization of the dipole at the exit site should be straightforward. As Barley predicted, the dipole magnitude is small when exiting the reentry circuit, the exit site occurs soon after the distance between consecutive dipoles reached a minimum, the exit occurred at a at a low χ^2 value, and the exit occurred soon after the initial peaks in the RNMSE although not at an absolute minimum.

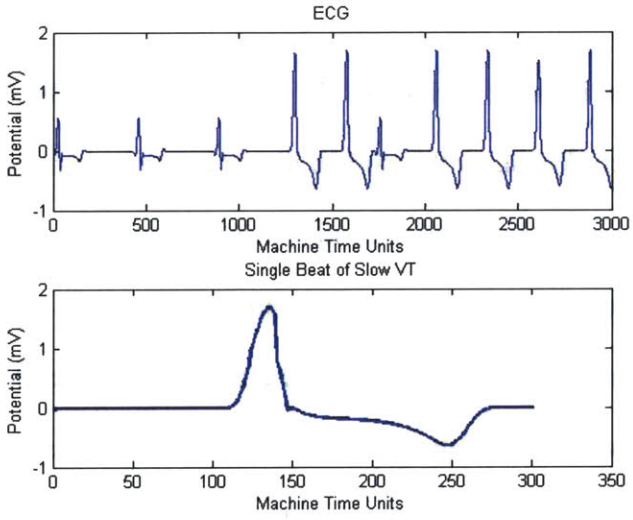

Figure 4.6: Simulation of normal cardiac rhythm, which deteriorates into a slow rate of Ventricular Tachycardia (120 beats per minute) using the Unbounded Model. The bottom figure shows a single beat of the slow Ventricular Tachycardia. Note the isoelectric period that exists before the onset of the QRS complex.

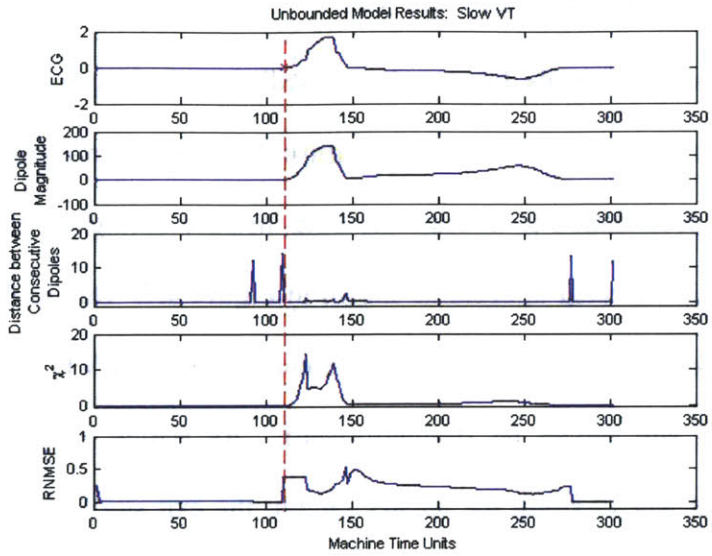

Figure 4.7: The electrocardiogram of slow Ventricular Tachycardia using the Unbounded Model and the exit site criteria (dipole magnitude, distance between consecutive dipoles, χ^2, and Root Normalized Mean Square Error). The red line indicates the time instance corresponding to the occurrence of the exit site.

For each time instance during the VT cycle length, the BFIA computes a dipole location and moment. We show the cardiac dipole location trajectory for one VT cycle length of slow VT using the unbounded model in **Figure 4.8**. In all of the following dipole trajectory results, the yellow patch represents the exit site on the ventricular surface and the number in black represents the time instance in the VT cardiac cycle length at which the exit site is determined. We expect the dipole trajectory to contain a dipole location estimate close to the physical location of the exit site when applying the unbounded model in the forward problem due to the lack of systematic error because the BFIA also uses the unbounded model equation to estimate the body surface potentials. We also did not expect the lack of boundary conditions to affect our results when using the unbounded model. In fact, of all the four cases analyzed in the following sections, the

BFIA determined an undistorted exit site only when applying the unbounded model to slow VT.

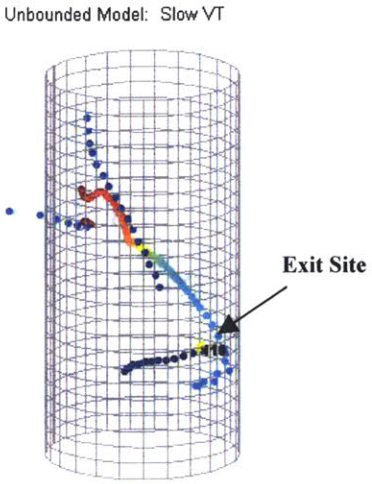

Figure 4.8: Dipole location trajectory for Unbounded Model of Slow VT. The color gradient from dark blue to dark red represents the initial (blue) localized dipole from the VT Cycle Length (VTCL) to the last (red) localized cardiac dipole in the VTCL under evaluation. The yellow patch represents the physical location of the exit site and the number represents the cardiac dipole location in the range [1:VTCL] that corresponds to the estimated time instance of the exit site.

4.12.2 Unbounded Model: Fast VT

Fast VT presents a more challenging environment for the BFIA to work accurately and effectively. During fast VT, the resting period between beats is nonexistent as shown in **Figure 4.9**. Interference from the electrical activity of consecutive VT beats causes distortion and thus difficulty for the BFIA to accurately localize the exit site. We applied the exit site criteria to determine the time instant in the cardiac cycle when the exit site is localized by the BFIA as shown in **Figure 4.10**. As

Barley predicted, the dipole magnitude is small when exiting the reentry circuit, the exit site occurs soon after the distance between consecutive dipoles reached a minimum, the exit occurred at a at a low χ^2 value, and the exit occurred soon after the initial peaks in the RNMSE although not at an absolute minimum.

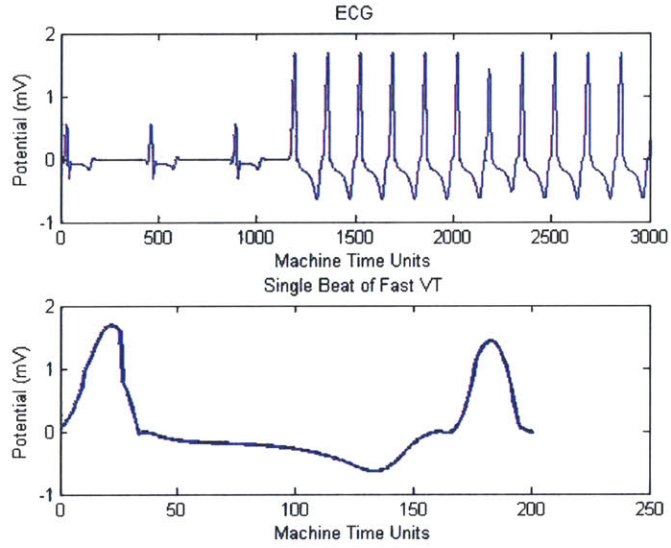

Figure 4.9: Simulation of normal cardiac rhythm, which deteriorates into a fast rate of Ventricular Tachycardia (200 beats per minute) using the Unbounded Model. The bottom figure shows a single beat of the fast Ventricular Tachycardia. Note the lack of an isoelectric period that precedes the onset of the QRS complex.

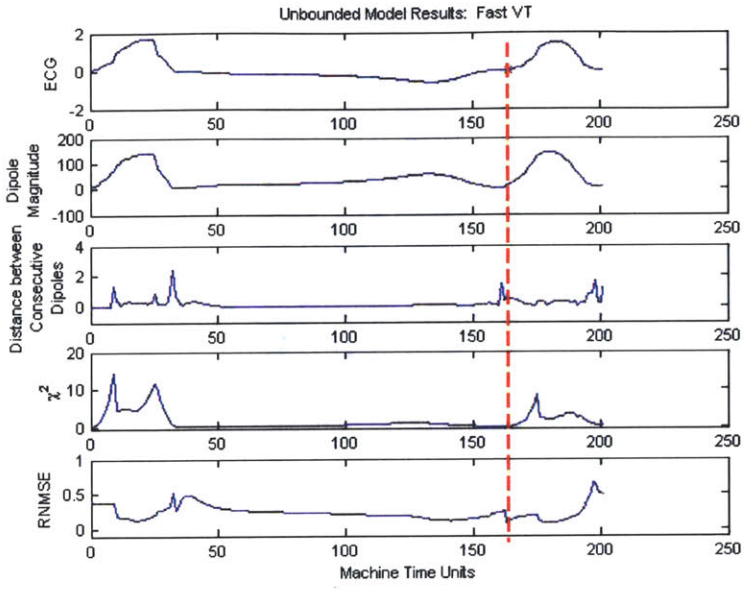

Figure 4.10: The electrocardiogram of fast Ventricular Tachycardia using the Unbounded Model and the exit site criteria (dipole magnitude, distance between consecutive dipoles, χ^2, and Root Normalized Mean Square Error). The red line indicates the time instance corresponding to the occurrence of the exit site.

The BFIA's dipole location trajectory for fast VT using the unbounded model is shown in **Figure 4.11**. We did not expect the dipole trajectory to contain a dipole location estimate close to the physical location of the exit site in the case of fast VT due to distortion caused by interference from the electrical activity of consecutive VT beats. This interference in the case of fast VT prevents the BFIA from accurately localizing the exit site as indicated by lack of correlation between the numbered dipole location in **Figure 4.11** and the physical location of the exit site.

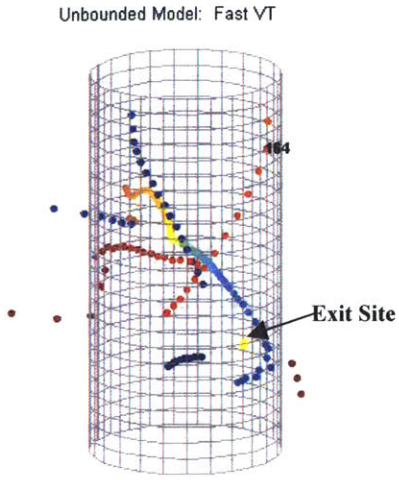

Figure 4.11: Dipole location trajectory for Unbounded Model of Fast VT. The color gradient from dark blue to dark red represents the initial (blue) localized dipole from the VT Cycle Length (VTCL) to the last (red) localized cardiac dipole in the VTCL under evaluation. The yellow patch represents the physical location of the exit site and the number represents the cardiac dipole location in the range [1:VTCL] that corresponds to the estimated time instance of the exit site.

4.12.3 Bounded Model: Slow VT

When the bounded model is applied in the forward problem to compute the measured body surface potentials, we expect a discrepancy in the BFIA's cardiac dipole estimate because the inverse algorithm uses the unbounded model to estimate the body surface potentials. The simulation result of slow VT using the bounded model is shown in **Figure 4.12**. The exit site criteria provided an estimate of the instance during the VT cycle length when the exit site should be localized is shown in **Figure 4.13**.

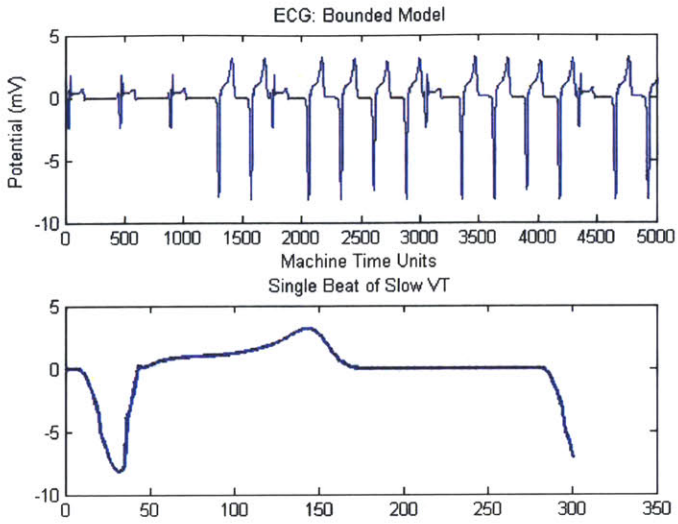

Figure 4.12: Simulation of normal cardiac rhythm, which deteriorates into a slow rate of Ventricular Tachycardia (120 beats per minute) using the Bounded Model. The bottom figure shows a single beat of the slow Ventricular Tachycardia. Note the presence of an isoelectric period that precedes the onset of the QRS complex.

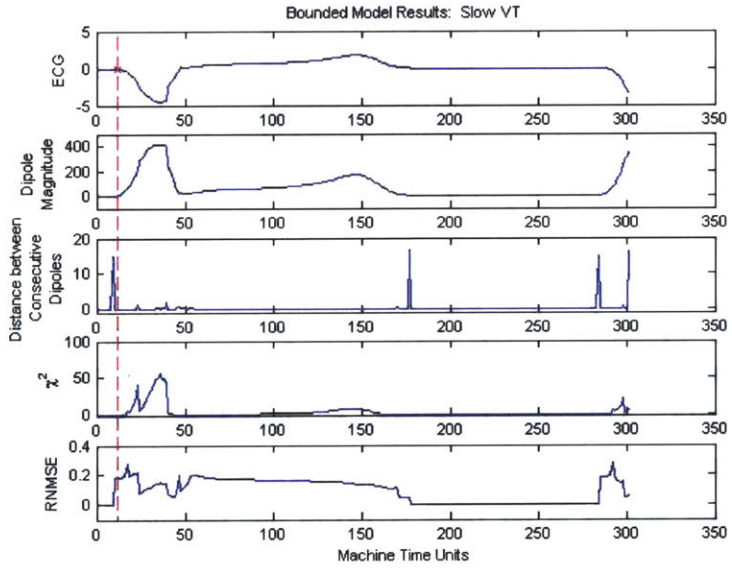

Figure 4.13: The electrocardiogram of fast Ventricular Tachycardia using the bounded model and the exit site criteria (dipole magnitude, distance between consecutive dipoles, χ^2, and Root Normalized Mean Square Error). The red line indicates the time instance corresponding to the occurrence of the exit site.

We expect the exit site criteria to determine a dipole location estimate from the cardiac dipole trajectory that is far away from the physical location of the exit site when applying the bounded model in the forward problem. The resulting systematic error is due to the BFIA using the unbounded model equation to estimate the body surface potentials. The effects of systematic error are shown in **Figure 4.14** by the offset in the numbered dipole location in the cardiac dipole trajectory and the physical location of the exit site.

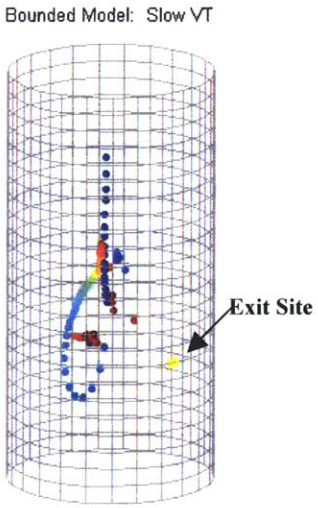

Figure 4.14: Dipole location trajectory for Bounded Model of slow VT. The color gradient from dark blue to dark red represents the initial (blue) localized dipole from the VT Cycle Length (VTCL) to the last (red) localized cardiac dipole in the VTCL under evaluation. The yellow patch represents the physical location of the exit site and the number represents the cardiac dipole location in the range [1:VTCL] that corresponds to the estimated time instance of the exit site.

4.12.4 Bounded Model: Fast VT

In the case of the bounded model and fast VT we have two barriers to overcome: (1) distortion due to the interference of consecutive beats of VT and (2) systematic error due to the consideration of boundary effects in the forward problem and the lack of consideration in the inverse problem (BFIA). The ECG simulation result of fast VT using the bounded model is shown in **Figure 4.15**. We applied the exit site criteria to determine the time instance at which the exit site is determined as shown in **Figure 4.16**.

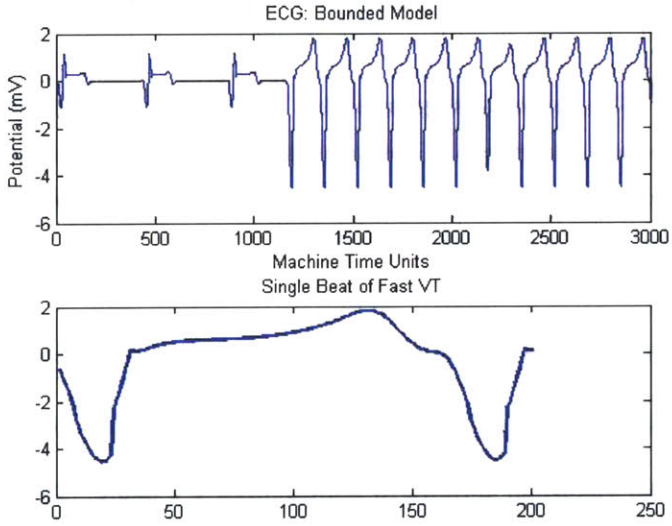

Figure 4.15: Simulation of normal cardiac rhythm, which deteriorates into a fast rate of Ventricular Tachycardia (200 beats per minute) using the Bounded Model. The bottom figure shows a single beat of the fast Ventricular Tachycardia. Note the lack of an isoelectric period that precedes the onset of the QRS complex.

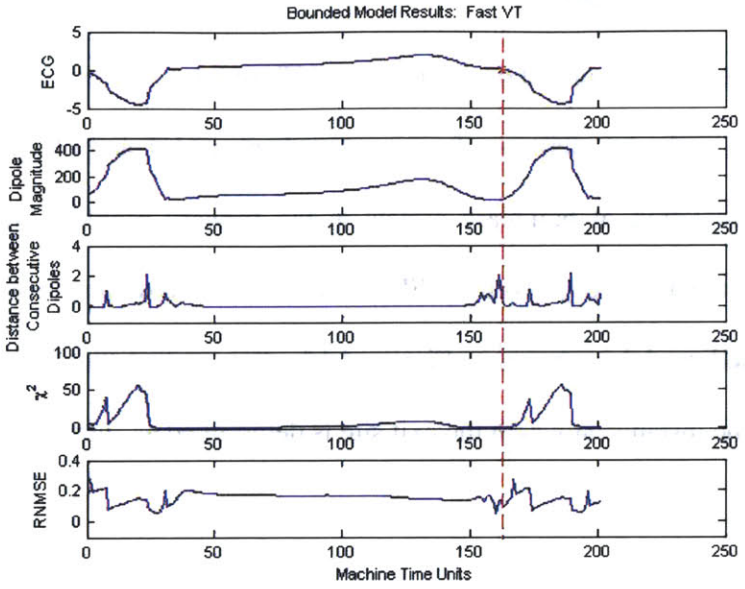

Figure 4.16: The electrocardiogram of fast Ventricular Tachycardia using the bounded model and the exit site criteria (dipole magnitude, distance between consecutive dipoles, χ^2, and Root Normalized Mean Square Error). The red line indicates the time instance corresponding to the occurrence of the exit site.

We did not expect the dipole trajectory to contain a dipole location estimate close to the physical location of the exit site in the case of fast VT due to distortion caused by interference from the electrical activity of consecutive VT beats. This interference in the case of fast VT prevents the BFIA from accurately localizing the exit site as indicated by lack of correlation between the numbered dipole location in **Figure 4.17** and the physical location of the exit site. In addition, the case of the dipole trajectory results using the bounded model on slow VT, the boundary effects create an offset between the exit site and dipole location trajectory as evidenced in **Figure 4.17**.

In addition, we expect the exit site criteria to determine a dipole location estimate from the cardiac dipole trajectory that is far away from the physical location of the exit site when applying the bounded model in the forward problem. The resulting systematic

error is due to the BFIA using the unbounded model equation to estimate the body surface potentials. The effects of systematic error are also shown in **Figure 4.17** by the offset in the numbered dipole location in the cardiac dipole trajectory and the physical location of the exit site.

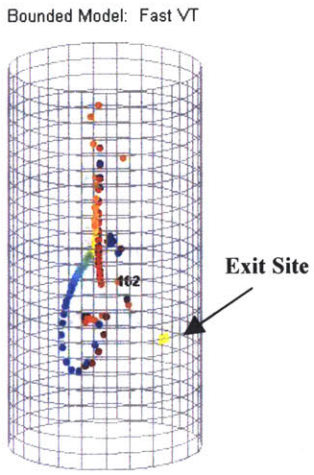

Figure 4.17: Dipole location trajectory for Bounded Model of fast VT. The color gradient from dark blue to dark red represents the initial (blue) localized dipole from the VT Cycle Length (VTCL) to the last (red) localized cardiac dipole in the VTCL under evaluation. The yellow patch represents the physical location of the exit site and the number represents the cardiac dipole location in the range [1:VTCL] that corresponds to the estimated time instance of the exit site.

Chapter 5

Ablation Site Localization in Slow and Fast VT

5.1 Introduction

In slow VT, there is an absence of remote electrical activity in the ventricle at the time that the new wave of depolarization emerges from the exit site. This absence of remote electrical activity at the time the electrical activity emerges from the exit site allows the Brute Force Inverse Algorithm to localize the exit site without additional distortion. The method that we have developed for ablation site localization in slow VT is the Catheter Dipole Method (CDM) and is presented in **Figure 5.1**. In this method we applied sub-threshold current pulses at the catheter tip. The resulting body surface potentials were used as input to the Brute Force Inverse Algorithm, which estimated the parameters of the dipole corresponding to the current pulses, specifically the location of the dipole. A catheter advancement algorithm was used to move the catheter dipole to the VT site of origin dipole.

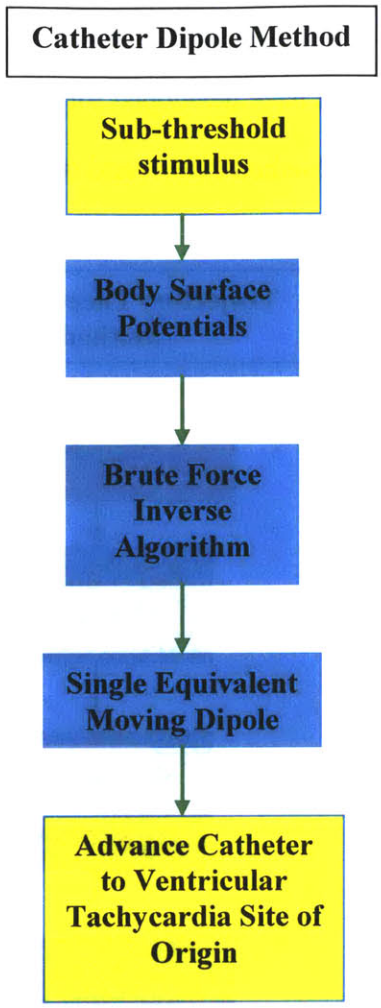

Figure 5.1: Outline of steps for guiding the catheter to the Ventricular Tachycardia site of origin using the Catheter Dipole Method.

In fast VT, remote electrical activity in the ventricle, resulting from previous beats of VT, is present at the time a new wave of depolarization emerges from the exit site. This presence of remote ventricular electrical activity at the time that the new wave of depolarization emerges from the exit site will contribute to the body surface potentials and thus distort the location of the exit site as calculated by the Brute Force Inverse

Algorithm. The method that we have developed for ablation site localization in fast VT is the Trajectory Pace-mapping Method (TPM) and is presented in **Figure 5.2**.

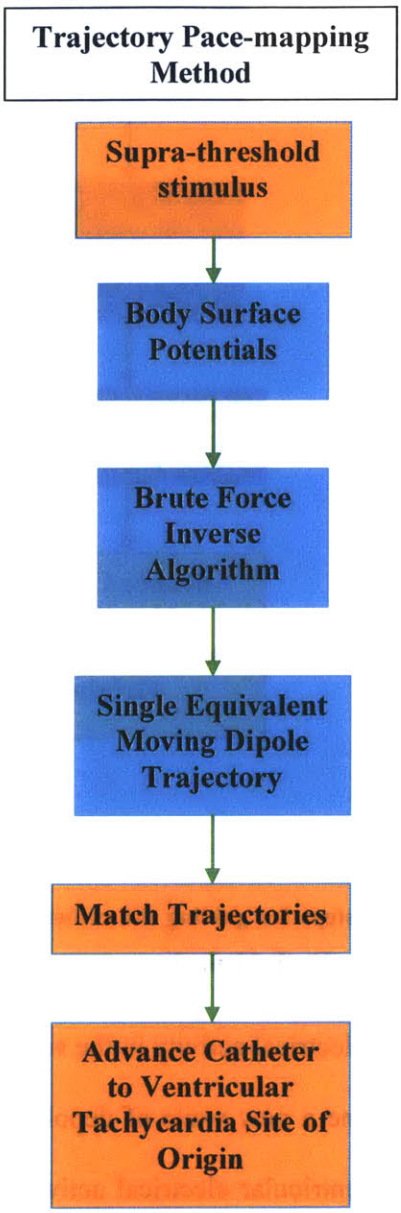

Figure 5.2: Outline of steps for guiding the catheter to the Ventricular Tachycardia site of origin using the Trajectory Pace-mapping Method.

In the Trajectory Pace-mapping Method we stimulated the ventricular myocardium through the electrode on the catheter tip using supra-threshold impulses. The resulting body surface potentials at each point in time were used as input to the Brute Force Inverse Algorithm, in which we estimated the parameters of the corresponding single equivalent moving dipole, resulting in a trajectory in space of cardiac dipoles. The resulting catheter dipole trajectory was compared to the VT site of origin dipole trajectory. Finally, a catheter advancement algorithm was used to move the catheter towards the VT site of origin until the trajectories converged. The advantage of this method is that both the bioelectrical source and the catheter generate a wave of ventricular depolarization and thus both sets of localization estimates should be affected equivalently by the resulting remote ventricular electrical activity.

5.2 Catheter Dipole Method

In the Catheter Dipole Method (CDM), we imaged the current pulse at the catheter tip using sub-threshold stimuli for an instantaneous dipole estimate. I should note that in our simulations we assume for simplicity that the catheter dipole moment had the same orientation as the bioelectrical source dipole. Maya Barley in Dr. Cohen's group has examined the issue of using multiple catheter electrodes to align the catheter and the bioelectrical source dipole orientations. Note that the results from the Brute Force Inverse Algorithm are considered image space solutions while the physical location of the bioelectrical source or catheter tip is defined in real space.

The CDM is essentially a method by which we are attempting to match two dipole locations, one from the bioelectrical source and one from the catheter tip. A flowchart describing the steps of catheter advancement using the CDM is presented in **Figure 5.3**.

Our analysis begins by selecting the best dipole location in the bioelectrical source dipole location trajectory, which results from application of the Brute Force Inverse Algorithm (BFIA). This best dipole location is referred to as the bioelectrical source image location.

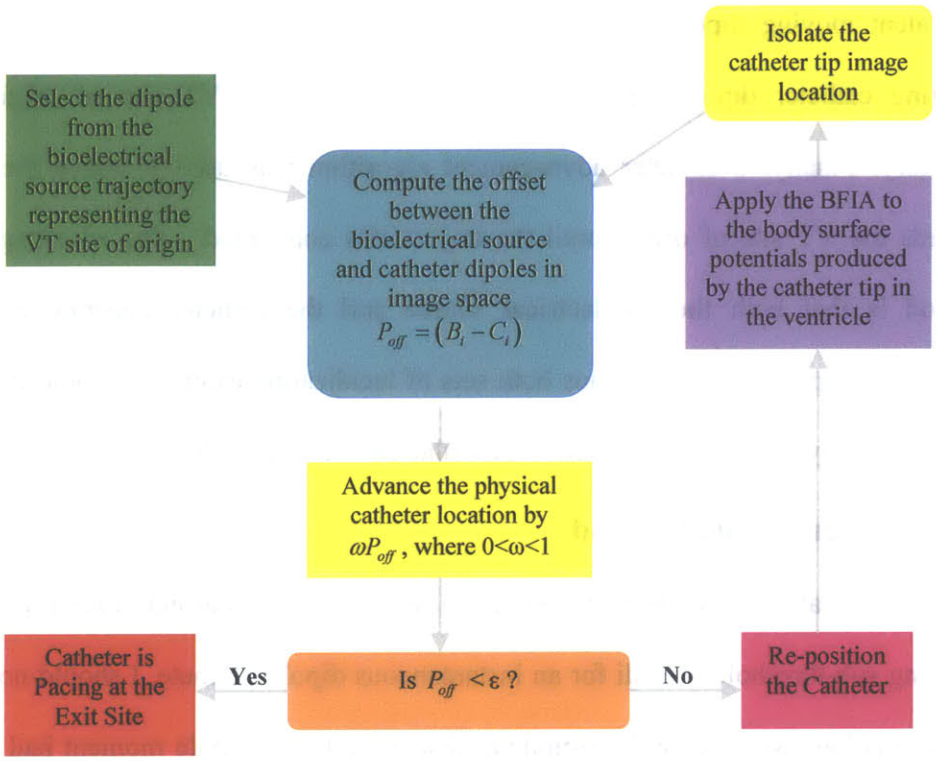

Figure 5.3: Flowchart of catheter advancement algorithm using the Catheter Dipole Method.

We then randomly place the catheter in the ventricle and apply sub-threshold impulses, which do not stimulate the ventricular muscle, to the catheter tip. The BFIA is then used to analyze the body surface potentials produced by the dipole on the catheter tip, which results in a catheter tip image location. After generating the offset vector between the bioelectrical source and catheter image locations, we generate a parallel

vector in real space from the physical catheter location. We advance the catheter along this offset vector by a third. We continue advancing the catheter until the offset vector in image space is less than 0.5 mm.

In the following graphical illustration, **Figure 5.4**, the physical bioelectrical source location (blue closed circle) and resulting image bioelectrical source location (blue open circle) after application of the Brute Force Inverse Algorithm, are shown at the top of the figure while the analogous case for the catheter is shown at the bottom of the figure. The red solid circle represents the physical location of the catheter while the red open circle represents the image location of the catheter.

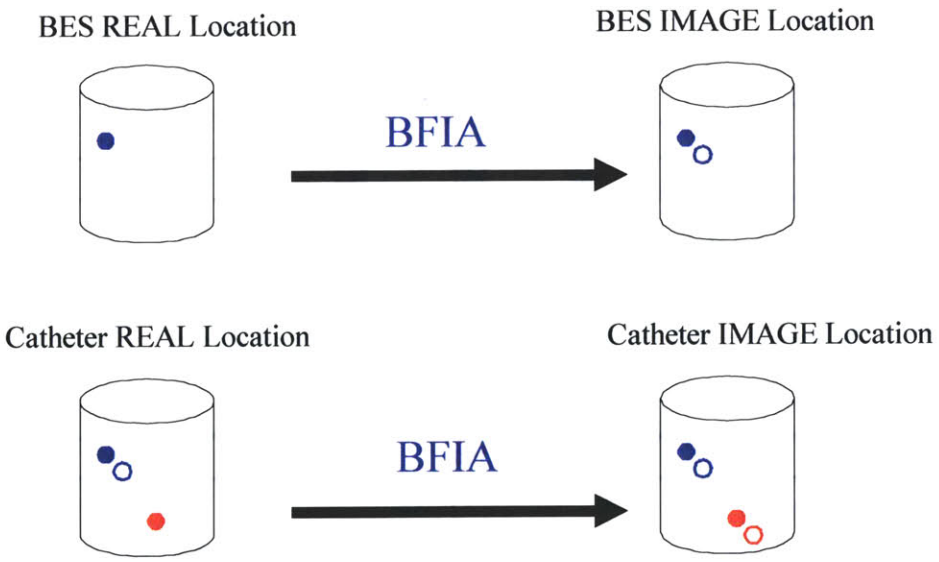

Figure 5.4: Catheter Dipole Method illustration with the physical bioelectrical source location (blue closed circle) and resulting image bioelectrical source location (blue open circle) after application of the Brute Force Inverse Algorithm. The red solid circle represents the physical location of the catheter and the red open circle represents the image location of the catheter.

Recall that in order to determine the bioelectrical source image dipole shown in **Figure 5.4**, we used a set of criteria developed by Maya Barley[111] in the Cohen Lab to determine the point in time when the electrical excitation emerges from the exit site. The criteria involved an analysis of the ECG, and the traces of the following parameters determined by the Brute Force Inverse Algorithm: dipole magnitude, distance between consecutive dipoles, the error function, chi-squared, and the root normalized mean square error as shown in **Figure 5.5**.

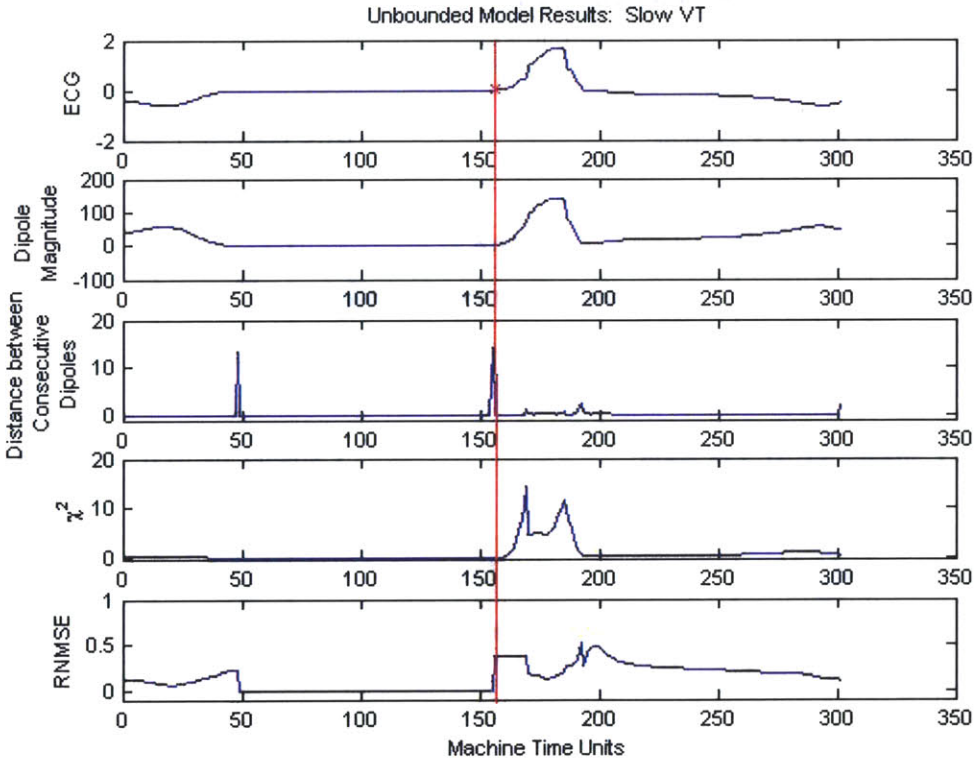

Figure 5.5: Analysis of the exit site criteria for VT site of origin determination from the bioelectrical source data. The red line represents the time instance in the Ventricular Tachycardia cycle length at which the exit site is localized.

The vertical red line at time step 156 denotes the time point in question. Note that the electrical activity first emerges from the exit site prior to the QRS complex. At the time of exit, the dipole magnitude should still be small, the distance between consecutive dipoles reaches a minimum after declining from a peak, the chi squared is small, and the root normalized mean square begins to rise.

In **Figure 5.6**, we show the bioelectrical source dipole location trajectory, represented by circles, inside the cylindrical model corresponding to the beat of Ventricular Tachycardia under analysis. The red square represents the physical location of the exit site. We see that in the case of slow VT with no noise that the bioelectrical source trajectory's dipole number 156 in fact corresponds to the physical exit site location. Therefore, we conclude that the BFIA is correct in its localization of the bioelectrical source's VT site of origin in this particular case.

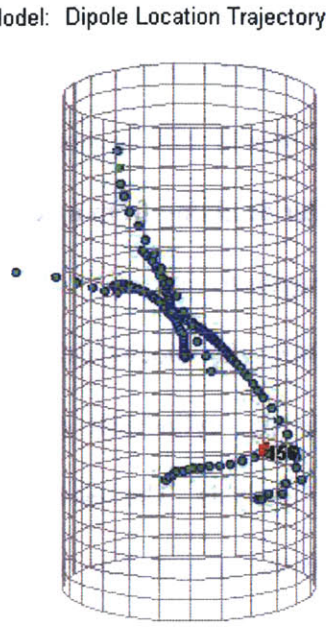

Figure 5.6: Bioelectrical Source dipole location trajectory (circles) and physical location of the exit site (red) on the ventricular model.

Since we have generated the bioelectrical source image, we next generate the catheter image, which is accomplished by application of the BFIA on the body surface potentials produced from the catheter tip dipole. The advancement of the catheter in image and real space is illustrated in **Figure 5.7**. We generate the offset vector between the bioelectrical source and catheter dipole image locations. Afterwards, we assume that we can incrementally move the catheter from the position in **Figure 5.7A** to the position in **Figure 5.7B** along a parallel vector in real space. The equation we use is as follows, $C_{k+1}^{R} = C_{k}^{R} + \omega\left(\vec{B}_{k}^{I} - \vec{C}_{k}^{I}\right)$. Here ω is a fraction between 0 and 1, typically we used 1/3. We continue advancement of the catheter until the bioelectrical source and catheter image are less than 0.5 mm apart.

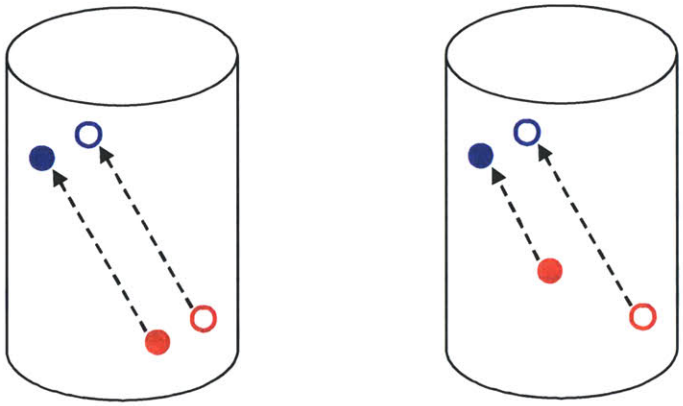

A B

Figure 5.7A and B: Illustration of catheter advancement on the cylindrical model where the red circles represent the catheter dipole location and the blue circles represent the bioelectrical source dipole location. Filled circles represent the location in physical space and open circles represent the location in image space.

5.3 Catheter Dipole Method Results

We tested performance of the Catheter Dipole Method with no noise and low to very high noise levels (1 to 100 μV) on slow VT as shown in **Figure 5.8**. Using the Catheter Dipole Method we obtained good results for the unbounded model as well as bounded model even though the Brute Force Inverse Algorithm assumes an unbounded model. This is because the distorting effect of the bounded model is the same for the bioelectrical source dipole and catheter dipole in slow VT.

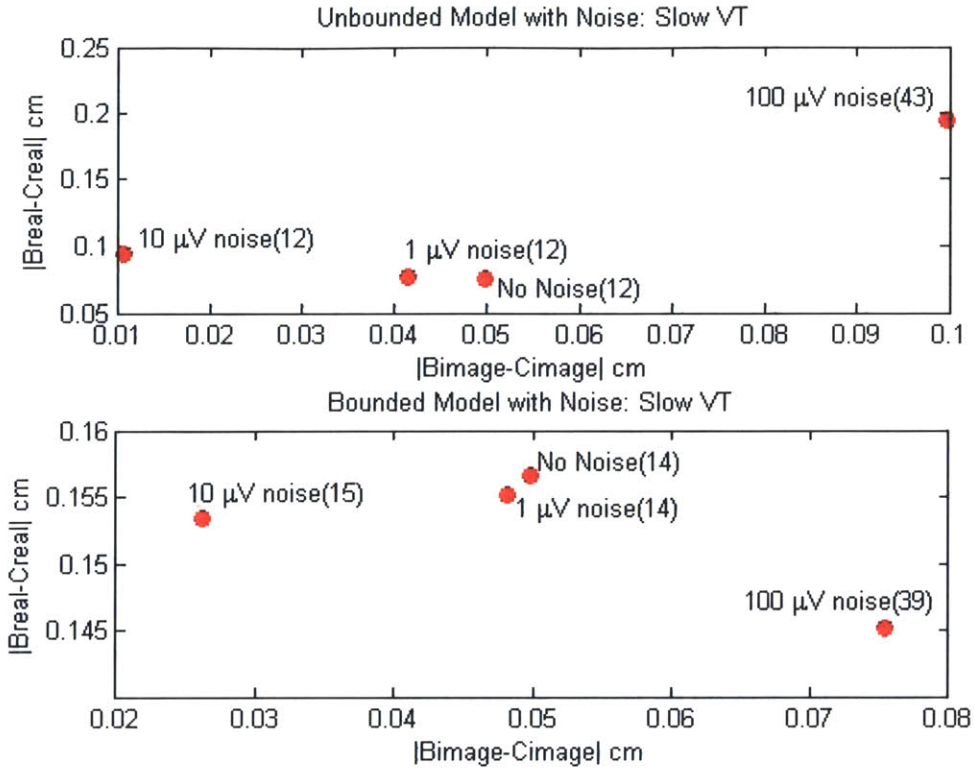

Figure 5.8: Catheter Dipole Method results for slow VT with no noise to very high noise levels of 100 μV. The x-axis gives the offset in image space between the bioelectrical source and catheter source dipoles when the catheter advancement procedure is terminated; the y-axis provides the corresponding offset in real space between the exit site and the location of the catheter tip. The number of steps until the Catheter Dipole Method converged is indicated in parenthesis to the left of the noise level.

In the unbounded and bounded model cases of slow VT, we see that for 0 to 100 μV noise levels, the catheter is successfully advanced to the bioelectrical source in both image and real space within 2 mm. Note that for 0 to 10 μV noise levels, the Catheter Dipole Method converges in 15 steps or less while for the very high noise level of 100 μV, the method converges in approximately 40 steps in the unbounded and bounded model cases. Actual anticipated noise levels are on the order of 10 μV.

As expected, the Catheter Dipole Method does a poor job of localizing the catheter and guiding it to the bioelectrical source in real space for fast VT. In fast VT remote ventricular electrical activity persists at the time that a new wave of electrical activity emerges from the exit site. This remote ventricular activity alters the body surface potentials generated by the bioelectrical source dipole at the VT site of origin, but not the body surface potentials generated by the catheter source. The altered body surface potentials result in a distorted estimate of the location of the bioelectrical source dipole.

There is no similar distortion of the estimate of the location of the catheter dipole. Thus although one can achieve convergence of the imaged locations of the VT site of origin dipole and the catheter dipole, the real locations of the exit site and catheter tip do not converge as shown in **Figure 5.9**. In our results, there was an offset of over 4.5 centimeters in the unbounded model case of fast VT and over 3.5 centimeters in the bounded model case of fast VT. These results inspired us to apply a more sophisticated approach to address bioelectrical source and catheter dipole convergence in fast VT, thus the Trajectory Pace-mapping Method.

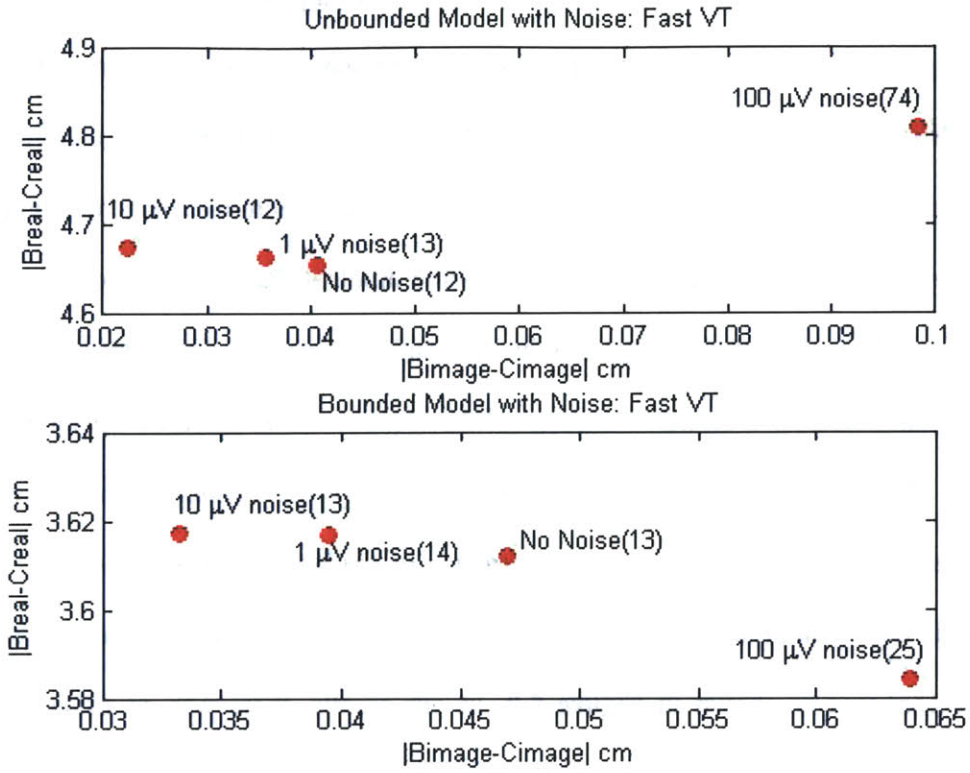

Figure 5.9: Catheter Dipole Method results for fast VT with no noise to very high noise levels of 100 μV. The x-axis gives the offset in image space between the bioelectrical source and catheter source dipoles when the catheter advancement procedure is terminated; the y-axis provides the corresponding offset in real space between the exit site and the location of the catheter tip. The number of steps until the Catheter Dipole Method converged is indicated in parenthesis to the left of the noise level.

5.4 Trajectory Pace-Mapping Method

The objective in matching the bioelectrical source and catheter dipole trajectories is to isolate the initially well-localized dipole locations in the vicinity of the onset of the QRS complex. Admittedly, we could have manually selected the points to be used in the trajectory comparisons, but instead we developed a simple algorithm to automatically select those points for computational convenience. Once we have the bioelectrical source and catheter trajectories, we compute the offset between the two sets of points. In a

subsequent version of this algorithm, it may be useful to develop an algorithm containing evaluation of a smoothness criterion in order to automatically select the optimal points for a trajectory match since we observed that the distance between consecutive dipoles monotonically increases in the localized region of interest.

We observed that the sequence of points immediately following the discontinuity in the distance between consecutive dipoles when the electrical activity starts, coincided with the highly localized bioelectrical source trajectory in the Trajectory Pace-mapping Method (TPM). This discontinuity is due to the Brute Force Inverse Algorithm's attempt to localize the cardiac dipole parameters in the region preceding the onset of VT, but in fact is only fitting the parameters to noise. The Brute Force Inverse Algorithm (BFIA) consistently computes an outlier in the region of noise resulting in computation of a sequence of sporadic distances between consecutive dipoles for the cardiac dipole solutions. A notable change occurs in the distance between consecutive dipoles when the electrical activity transitions from noise to meaningful electrical signals, which initially corresponds to the highly localized region of interest and signals that we should begin selection of the sequence of points for our bioelectrical source trajectory.

Isolating the catheter dipole location trajectory was particularly straightforward in that the electrical activity at the catheter tip is highly localized at the ventricle location when the stimulus is applied, before spreading to depolarize the rest of the ventricle. Therefore, we automatically selected the initial points after application of the stimulus to the catheter tip in order to select the catheter trajectory points of interest. In the following sections we will present the method of localizing the exit site of the reentry

circuit in both slow and fast VT. We found it necessary to make minor changes to the Trajectory Pace-mapping Method for fast VT.

5.4.1 Trajectory Pace-mapping Method for Slow VT

A sequential analysis of the Trajectory Pace-mapping Method for slow VT and corresponding figures are provided in the following steps:

1. *Extract one VTCL of the bioelectrical source from the ECG*
2. *Compute the distance between consecutive dipoles,* d_{cons}

The ECG of slow VT using the Unbounded Model along with corresponding distances between consecutive dipoles is shown in **Figure 5.10**. Note that in the middle sub-figure that the distances between consecutive dipoles are extremely large, exceeding 20 cm while the ventricle is only 9 cm long. This characteristic is due to the fact that the Brute Force Inverse Algorithm (BFIA) cannot localize the cardiac dipole in the region preceding the QRS onset in slow VT because it is essentially fitting the cardiac dipole parameters to noise. We capitalize on this characteristic to isolate the electrical activity as it emerges from the exit site of the reentry circuit.

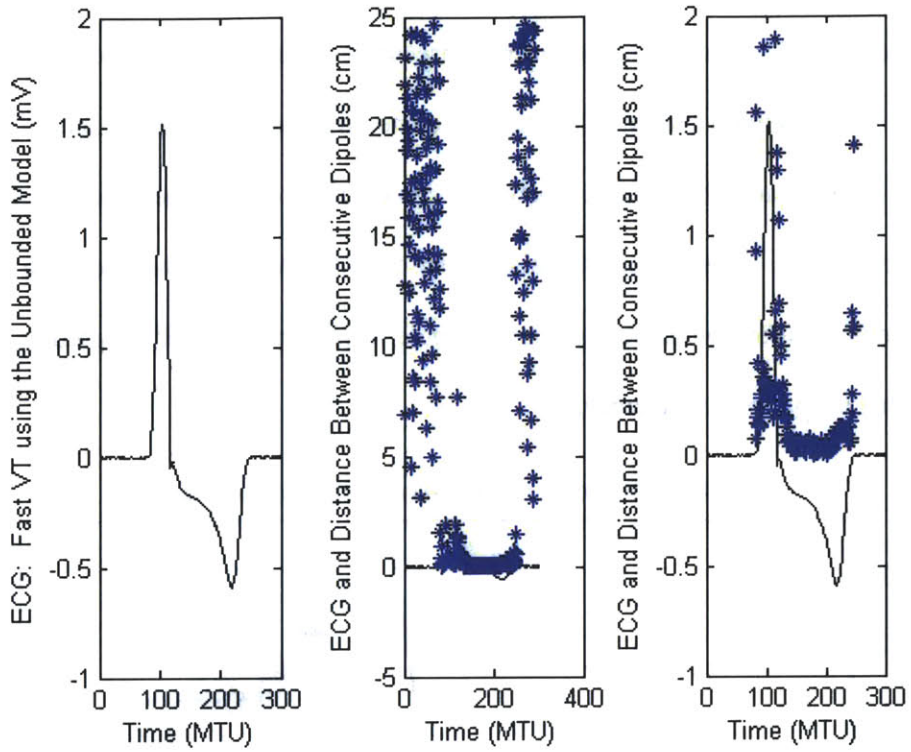

Figure 5.10: The first figure shows an ECG of Slow Ventricular Tachycardia (VT) using the Unbounded Model with noise added to the electrodes. The second figure is of the ECG and the VT's corresponding distance between consecutive dipoles (blue) and the third figure is a magnified version of the second figure to more closely observe the distance between consecutive dipoles in our region of interest where the electrical activity emerges from the exit site.

3. *Select the sequence of consecutive, well-localized dipole locations following* $d_{cons} > 0$.

4. *Observe the first 5 dipole locations following the discontinuity in the distance between consecutive dipoles.*

Recall that the cardiac tissue rests immediately before initiation of the period of highly localized electrical activity. We sought to isolate those points immediately following the period of isoelectric activity as shown in **Figure 5.11**. During the isoelectric region, the Brute Fore Inverse Algorithm fits the dipole to noise and

consistently computes a dipole solution without the presence of cardiac electrical activity. This explains why the distance between consecutive dipoles is sporadic in the case of noise and would remain the same in the case of no noise until the BFIA actually reaches localized activity and the distance between consecutive dipole increases in a smooth, consistent manner. This feature signals the onset of the VT and we select the first five points to represent the bioelectrical source dipole trajectory that will be used to compare to the catheter tip dipole trajectory.

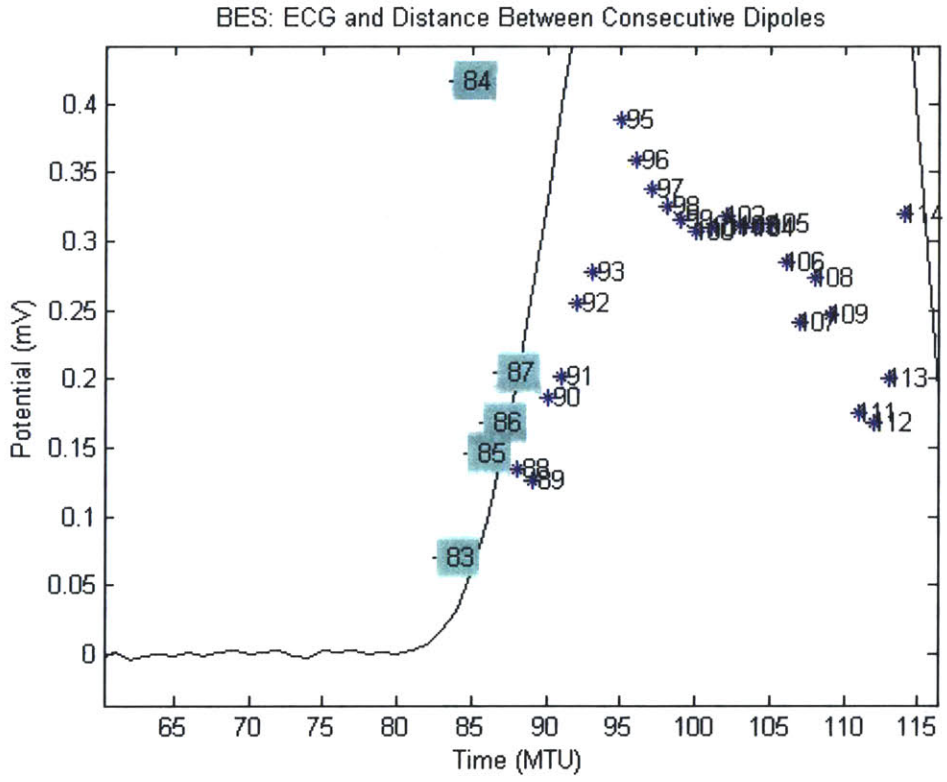

Figure 5.11: Bioelectrical source with the numbered points in the Ventricular Tachycardia cycle length to be used in the Trajectory Pace-mapping Method. The points are selected by observing the initial instance when the distance between consecutive dipoles follows a roughly monotonically increasing pattern (highlighted in blue).

5. *Select a sequence of 5 dipole locations following the paced catheter sequence.*

Upon delivery of the pacing impulse to the catheter, the initial cardiac dipole locations determined by the BFIA indicate those that are appropriate for matching to the bioelectrical source trajectory. The cardiac dipole locations of interest from the catheter are shown in **Figure 5.12**.

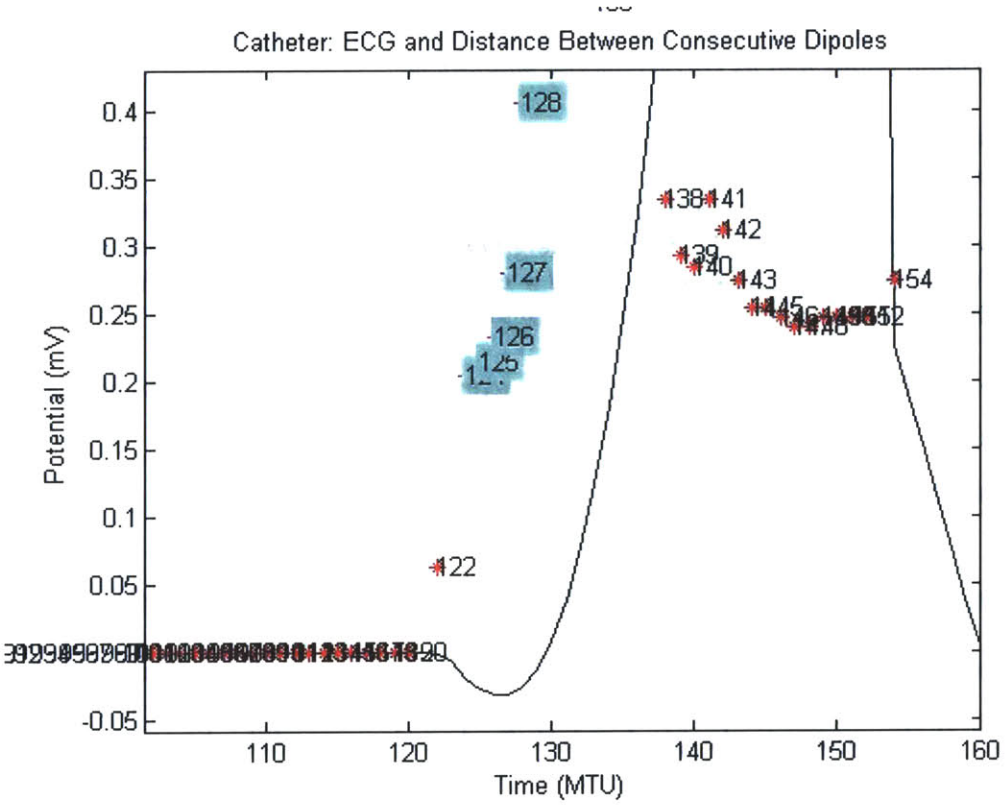

Figure 5.12: Catheter source with the numbered points in the Ventricular Tachycardia cycle length to be used in the Trajectory Pace-mapping Method. The points are selected by observing the initial instance when the distance between consecutive dipoles follows a roughly monotonically increasing pattern (highlighted in blue).

6. *Compute the offset vector between bioelectrical source and Catheter location trajectory points,* $d_{off}\frac{\sum_{i=1}^{N}(B_i - C_i)}{N}$, *where N is the number of points in the trajectory.*

7. *Advance the Catheter by a fraction of the offset vector, $w*d_{off}$, where $w = ½$.*

8. *Project the new catheter position onto the cylindrical surface via a lookup table of all the model element center locations.*
    a. *If the z-component of d_{off} remains the same and is smaller than scz, we move the z-component up by 2*scz if the algorithm was initially moving upwards and down by 2*scz if the algorithm was initially moving downwards*

9. *Compute the offset vector between the physical bioelectrical source and Catheter location points and its corresponding magnitude*

10. *Run the brute force inverse algorithm, BFIA, on the new physical Catheter location*
11. *If the catheter remains at the same location, check the d_{off} results from moving the catheter to each of the four nearest neighbors 2*scz, where scz = 2 mm, the linear dimension of the ventricular model's elements. Choose the neighbor and its corresponding trajectory that results in the minimum d_{off}*

    a. *If the catheter is pacing in the scar tissue, move the catheter back to its previous location*

12. *Repeat steps 7 –12 in an iterative loop until $|d_{off}| < 1.5*scz$*

An illustration of the method by which we attempt to advance the catheter dipole to the bioelectrical source dipole is shown in **Figure 5.13**. In this illustration, the yellow perforated circle represents the bioelectrical dipole trajectory while the red perforated square represents the catheter dipole trajectory. The offset between the two trajectories is measured by computing an average of the sum of differences of all the dipoles in the respective trajectories. This offset vector is represented by $\vec{\lambda}_k$, whose equation is $\vec{\lambda}_k = \sum_{i=1}^{N} \frac{\left(\vec{C}_i - \vec{B}_i\right)}{N}$. In this equation, *k* represents the current number is the sequence of catheter moves until trajectory convergence is attained, N is the number of dipole

locations in the trajectory, $\vec{C}$ represents the catheter trajectory, and $\vec{B}$ represents the bioelectrical source trajectory.

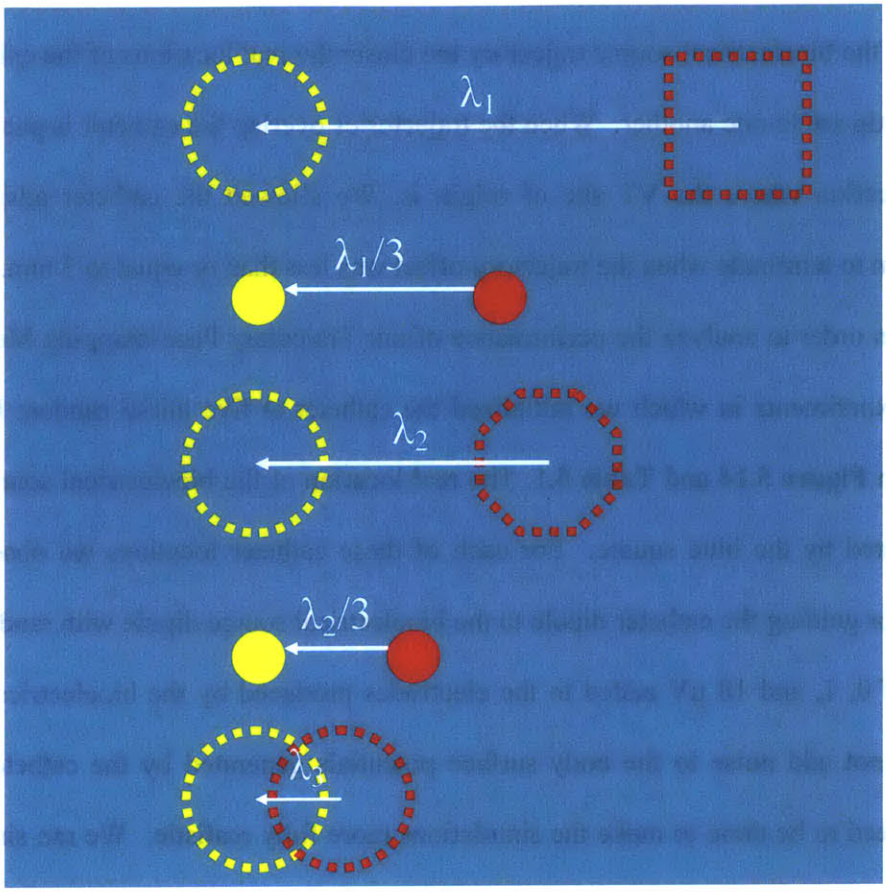

Figure 5.13: Catheter advancement algorithm for the Trajectory Pace-mapping Method. The yellow perforated circle represents the bioelectrical dipole trajectory in image space while the yellow solid circle represents the physical location of the bioelectrical source dipole when the electrical activity emerges from the exit site. The red perforated shapes represent the catheter dipole trajectory while the solid red circle represents the physical location of the catheter on the ventricular surface. The $\vec{\lambda}_k$ is the offset vector used in both image and real space to advance the catheter a third of the distance in sequential steps until the desired resolution is attained.

We create a vector parallel to $\vec{\lambda}_k$ in real space and advance the catheter along this offset vector by a fraction of $\vec{\lambda}_k$, in this case 1/2. We continue this process and as we indicate in the illustration, the shape of the catheter trajectory will begin to morph into the shape of the bioelectrical source trajectory the closer the real locations of the exit site and catheter tip are to one another. When the trajectories overlap the catheter is pacing at the same location where the VT site of origin is. We allowed the catheter advancement algorithm to terminate when the trajectory offset was less than or equal to 3 mm.

In order to analyze the performance of our Trajectory Pace-mapping Method, we set up experiments in which we initialized the catheter at five initial random locations, shown in **Figure 5.14** and **Table 5.1**. The real location of the bioelectrical source dipole is indicated by the blue square. For each of these catheter locations we observed the results for guiding the catheter dipole to the bioelectrical source dipole with random noise levels of 0, 1, and 10 μV added to the electrodes produced by the bioelectrical source. We did not add noise to the body surface potentials generated by the catheter, which would need to be done to make the simulations more fully realistic. We ran simulations for slow and fast VT using both the unbounded and bounded models.

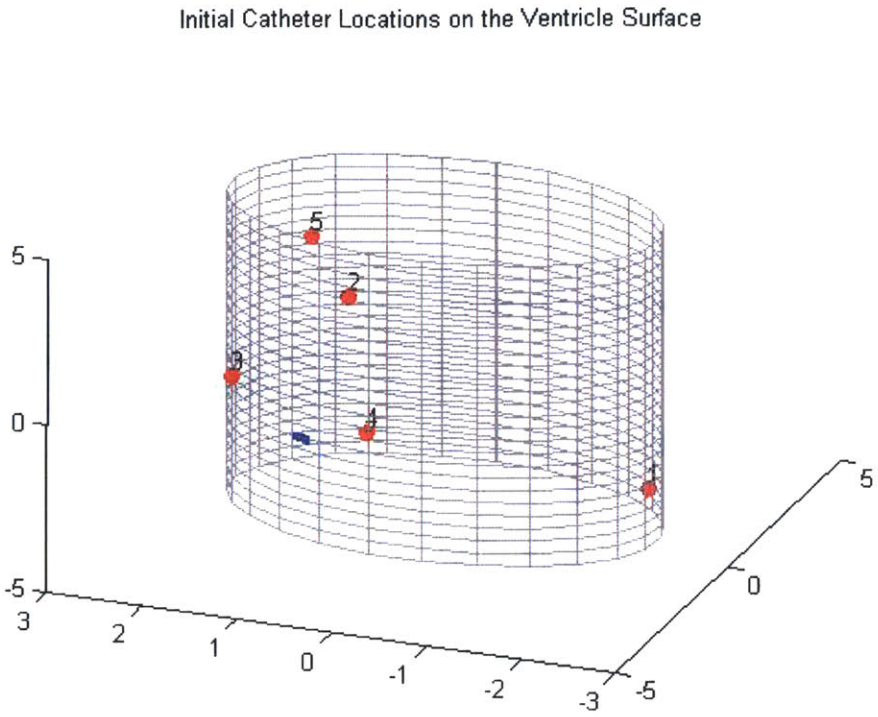

Figure 5.14: Initial catheter locations (red and numbered 1-5) and physical location of the exit site (blue) on the surface of the ventricular finite element model.

Trial	Initial Catheter Distance from Exit Site (cm)
#1	4.9834
#2	4.6384
#3	1.5879
#4	0.9939
#5	5.0088

Table 5.1: Initial catheter distance from the exit site in the five trials under observation.

5.4.2 Results: Trajectory Pace-mapping Method for Slow VT

The bioelectrical source and catheter five point trajectories for trial #1 of slow VT using the Unbounded model with no noise converged in five steps as shown in **Figure**

5.15. Note that as the catheter is paced closer to the exit site, the bioelectrical source and catheter trajectory morphologies look more similar and overlap. In physical space, the catheter converged towards the exit site as shown in **Figure 5.16**.

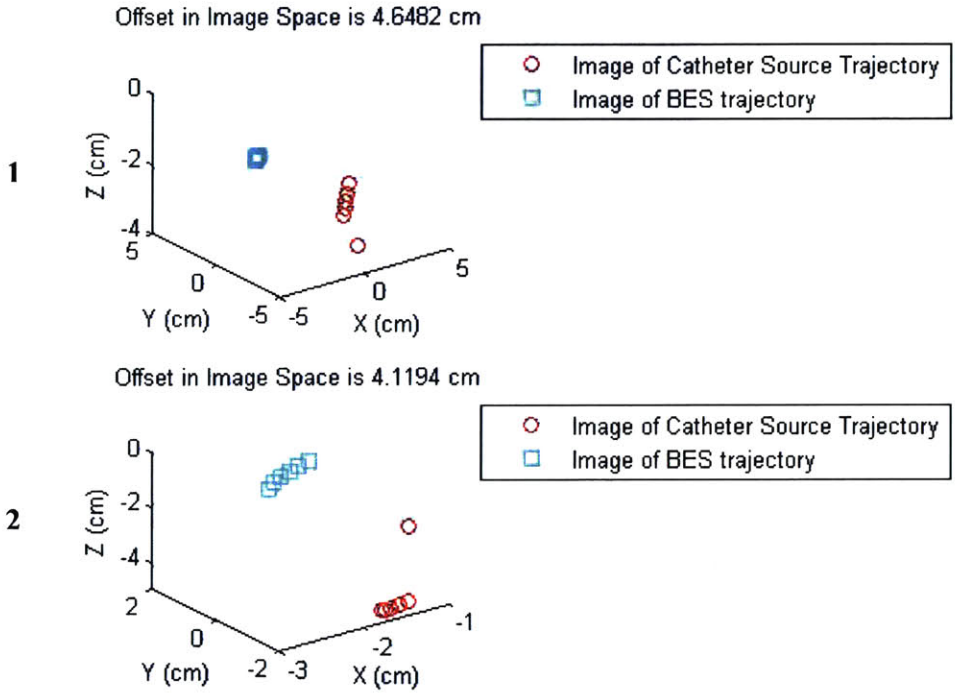

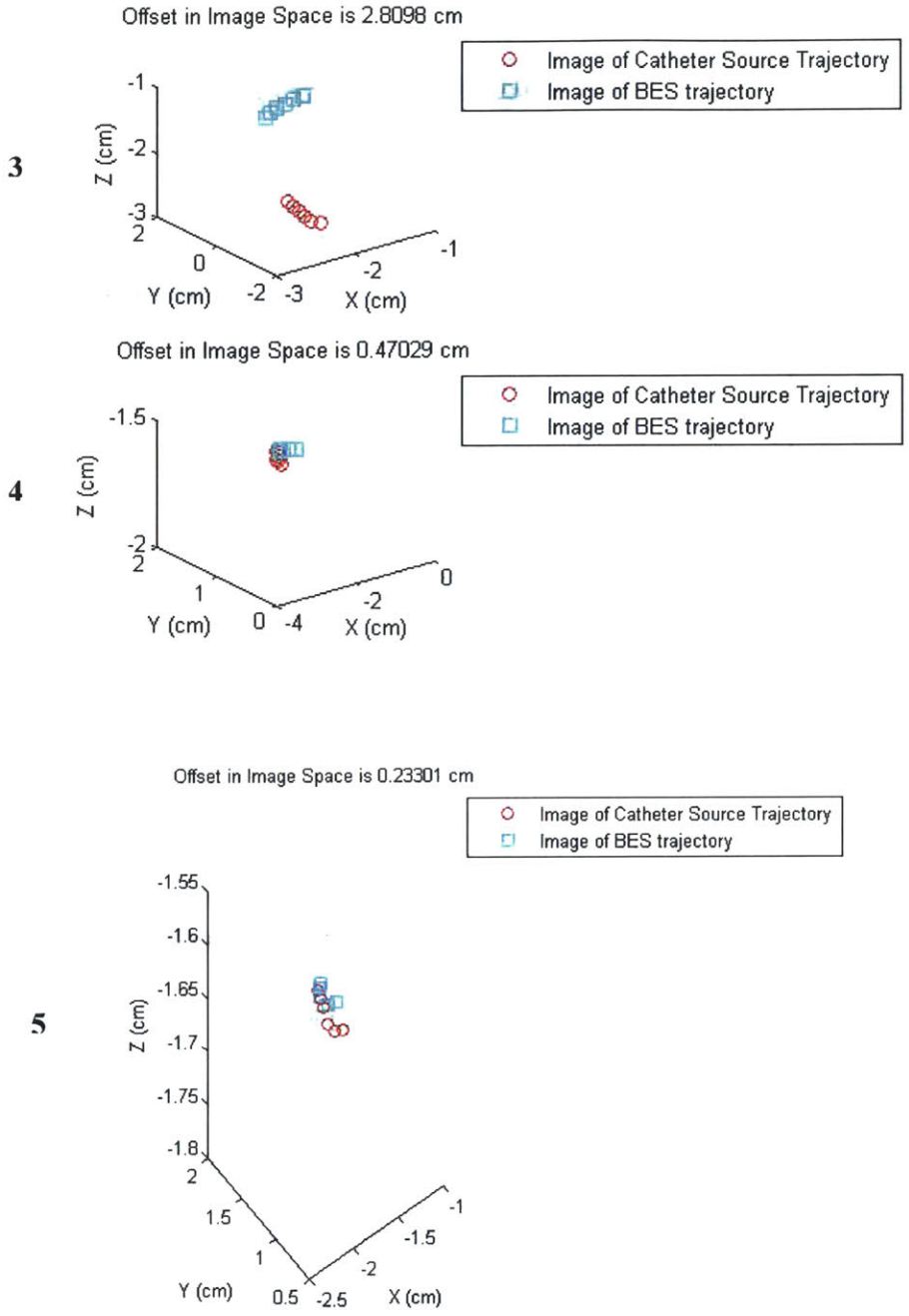

Figure 5.15: Example of a complete sequence (1-5) of catheter (red) and bioelectrical source (blue) trajectories extracted from each respective cardiac dipole trajectory for a Ventricular Tachycardia cycle length. The corresponding offset is indicated at the top of each individual plot. This is in the example of slow VT using the Unbounded Model.

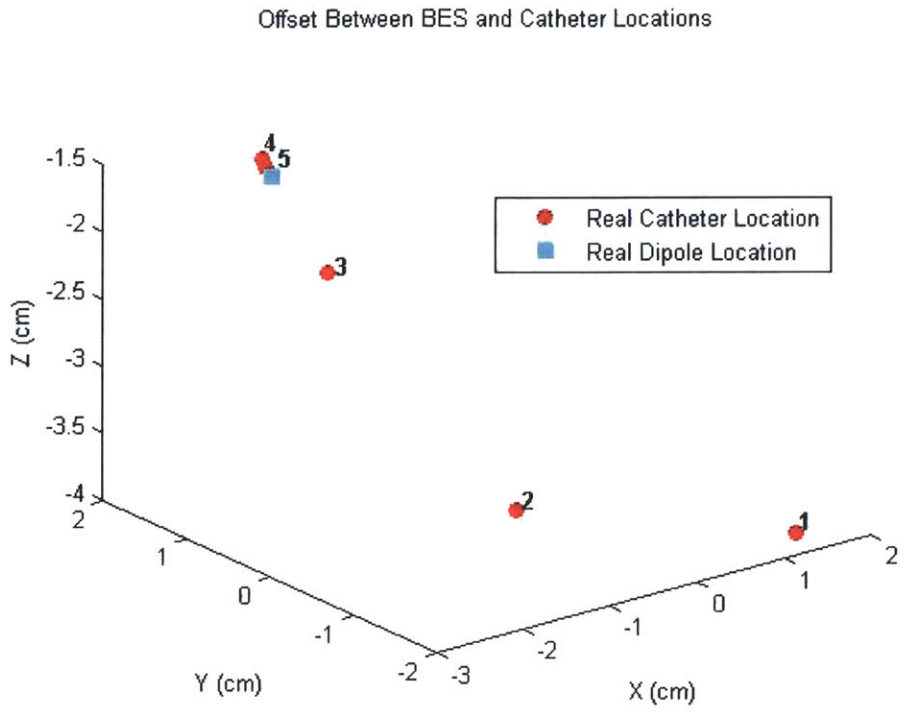

Figure 5.16: Catheter advancement (red) towards the exit site (blue) using the Trajectory Pace-mapping Method. This is in the example of slow VT using the Unbounded Model.

The experimental results for the unbounded and bounded models for slow VT in which a catheter was randomly placed in the ventricle and guided towards the bioelectrical source dipole are shown in **Figure 5.17** and **Figure 5.18**. The number of steps until convergence in image space is indicated in parenthesis left of the labeled noise level. Note that one experiment was conducted for each noise level in each trial. Recall that the ventricular model's individual elements had a linear dimension of 2 mm so we were satisfied when the catheter and bioelectrical source dipoles converged in physical, or real, space within two elements, or 4 mm. In the case of no noise, we achieved the desired convergence resolution in the unbounded model. However, the ability to advance

the catheter to the bioelectrical source dipole progressively worsened as we introduced more noise to the potentials generated by the bioelectrical source.

With the bounded model in slow VT, we also achieved the desired convergence in the case of no noise. However, the ability to advance the catheter to the bioelectrical source dipole progressively worsened as we introduced more noise to the potentials generated by the bioelectrical source.

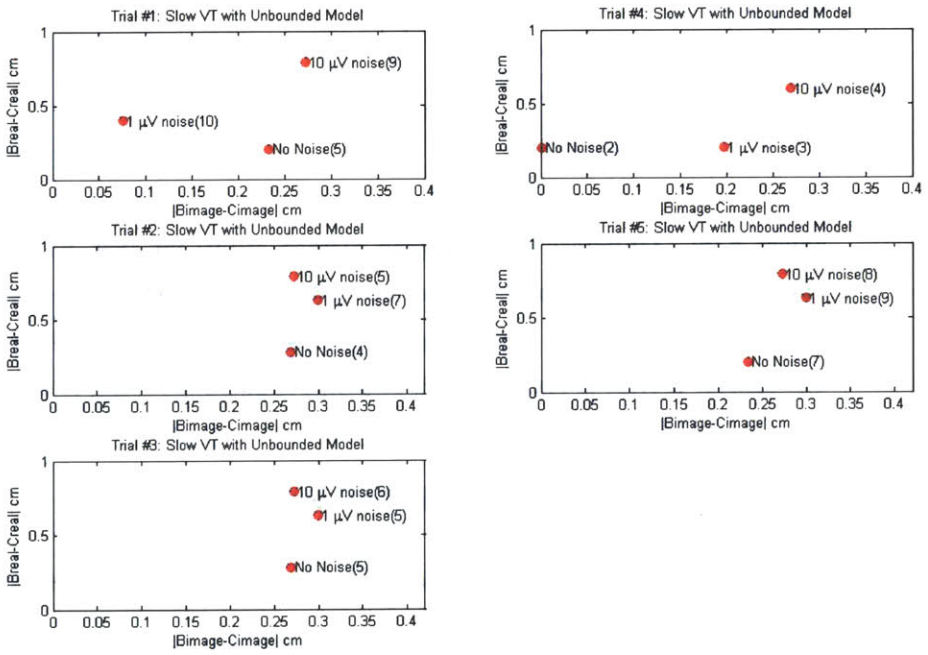

Figure 5.17: Trajectory Pace--mapping Method results for slow VT using the Unbounded Model with the final displacement of the catheter and bioelectrical source trajectories in image space (x-axis) and physical space (x-axis) for the 5 initial catheter locations tested. The number of steps to convergence is indicated in parenthesis next to the noise level.

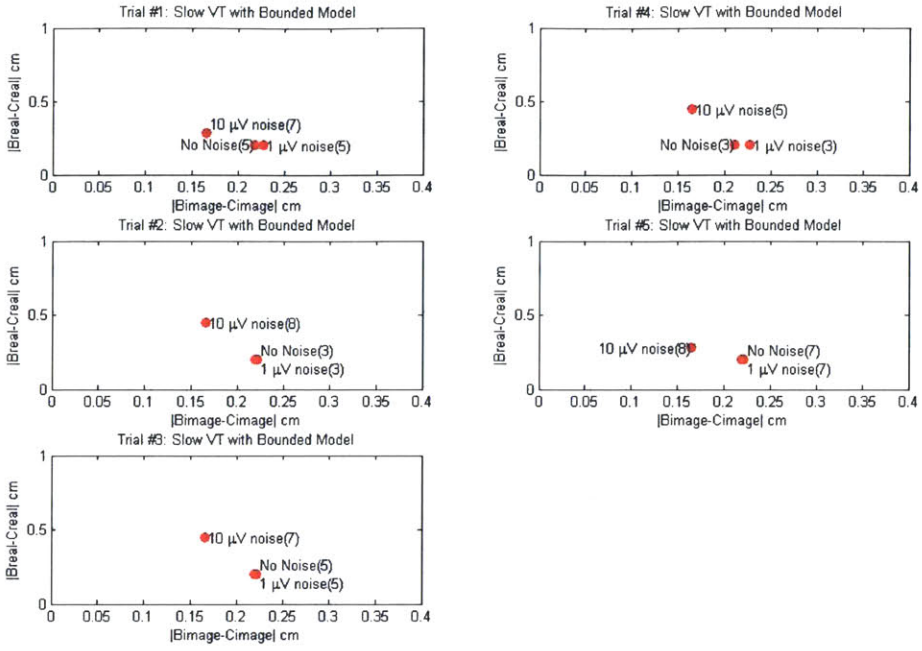

Figure 5.18: Trajectory Pace-mapping Method results for slow VT using the Bounded Model with the final displacement of the catheter and bioelectrical source trajectories in image space (x-axis) and physical space (x-axis) for the 5 initial catheter locations tested. The number of steps to convergence is indicated in parenthesis next to the noise level.

5.4.3 Trajectory Pace-mapping Method for Fast VT

A sequential analysis of the Trajectory Pace-mapping Method for fast VT using the Unbounded Model and corresponding figures is provided in the following steps. Please note that the differences between the TPM algorithm for slow and fast VT are noted in *red* below.

1. *Extract one VTCL of the bioelectrical source, bioelectrical source, from the ECG*
2. *Compute the distance between consecutive dipoles, d_{cons}*

The ECG along with the corresponding distance between consecutive dipoles is shown in **Figure 5.19**. Note that the distance between consecutive dipoles progressively increases in the vicinity of the QRS onset to the peak in the QRS complex.

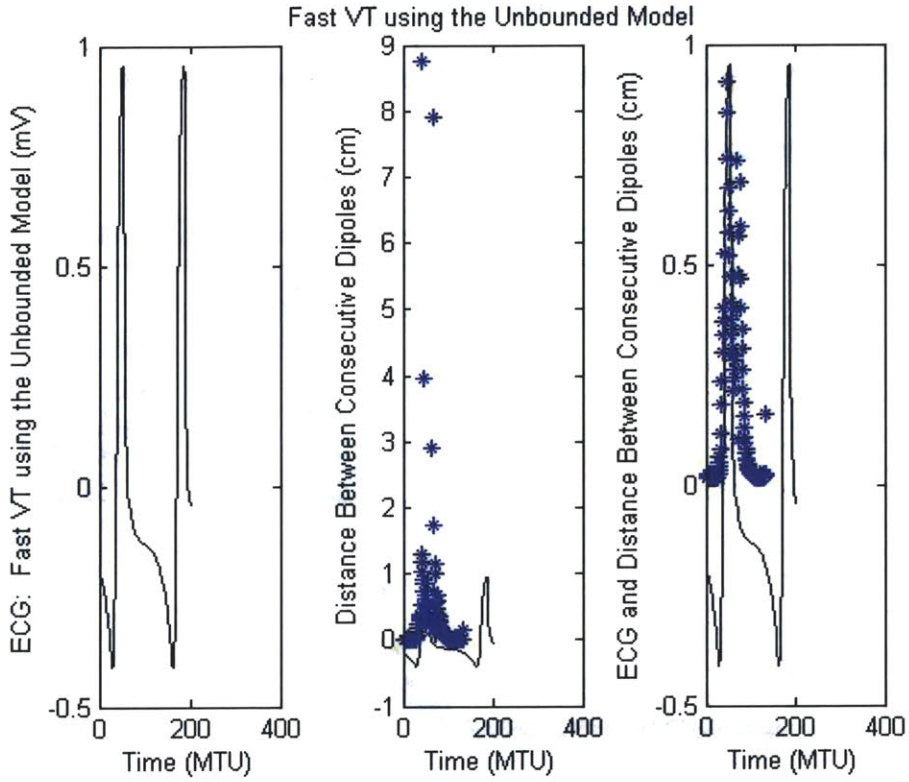

Figure 5.19: The first figure shows an ECG of Fast VT using the Unbounded Model with noise added to the electrodes. The second figure is of the ECG and the VT's corresponding distance between consecutive dipoles (blue) and the third figure is a magnified version of the second figure to more closely observe the distance between consecutive dipoles in our region of interest where the electrical activity emerges from the exit site.

3. *Select the sequence of consecutive, well-localized dipole locations following* $d_{cons} > scz$

4. *Observe the first 5 dipole locations following the discontinuity in the distance between consecutive dipoles. This is the bioelectrical source trajectory.*

The region in the Ventricular Tachycardia cycle length of fast VT distorted by the electrical interference from consecutive beats of VT should precede the onset of the QRS

complex. We found that the distance between consecutive dipoles was initially small during this period of distortion, but started to monotonically increase in the vicinity of the exit site of the reentry circuit. We sought to isolate the cardiac dipole locations of interest by setting a threshold of 2 mm for the points under evaluation as shown in **Figure 5.20**. This is the region of the bioelectrical source trajectory that will be matched to the paced catheter trajectory.

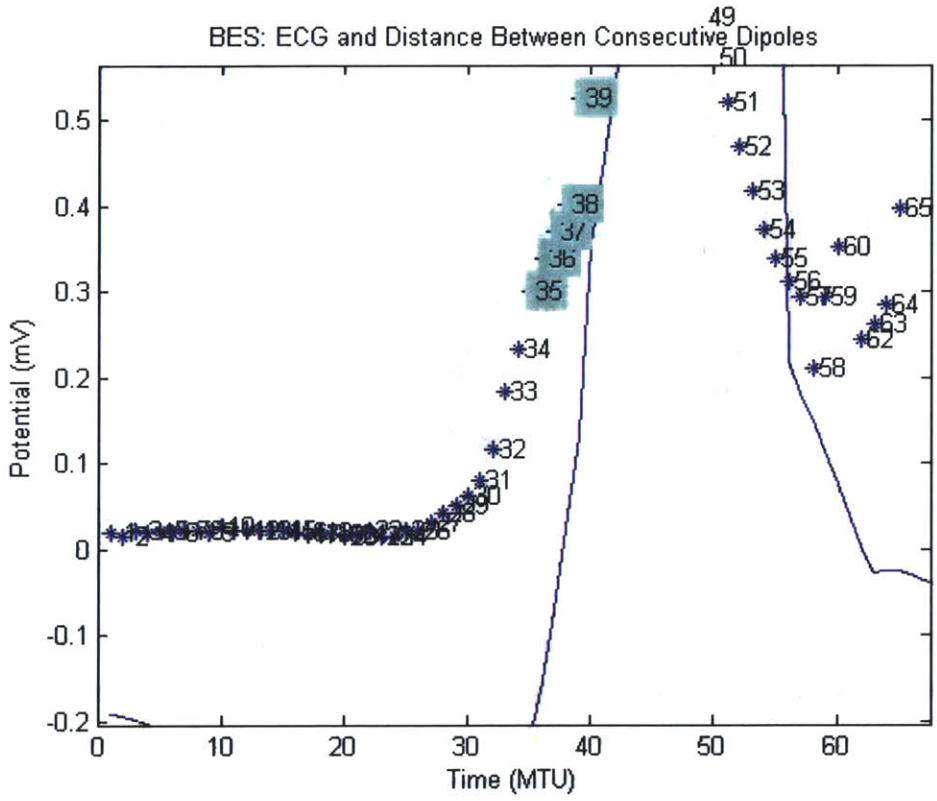

Figure 5.20: Bioelectrical source with the numbered points in the Ventricular Tachycardia cycle length to be used in the Trajectory Pace-mapping Method. The points are selected by observing the initial instance when the distance between consecutive dipoles follows a roughly monotonically increasing pattern (highlighted in blue).

5. *Select a sequence of 5 dipole locations following the paced catheter sequence. This is the catheter trajectory.*

Upon delivery of the pacing impulse to the catheter, the initial cardiac dipole locations determined by the Brute Force Inverse Algorithm indicate those that are appropriate for matching to the bioelectrical source trajectory. The cardiac dipole locations of interest from the catheter are distinguished in **Figure 5.21**. We used the same catheter advancement algorithm used in slow VT shown in **Figure 5.13** to guide the catheter to the VT site of origin.

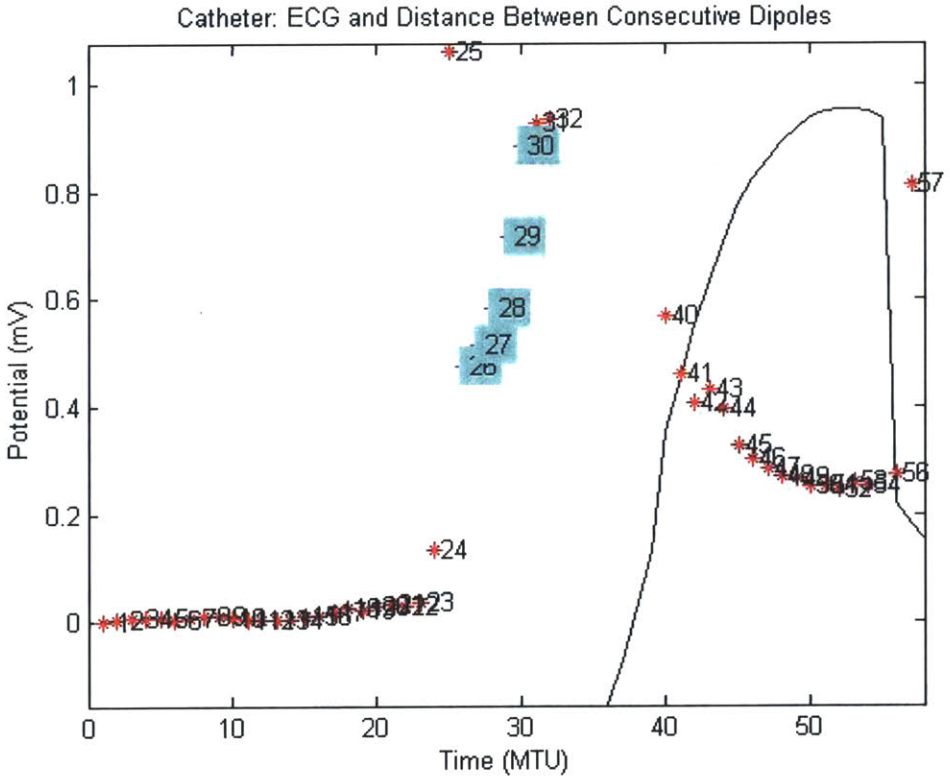

Figure 5.21: Catheter source with the numbered points in the Ventricular Tachycardia cycle length to be used in the Trajectory Pace-mapping Method. The points are selected by observing the initial instance when the distance between consecutive dipoles follows a roughly monotonically increasing pattern (highlighted in blue).

6. *Compute the offset vector between bioelectrical source and Catheter location trajectory points,* $d_{off} \frac{\sum_{i=1}^{N}(C_i - B_i)}{N}$, *where N is the number of points in the trajectory*

7. *Advance the Catheter by a fraction of the offset vector,* $w*d_{off}$, *where* $w = ½$

8. *Project the new catheter position onto the cylindrical surface via a lookup table of all the model element center locations.*

    a. *If the z-component of* d_{off} *remains the same and is smaller than scz, we move the z-component up by 2*scz if the algorithm was initially moving upwards and down by 2*scz if the algorithm was initially moving downwards*

9. *Compute the offset vector between the physical bioelectrical source and Catheter location points and its corresponding magnitude*

10. *Run the brute force inverse algorithm, BFIA, on the new physical Catheter location*

11. *If the catheter remains at the same location, check the* d_{off} *results from moving the catheter to each of the four nearest neighbors 2*scz, where scz = 2 mm, the linear dimension of the ventricular model's elements. Choose the neighbor and its corresponding trajectory that results in the minimum* d_{off}

    a. *If the catheter is pacing in the scar tissue, move the catheter back to its previous location*

12. *Repeat steps 7 –12 in an iterative loop until* $|d_{off}| < 1.5*scz$

5.4.4 Results: Trajectory Pace-mapping Method for Fast VT

The bioelectrical and catheter trajectories for trial #1 with no noise in which convergence was accomplished in nine steps are shown in **Figure 5.22**. Note that as the catheter is paced closer to the exit site, the bioelectrical source and catheter trajectory morphologies look more similar and overlap. In physical space, the catheter converged towards the exit site as shown in **Figure 5.23**.

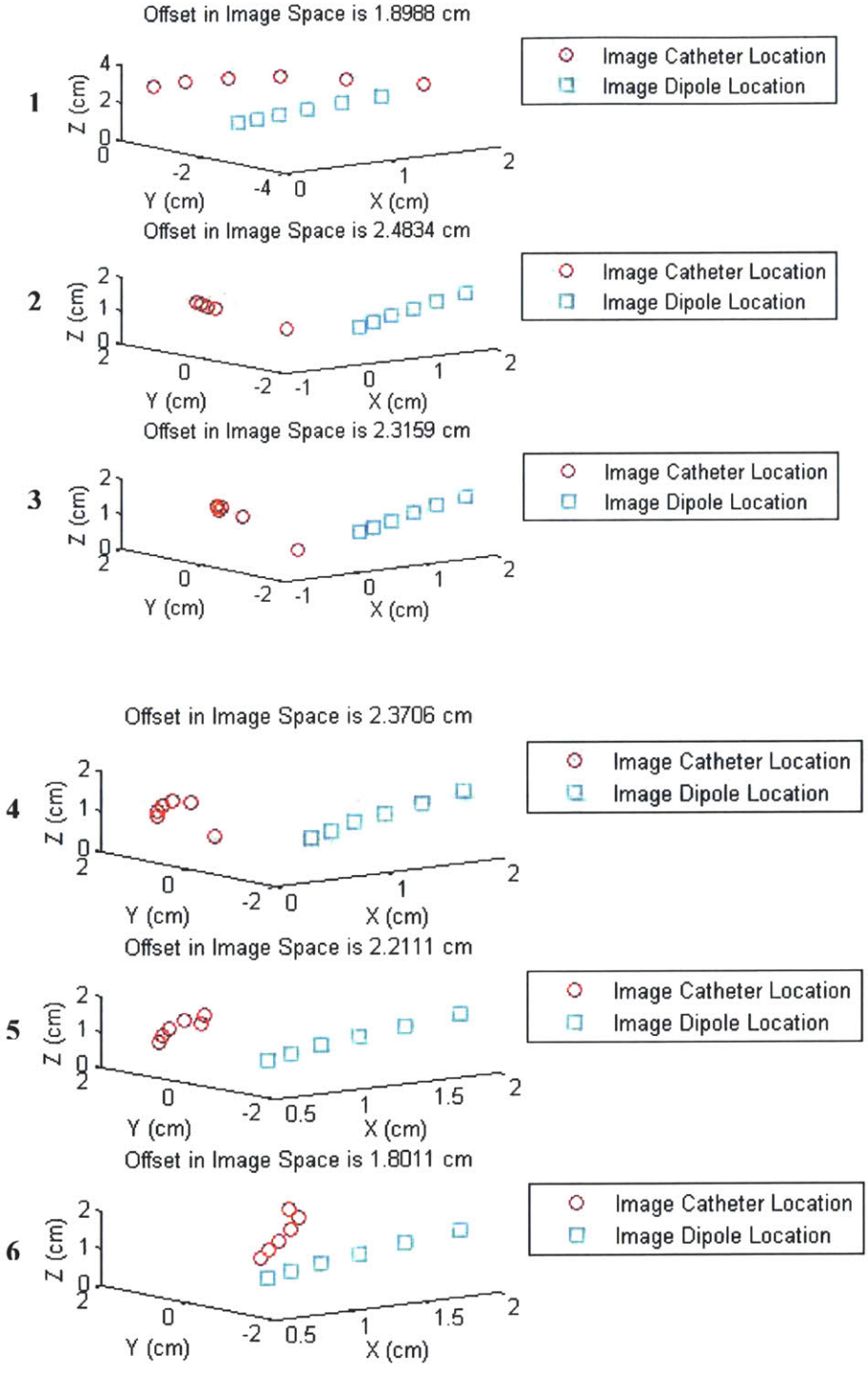
Offset in Image Space is 1.8988 cm
1
Z (cm)
Y (cm)
X (cm)
Image Catheter Location
Image Dipole Location
Offset in Image Space is 2.4834 cm
2
Z (cm)
Y (cm)
X (cm)
Image Catheter Location
Image Dipole Location
Offset in Image Space is 2.3159 cm
3
Z (cm)
Y (cm)
X (cm)
Image Catheter Location
Image Dipole Location
Offset in Image Space is 2.3706 cm
4
Z (cm)
Y (cm)
X (cm)
Image Catheter Location
Image Dipole Location
Offset in Image Space is 2.2111 cm
5
Z (cm)
Y (cm)
X (cm)
Image Catheter Location
Image Dipole Location
Offset in Image Space is 1.8011 cm
6
Z (cm)
Y (cm)
X (cm)
Image Catheter Location
Image Dipole Location

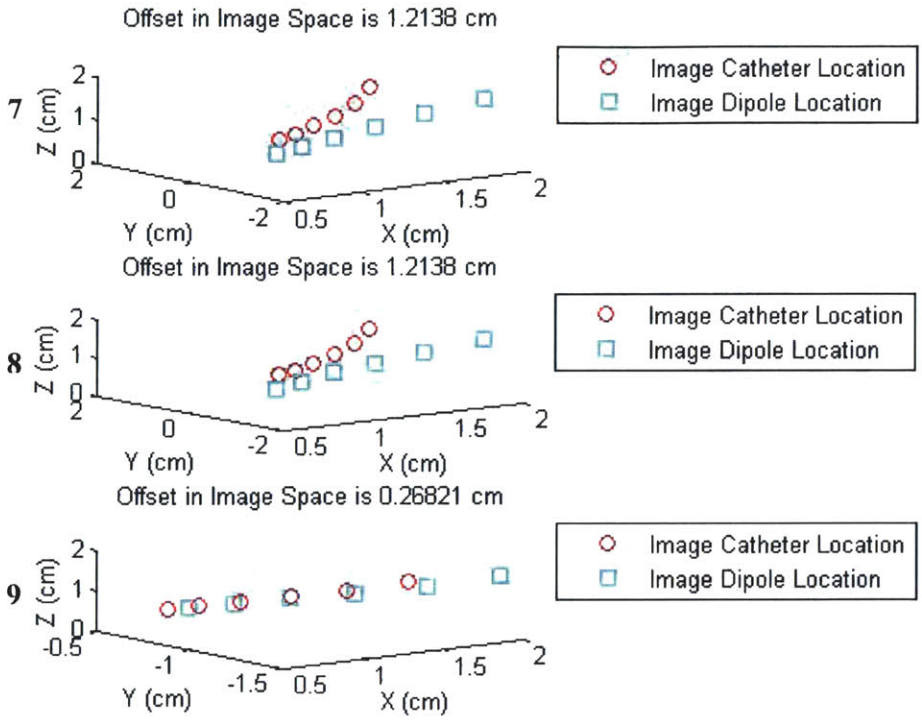

Figure 5.22: Example of a complete sequence (1-9) of catheter (red) and bioelectrical source (blue) trajectories extracted from each respective cardiac dipole trajectory for a Ventricular Tachycardia cycle length. The corresponding offset is indicated at the top of each individual plot. This is in the example of fast VT using the Unbounded Model.

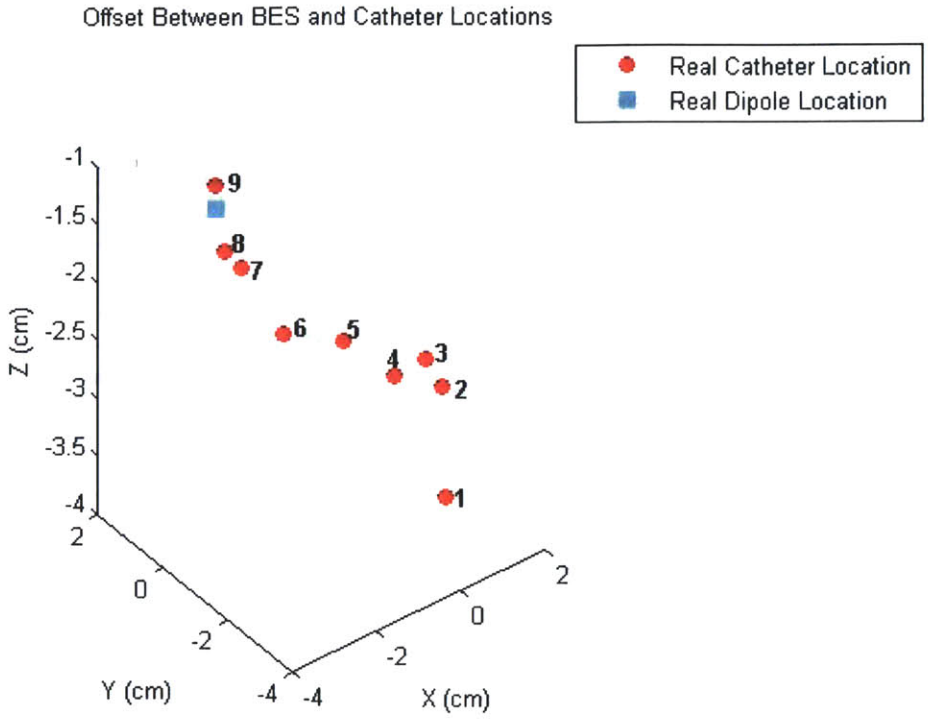

Figure 5.23: Catheter advancement (red) towards the exit site (blue) using the Trajectory Pace-mapping Method. This is in the example of fast VT using the Unbounded Model.

The experimental results utilizing the Unbounded and Bounded Models for fast VT in both image and physical space of the five trials are presented in **Figure 5.24** and **Figure 5.25**. In the case of fast VT, note that we achieve the desired convergence of less than 4 mm in real space for the unbounded model for all of the noise levels analyzed. We observed dipole trajectory convergence with this method because both the bioelectrical source and the catheter source generate a wave of ventricular depolarization and thus both sets of localization estimates are affected equivalently by the resulting remote ventricular electrical activity.

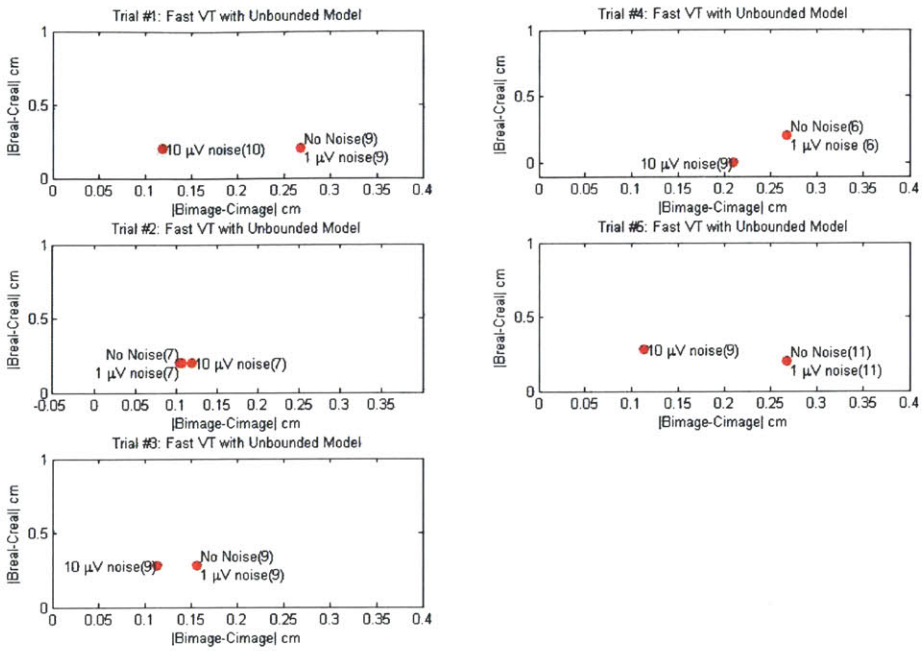

Figure 5.24: Trajectory Pace--mapping Method results for fast VT using the Unbounded Model with the final displacement of the catheter and bioelectrical source trajectories in image space (x-axis) and physical space (x-axis) for the 5 initial catheter locations tested. The number of steps until convergence is indicated in parenthesis next to the noise level.

In the bounded model case of fast VT, note that we achieve the desired convergence of less than 4 mm in real space for all noise levels analyzed. We conclude from the Trajectory Pace-mapping Method results for slow and fast VT that this method appears to be an effective algorithm for ablation site localization in both slow and fast VT.

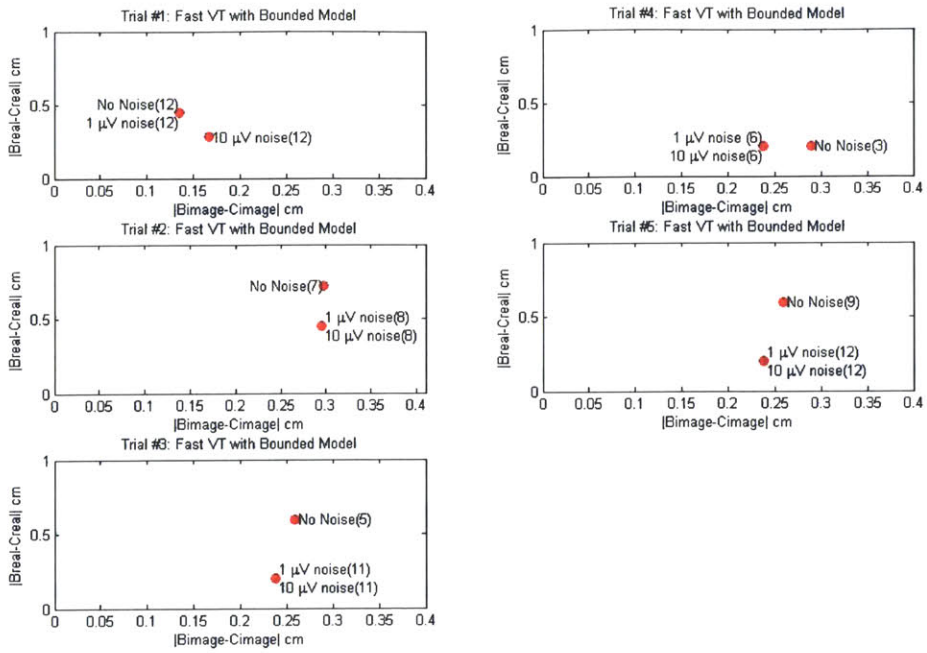

Figure 5.25: Trajectory Pace--mapping Method results for fast VT using the Bounded Model with the final displacement of the catheter and bioelectrical source trajectories in image space (x-axis) and physical space (x-axis) for the 5 initial catheter locations tested. The number of steps until convergence is indicated in parenthesis next to the noise level.

Chapter 6

Summary of Results and Future Goals

6.1 Completed Research Objectives

Our research objectives for this thesis were to design a finite element model to simulate VT, develop an algorithm to localize the exit site of a reentry circuit using body surface potentials, localize the ablation catheter in both slow and fast VT, and advance the ablation catheter to the localized exit site of the reentry circuit. We were able to successfully simulate various rates of Ventricular Tachycardia through development of a simple finite element model of ventricular conduction.

We also developed the Brute Force Inverse Algorithm to estimate the cardiac dipole parameters at the localized exit site using the Single Equivalent Moving Dipole Model. In addition, we designed and tested the Catheter Dipole Method for localizing the exit site in slow and fast VT. The Catheter Dipole Method was effective in localizing the exit site in slow VT, but was ineffective in the case of fast VT. Thus, we developed the Trajectory Pace-mapping Method, in which the exit site was localized for both the unbounded and bounded model cases of slow and fast VT.

6.2 Detailed Summary of Results

Our first objective was to develop a finite element model of ventricular electrical activity in order to simulate various rates of VT resulting from reentry. The model was simple and deterministic, providing a straightforward method for generating body surface

potentials corresponding to the ventricular electrical activity. Because we were interested in the case of VT resulting from structural heart disease, we superimposed an area of scar tissue on the ventricular model to accommodate the formation of reentry. Through the development and application of excitation and conduction rules using a cellular automata model, we were able to successfully generate electrocardiograms for both slow and fast rates of VT.

Our second objective was to develop an algorithm to localize the VT site of origin, or exit site of the reentry circuit, from a single beat of VT. This algorithm, the Brute Force Inverse Algorithm (BFIA), estimated the cardiac dipole parameters of a Single Equivalent Moving Dipole (SEMD) representation of cardiac electrical activity from the body surface potentials at each point during the cardiac cycle. The SEMD model represented the heart as a bioelectrical source modeled by a single equivalent dipole whose location, magnitude and direction varies throughout the cardiac cycle. For each point in time, the BFIA estimated the location and moment of a single equivalent moving dipole resulting in a trajectory in space of cardiac dipoles. Finally the dipole trajectory was analyzed to determine which point corresponded to the exit site of the reentry circuit. Results from the BFIA in both slow and fast VT using the unbounded and bounded model results proved to be reliable.

Our third objective was to localize the ablation catheter and advance it to the VT site of origin. To guide the catheter to the VT site of origin in slow VT, we developed the Catheter Dipole Method. In this method we applied sub-threshold current pulses at the catheter tip. The resulting body surface potentials were used as input to the Brute Force Inverse Algorithm, which estimated the parameters of the dipole corresponding to

the current pulses, specifically the location of the dipole. By analyzing the SEMD trajectory from the VT simulation (bioelectrical source), the dipole corresponding to the VT site of origin was identified. A catheter advancement algorithm was used to move the catheter dipole to the VT site of origin dipole. The Catheter Dipole Method was successful in localizing the VT site of origin in slow VT, but was unsuccessful in fast VT because in fast VT remote ventricular electrical activity altered the body surface potentials generated by the bioelectrical source dipole at the VT site of origin but not the body surface potentials generated by the catheter source.

To guide the catheter to the VT site of origin in fast VT, we developed the Trajectory Pace-mapping Method. In this method we applied supra-threshold current pulses to the catheter tip to stimulate the ventricular myocardium. The resulting body surface potentials at each point in time were used as input to the Brute Force Inverse Algorithm to estimate the parameters of the corresponding SEMD, resulting in a trajectory in space of cardiac dipoles. The resulting catheter dipole trajectory was compared to the VT site of origin dipole trajectory. Finally, a catheter advancement algorithm was used to move the catheter towards the VT site of origin until the trajectories converged. We observed dipole trajectory convergence in both slow and fast VT with this method because both the bioelectrical source and the catheter source generate a wave of ventricular depolarization and thus both sets of localization estimates should be affected equivalently by the resulting remote ventricular electrical activity.

Through the simulation of VT due to reentry, development of the Brute Force Inverse Algorithm for VT site of origin localization through analysis of the SEMD model, localization of the ablation catheter tip though development of the Catheter

Dipole Method and Trajectory Pace-mapping Method, and guidance of the ablation catheter to the VT site of origin, we were able to provide a complete simulation of a new approach to RFA. The proposed new RFA procedure would allow therapy for patients who cannot tolerate the maintenance phase and frequent inductions of VT, by increasing the accuracy and speed by which we determine the site for ablation. In principle, our RFA technique only requires a single beat of VT to localize the VT site of origin. The proposed new RFA procedure promises to provide a new rapid and effective means for treatment of VT. Future animal and human studies are needed to validate the approaches we have developed.

6.3 Future Direction of Research

In future research, we should validate our approach to Radio-frequency Ablation of Ventricular Tachycardia via saline tank experiments, which are currently in progress by Maya Barley. As suggested by Armoundas with his approach, in vitro studies, conducted in a saline tank using an anatomically and geometrically realistic saline torso tank and current dipole sources, will prove to be insightful.[110] The body surface potentials will be used to identify the location and moment of the dipoles that were analyzed to generate those potentials. The ability of the Brute Force Inverse Algorithm to localize multiple simultaneously active and spatially separated electrical current sources will be tested. The final step will be to conduct animal and human studies.

Further analysis using the algorithms developed in this thesis can include the following experiments. In the VT simulation model, we could simulate more complex forms of VT and we should note that in the case of polymorphic VT, the exit site may vary widely, constantly changing in shape and size. Thus, there is a need to develop a set

of exit site criteria in VT when the QRS complex is not well defined. Also, we could address the case of reentry circuits located in the myocardium by extending our finite element model to consist of three layers: an epicardium, myocardium, and endocardium.

We could also optimize the Brute Force Inverse Algorithm so that the cardiac dipole parameters are determined in a clinically acceptable time frame. The catheter dipole moment alignment can also be incorporated in catheter guidance using methods developed by Barley.[111] Development of an algorithm to automatically select a subset of points from the bioelectrical source and catheter dipole trajectories for matching by the Trajectory Pace-mapping Method will prove useful. Also, we noted in the Trajectory Pace-mapping Method that noise was not added to the body surface potentials generated by the catheter in our analysis. Noise must be added to the catheter to obtain fully realistic results of the Trajectory Pace-mapping Method. Upon completion of all of these aforementioned experiments, a more robust set of algorithms will be available for clinical purposes.

BIBLIOGRAPHY

[1] Mark R. Quantitative Physiology: Organ Transport Systems. Notes from Principals of Cardiac Electrophysiology Course. 2000.

[2] Zheng Z, Croft JB, Giles WH, Mensah GA. Sudden cardiac death in the United States, 1989 to 1998. *Circulation.* 2001;104:2158-2163.

[3] St. Jude Medical. Tachyarrhythmia (Fast Heart Rate). http://www.sjm.com/conditions/condition.aspx?name=Tachyarrhythmia+(Fast+Heart+Rate)

[4] Engelstein ED, Zipes DP. Sudden cardiac death. In: Alexander RW, Schlant RC, Fuster V, eds. Hurst's The Heart, 9th edition. New York: McGraw Hill, 1998;1081-1112.

[5] MERIT-HF Study Group. Effect of metoprolol CR/XL in chronic heart failure: the Metoprolol CR/XL Randomized Intervention Trial in Congestive Heart Failure (MERIT-HF). *Lancet* 1999;353:2001-2007.

[6] Langberg J, Delurgio D. VI. Ventricular Arrhythmias. In: Dale D, Federman D, eds. Web MD Scientific American. 1999.

[7] Tullo N. Your Heart Rhythm. Cardiac Arrhythmia InfoCenter. http://home.earthlink.net/~avdoc/infocntr/htrhythm/hrintro.htm

[8] Stevenson WG, Friedman PL. Chapter 113: Catheter Ablation of Ventricular Tachycardia. In: Zipes DP, Jalife J, eds. Cardiac Electrophysiology: from Cell to Bedside, 3rd edition. 2000.

[9] Soejima K, Suzuki M, Maisel W, et al. Catheter ablation in patients with multiple and unstable ventricular tachycardias after myocardial infarction: short ablation lines guided by reentry circuit isthmuses and sinus rhythm mapping. *Circulation.* 2001;104:664-669.

[10] Ideker RE, Smith RM, Blanchard SM, et al. The assumptions of isochronal cardiac mapping. *Pace.* 1989;12:436-478.

[11] Martini. Chapter 10: Muscle Tissue. Anatomy and Physiology. http://media.pearsoncmg.com/ph/esm/esm_martini_fundanaphy_5/bb/obj/10/CH10/html/ch10_8.html#Anchor-DIFFERENCES-49575

[12] Weiss TF. Cellular Biophysics *Electrical Properties*. Volume 2. The MIT Press, Cambridge, MA 1997.

[13] Wikipedia. The Free Encyclopedia. http://en.wikipedia.org/wiki/Image:Action_potential.png

[14] Zaza A. Rosen M. An Introduction to Cardiac Electrophysiology. Overseas Publishers Association. 2000.

[15] Berne R, Leby M. Physiology Fourth Edition. Mosby, Inc. 1998.

[16] Klabunde R. Cardiovascular Physiology Concepts.

http://www.cvphysiology.com/Arrhythmias/A006.htm

[17] Trudel MC, Gulrajani, RM, Leon LJ. Electrotonic coupling reduces action potential duration gradients in the ventricle: a simulation study. *International Journal of Electromagnetism.* 2002;4:55-56.

[18] Texas Heart Institute. Leading with the Heart. Anatomy of the Human Heart. http://www.tmc.edu/thi/anatomy2.html

[19] Carr JJ. Chapter 1: Introduction to Biomedical Equipment Technology, 2nd edition. Prentice Hall Career and Technology, 1993;10-23.

[20] NASPE Heart Rhythm Society. Patient and Public Information Center. http://www.naspe-patients.org/patients/treatments/catheter_ablation.html

[21] The Encyclopedia of Medical Devices and Instrumentation, Editors. Wiley-Interscience Publication. Vol. 4, 1988.

[22]The Merck Manual of Medical Information--Home Edition. Section 3: Heart and Blood Vessel Disorders. Chapter 15. Illustrations. ECG: Reading the Waves. http://www.merck.com/mrkshared/mmanual_home/illus/15i1.jsp

[23] Lemkin D, Plotnik J. Introduction to EKGs. Electrophysiology. http://davidge2.umaryland.edu/~emig/ekgtu02.html

[24] American Heart Association. Sudden Cardiac Death. http://www.americanheart.org/presenter.jhtml?identifier=4741

[25] Kuller L, Lilienfeld A, Fisher R. Epidemiological study of sudden and unexpected deaths due to arteriosclerotic heart disease. *Circulation.* 1966; 34: 1056–1068.

[26] Doyle JT, Kannel WB, McNamara PM, et al. Factors related to suddenness of death from coronary disease: combined Albany-Framingham studies. *Am J Cardiol.* 1976; 37: 1073–1078.

[27] Kannel WB, Schatzkin A. Sudden death: lessons from subsets in population studies. *J Am Coll Cardiol.* 1985; 5 (6 suppl):141B–149B.

[28] Lown B. Sudden cardiac death: the major challenge confronting contemporary cardiology. *Am J Cardiol.* 1979; 43: 313–328.

[29] Myerburg RJ, Castellanos A. Cardiac arrest and sudden cardiac death. In: Braunwald E, ed. Heart Disease: A Textbook of Cardiovascular Medicine. Philadelphia, Pa: WB Saunders. 1992;756–789.

[30] Zipes DP, Wellens HJ. Sudden cardiac death. *Circulation.* 1998;98:2334–2351.

[31] Moss AJ. Prediction and prevention of sudden cardiac death. *Ann Rev Med.* 1980;31:1–14.

[32] Gillum RF, Folsom A, Luepker RV, et al. Sudden death and acute myocardial infarction in a metropolitan area, 1970-1980: the Minnesota Heart Survey. *N Engl J Med.* 1983;309:1353-1358.

[33] Roberts WC. Sudden cardiac death: a diversity of causes with focus on atherosclerotic coronary artery disease. *Am J Cardiol.* 1990;65:13B–19B.

[34] Bayes de Luna A, Coumel P, Leclercq JF. Ambulatory sudden cardiac death: mechanisms of production of fatal arrhythmia on the basis of data from 157 cases. *Am Heart J.* 1989;117:151-159.

[35] Internet Medical Education, Inc. The Ventricular Tachycardias. http://www.med-edu.com/patient/arrhythmia/arrhythmia-tachy-ventr.html

[36] Heart Center Online: For cardiologists and their patients. http://www.heartcenteronline.com/myheartdr/common/artprn_rev.cfm?filename=&ARTID=420

[37] Fenton F, Karma A, Hastings H, Evans S. Transition from ventricular tachycardia to ventricular fibrillation as function of tissue characteristics in a computer model. University of Hofstra, NY. http://stardec.hpcc.neu.edu/~fenton/pdf/shpaper.pdf

[38] Gomersall, C. Ventricular Arrhythmia. The Chinese University of Hong Kong. July 1999. http://www.aic.cuhk.edu.hk/web8/ventricular_arrhythmia.htm#classification

[39] Cardionetics Limited. United Kingdom. Cardiac Arrhythmia. http://www.cardionetics.com/docs/healthcr/ecg/arrhythm.htm

[40] Stevenson WG, Friedman PL, Kocovic D, et al. Radiofrequency catheter ablation of ventricular tachycardia after myocardial infarction. *Circulation.* 1998:98:308-314.

[41] Ernoehazy W. Consulting Staff, Department of Emergency Medicine, St. Lukes Hospital of Jacksonville. http://www.emedicine.com/emerg/topic634.htm#section~introduction

[42] Klabunde R. Cardiovascular Physiology Concepts. http://www.cvphysiology.com/Arrhythmias/A006.htm

[43] Medical Dictionary Search Engine. http://www.books.md/index.html

[44] Smith J, Kaplan DT, Cohen RJ. Chapter 25: The Physics of Reentry and Fibrillation. Theoretical Bases. 1990.

[45] Ganong W. Review of Medical Physiology, 16th edition. Appleton and Lange. 1993.

[46] Soejima K, Stevenson, WG. Ventricular tachycardia associated with myocardial infarct scar: a spectrum of therapies for a single patient. *Circulation.* 2002;106:176-179.

[47] The ESVM investigators. Determinants of predicted efficacy of antiarrhythmic drugs in the electrophysiologic study versus electrocardiographic monitoring trial. *Circulation.* 1993;87:323-329.

[48] Preliminary report: effect of encainide and flecainide on mortality in a randomized trial of arrhythmia suppression after myocardial infarction. The Cardiac Arrhythmia Suppression Trial (CAST) investigators. *N Engl J Med.* 1989;321:406.

[49] The Antiarrhythmics versus Implantable Defibrillators (AVID) Investigators. A comparison of antiarrhythmic-drug therapy with implantable defibrillators in patients resuscitated from near fatal ventricular arrhythmias. *N Engl J Med.* 1997;337:1576-1583.

[50] Connoly SJ, Gent M, Roberts RS, et al. Canadian implantable defibrillator study (CIDS); a randomized trial of the implantable cardioverter defibrillator against amiodarone. *Circulation.* 2000;101:1297-1302.

[51] Kuck KH, Cappato R, Siebels J, et al. Randomized comparison of antiarrhythmic drug therapy with implantable defibrillators in patients resuscitated from cardiac arrest. The cardiac arrest study Hamburg (CASH). *Circulation.* 2000;102:748-754.

[52] St. Jude Medical. Implantable Cardioverter Defibrillator System.

http://www.sjm.com/resources/learnmoreabout.aspx?section=ImplantableCardioverterDefibrillatorSystem#ICD

[53] Dvorak E. Implantable Cardioverter-Defibrillator. http://216.239.39.104/search?q=cache:01frH515DxkJ:www.pharmacy.wisc.edu/courses/718-430/2000presentation/Dvorak.pdf+ICD+overdrive+pacing&hl=en&ie=UTF-8

[54] Strickberger SA, Man KC, Daoud EG, et al. A prospective evaluation of catheter ablation of ventricular tachycardia as adjunct therapy in patients with coronary artery disease. *Circulation.* 1997;96:1525-1531.

[55] Miller J, Zipes D. Catheter ablation of arrhythmias. *Circulation.* 2002;106:e203.

[56] Morady F, Harvey M, Kalbfleisch SJ, et al. Radiofrequency catheter ablation of VT in patients with coronary artery disease. *Circulation.* 1993;87:363-372.

[57] Stevenson WG, Khan H, Sager P, et al. Identification of reentry circuit sites during catheter mapping and radiofrequency ablation of ventricular tachycardia late after myocardial infarction. *Circulation.* 1993;88:1647-1670.

[58] Callans DJ, Zado E, Sarter BH, Schwartzman D, Gottlieb CD, Marchlinski FE. Efficacy of radiofrequency ablation for VT in healed myocardial infarction. *Am J Cardiol.* 1998;83:429-432.

[59] Calkins H, Sousa J, El-Atassi R, et al. Diagnosis and cure of the Wolff-Parkinson-White syndrome or paroxysmal supraventricular tachycardias during a single electrophysiologic test. *N Engl J Med.* 1991;324:1612-1618.

[60] Morady F, Radio-frequency ablation as treatment for cardiac arrhythmias. *N Engl J Med.* 1999;340:534-544.

[61] Stevenson WG, Ellison K, LeFroy D, Friedman P. Ablation of cardiac arrhythmias. *Am J Cardiol.* 1997;80(8A):56G-66G.

[62] Calkins H. VII. Catheter Ablation for Cardiac Arrhythmias. In: Dale D, Federman D, eds. Web MD Scientific American. 1999.

[63]Kay JN. Catheter ablation of AV nodal reentrant tachycardia. NASPE Heart Rhythm Society. University of Alabama at Birmingham. http://www.naspe.org/professional_education/learning_categories/articles/kay/

[64] Stevenson WG. Chapter 96: Catheter Mapping of Ventricular Tachycardia. In: Zipes DP, Jalife J, eds. Cardiac Electrophysiology: from Cell to Bedside, 2nd edition. 1995.

[65] Dixit S, Marchlinski FE. Clinical characteristics and catheter ablation of left ventricular outflow tract tachycardia. *Curr Cadriol Rep.* 2001;3(4):305-313.

[66] Fogoros, R. Heart Disease/Cardiology. http://heartdisease.about.com/library/weekly/aa020101b.htm

[67] Stevenson WG, Sager P, Natterson PD, et al. I. Relation of pace-mapping QRS morphology and conduction delay to ventricular tachycardia reentry circuits in human infarct scars. *J Am Coll Cardiol.* 1995;26:481-488.

[68] De Bakker JMT, van Capelle FJL, Janse MJ, et al. Macroreentry in the infracted human heart: mechanism of ventricular tachycardias with a focal activation pattern. J Am Coll Cardiol. 1991;18:1005-1014.

[69] Downar E, Kimber S, Harris L, et al. Endocardial mapping of ventricular tachycardia in the intact human heart. *J Am Coll Cardiol.* 1992;20:869-878.

[70] Kaltenbrunner W, Cardinal R, Dubuc M, et al. Epicardial and endocardial mapping of ventricular tachycardia in patients with myocardial infarction. Is the origin of the tachycardia always subendocardially localized? *Circulation.* 1991;84:1058-1071.

[71] Pogwizd SM, Hoyt RH, Saffitz JE, et al. Reentrant and focal mechanisms underlying ventricular tachycardia in the human heart. *Circulation.* 1992;86:1872-1887.

[72] Three distinct patterns of ventricular activation in infracted human hearts: an intraoperative cardiac mapping study during sinus rhythm. *Circulation.* 1995;91:1480-1494.

[73] Klein LS, Shih HT, Hackett FK, et al. Radiofrequency catheter ablation of ventricular tachycardia in patients without structural heart disease. *Circulation.* 1992;85:1666-1674.

[74] Gardner PI, Ursell P, Fenoglio JJ, Wit AL. Electrophysiologic and anatomic basis for fractionated electrograms recorded from healed myocardial infarcts. *Circulation.* 1985;72:596-611.

[75] Miller JM, Vassallo JA, Hargrove WC, Josephson ME. Intermittent failure of local conduction during VT. *Circulation.* 1985;72:1286-1292.

[76] Stevenson WG, Friedman PL. Chapter 113: Catheter Ablation of Ventricular Tachycardia. In: Zipes DP, Jalife J, eds. Cardiac Electrophysiology: from Cell to Bedside, 3rd edition. 2000.

[77] Stevenson WG, Friedman PL, Sager PT, et al. Exploring post-infarct reentrant ventricular tachycardia with entrainment mapping. *J Am Coll Cardiol.* 1997;29:1180-1189.

[78] Stevenson WG. Catheter ablation of ventricular tachycardias: a conventional mapping approach. 4th Prague Workshop on Catheter Ablation. March 21-23, 2001. IKEM, Prague, Czech Republic. http://www.ekgreading.com/prague_ablation.htm

[79] Okumura K, Henthora RW, Epstein AE, et al. Further observation on transient entrainment: Importance of pacing site and properties of the components of the reentry circuit. *Circulation.* 1985;72:1293-1307.

[80] Downar E, Kimber S, Harris L, et al. Endocardial mapping of ventricular tachycardia in the intact human heart. *J Am Coll Cardiol.* 1992;20:869-878.

[81] Khan HH, Stevenson WG: Activation times in and adjacent to reentry circuits during entrainment: implications for mapping ventricular tachycardia. *Am Heart J.* 1994;127:833-842.

[82] Dixit S, Callans D. Mapping for ventricular tachycardia. *Cardiac Electrophsiol Rev.* 2002;6:436-441.

[83] Ellison KE, Stevenson WG, Couper GS, Friedman PL. Ablation of ventricular tachycardia due to post-infarct ventricular septal defect: identification and transaction of a broad reentry loop. *J Cardiovasc Electrophysiol.* 1997;8:1163-1166.

[84] Hadjis TA, Stevenson WG, Harada T, et al. Preferential locations for critical reentry circuit sites causing ventricular tachycardia after inferior wall myocardial infarction. *J Cardiovasc Electrophysiol.* 1997;8:363-370.

[85] El-Shalakany A, Hadjis T, Papageorgiou P, Monohan K, Epstein L, Josephson ME. Entrainment/mapping criteria for prediction of site of ventricular tachycardia by single radiofrequency lesion in patients with coronary artery disease. *Circulation.* 1999;99:2283-2289.

[86] Bogun F, Bahu M, Knight BP, Weiss R, Paladmo W, et al. Comparison of effective and ineffective target sites that demonstrate concealed entrainment in patients with coronary artery disease undergoing radiofrequency ablation of ventricular tachycardia. *Circulation.* 1997;95:183-190.

[87] Ben-Haim SA, Osadchy D, Schuster I, et al. Nonfluoroscopic, in vivo navigation and mapping technology. *Nat Med.* 1996;2:1393-1395.

[88] Ben-Haim SA. Chapter 92: Non-fluoroscopic Electroanatomical Cardiac Mapping. . In: Zipes DP, Jalife J, eds. Cardiac Electrophysiology: from Cell to Bedside, 3rd edition. 2000.

[89] Hayam G, Gepstein L, Ben-Haim SA. Accuracy of the in vivo determination of location using a new non-fluoroscopic cardiac mapping system [abstract]. *Pacing Clin Electrophysiol.* 1996;19:712.

[90] Shpun S, Gepstein L, Hayam G, Ben-Haim SA. Guidance of radio-frequency endocardial ablation with real-time three dimensional magnetic navigation system. *Circulation.* 1997;96:2016-2021.

[91] Bernd-Dieter G, Catheter ablation of idiopathic ventricular tachycardia: pathophysiological insights and electroanatomical mapping. *Journal of Interventional Cardiac Electrophysiology.* 2001;5:215-217.

[92] Peters NS, Schilling RJ, Davies DW. Chapter 93: Non-Contact Endocardial Activation Mapping. In: Zipes DP, Jalife J, eds. Cardiac Electrophysiology: from Cell to Bedside, 3rd edition. 2000.

[93] Khoury DS, Rudy Y. A model study of volume conductor effects on endocardial and intracavitary potentials. *Circ Res.* 1992;71:511-525.

[94] Rudy Y, Messinger-Rapport BJ. The inverse problem in electrocardiography: solutions in terms of epicardial potentials. *CRC Crit Rev Biomed Eng.* 1988;16:214-268.

[95] Sra J, Bhatia A, Krum D, Akhtar M. Noncontact mapping for radiofrequency ablation of complex cardiac arrhythmias. *Journal of Interventional Cardiac Electrophysiology.* 2001;5:327-335.

[96] Schilling R, Peters N, Davies W. Simultaneous endocardial mapping in the human left ventricle using a noncontact catheter: comparison of contact and reconstructed electrograms during sinus rhythm. *Circulation.* 1998;98:887-898. http://circ.ahajournals.org/cgi/content/full/98/9/887#F3

[97] Gornick CC, Adler SW, Pederson B, et al. Validation of a new non-contact catheter system for electro-anatomic mapping of the left ventricular endocardium. *Circulation.* 1999; 99:829-835.

[98] Schilling RJ, Peters NS, Davies DW. Feasibility of a non-contact catheter for endocardial mapping of human ventricular tachycardia. *Circulation.* 1999;99:2543-2552.

[99] Duru F. CARTO three-dimensional non-fluoroscopic electroanatomic mapping for catheter ablation of arrhythmias: a useful tool or an expensive toy for the electrophysiologist-invited review. *Anadolu Kardiyol Derg.* 2002;4:330-337. http://www.anakarder.com/eng/yazilar.asp?yaziid=242&sayiid=8

[100] Smith J, Cohen R. Simple finite-element model accounts for wide range of cardiac dysrhythmias. *Proc. Natl. Acad. Sci.* USA Medical Sciences. 1984;81:233-237

[101] Moe GK, Rheinboldt WC, Abildskov JA. A computer model of atrial fibrillation. *Am Heart J.* 1964;67:200-220.

[102] Belk, P. Electrical Modeling of Myocardium and Development of Advanced Pacing Techniques. Ph.D. Thesis in the Department of the Harvard-MIT Division of Health Sciences and Technology, 1998.

[103] Rosenband, LM. The Study of Aberrant Conduction in Myocardial Tissue using a Finite-element Computer Simulation. Bachelor's Thesis. Massachusetts Institute of Technology, 1996.

[104] Garfinkle A, Weiss J, Qu Z, et al. Modeling Cardiac Fibrillation, UCLA Medical School, http://nbcr.sdsc.edu/mcmregistration/pdf/Alan_Garfinkel.pdf

[105] Beeler GW, Reuter H. Reconstruction of the action potential of ventricular myocardial fibers. *J. Physiol*, 1977; 268:177-210.

[106] Chernyak YB, Esperer HD, Cohen RJ. Iterative restitution effects from heart rate variability.

[107] Elharrar V, Surawicz B. Cycle length effect on restitution of action potential duration in dog cardiac fibers. *Am J Physiol*. 1983; 13:H782-H792.

[108] Stevenson WG, Friedman PL. Chapter 113: Catheter Ablation of Ventricular Tachycardia. In: Zipes DP, Jalife J, eds. Cardiac Electrophysiology: from Cell to Bedside, 3rd edition. 2000.

[109] Ideker RE, Smith RM, Blanchard SM, et al. The assumptions of isochronal cardiac mapping. *Pace*. 1989;12:436-478.

[110] Armoundas A. A Novel Technique for Guiding Ablative Therapy of Cardiac Arrhythmias. Ph.D. Thesis. Massachusetts Institute of Technology Department of Nuclear Engineering, 1999.

[111] Barley, M. A Device User Interface for the Guided Ablative Therapy of Cardiac Arrhythmias. Masters Thesis. Massachusetts Institute of Technology Department of Electrical Engineering and Computer Science, 2003.

[112] Mark R. Quantitative Physiology: Organ Transport Systems. Notes from Principals of Cardiac Electrophysiology Course. 2000.

[113] Geselowitz D, Ishiwatari H. A theoretical study of the effect of the intracavitary blood mass on the dipolarity of an equivalent heart generator. North Holland Publishing Co, Amsterdam, Holland, 1965.